

**MULTI-BASELINE SEARCHES FOR STOCHASTIC SOURCES AND
BLACK HOLE RINGDOWN SIGNALS IN LIGO-VIRGO DATA**

By
DIPONGKAR TALUKDER

A thesis submitted in partial fulfillment of
the requirements for the degree of
DOCTOR OF PHILOSOPHY

WASHINGTON STATE UNIVERSITY
Department of Physics and Astronomy

AUGUST 2012

To the Faculty of Washington State University:

The members of the Committee appointed to examine the dissertation of DIPONGKAR TALUKDER find it satisfactory and recommend that it be accepted.

Sukanta Bose, Ph.D., Chair

Matthew Duez, Ph.D.

Gregory Mendell, Ph.D.

Guy Worthey, Ph.D.

ACKNOWLEDGEMENT

Firstly, I would like to express my gratitude and warm-hearted thanks to Sukanta Bose for giving me the opportunity to contribute to gravitational-wave science. I am indebted to him for his constant support and guidance throughout my Ph.D. He certainly has been, without any doubt, a wonderful critic of my work.

I enjoyed and benefited from the interactions I had over the years with the members of the LIGO Scientific Collaboration and the Virgo Collaboration. I would like to sincerely thank my research collaborators. First, I have had the great pleasure to work with Paul Baker, Sarah Caudill and Sanjit Mitra. My special thanks to Warren Anderson, Stefan Ballmer, Matthew Benacquista, Nelson Christensen, Neil Cornish, Sanjeev Dhurandhar, Gabriela González, Kari Hodge, Shivaraj Kandasamy, Albert Lazzarini, Vuk Mandic, Sean Morriss, Tania Regimbau, Emma Robinson, Joseph Romano, Eric Thrane, Alan Weinstein and many more for helpful discussions.

I am deeply obliged to Bruce Allen for his support and hospitality during my stay at Albert Einstein Institute, Hannover, Germany. Special thanks to my friends and colleagues Benjamin Knispel, Chris Messenger, Ajith Parameswaran, Holger Pletsch and Reinhard Prix for their help, friendship and entertainment.

I have benefited from enlightening discussions with Gregory Mendell and Fred Raab in our weekly group meetings. I also want to express sincere thanks to my teachers in Washington State University for their inspiration. I take this opportunity to thank my friends in Washington State University. These people

have made my time at WSU productive. I especially enjoyed the company of JiaJia Chang, Thilina Dayanga, Brett Deaton, Shaon Ghosh, Fatemeh H. Nouri, and Szymon Steplewski. I thank Carl Brannen for reading the thesis carefully and providing helpful comments.

Additionally, I would like to thank Matthew Duez, Gregory Mendell and Guy Worthey for all of their time and being willing to serve on my thesis committee. I would like to acknowledge the National Science Foundation for funding my research in gravitational-wave data-analysis in support of LIGO. This work has been supported by the National Science Foundation Grant Nos. PHY-0758172 and PHY-0855679. I would also like to thank College of Sciences (COS) at Washington State University for awarding me a COS Research Assistantship for Spring 2012.

Finally, I cannot end without thanking my family for their sacrifice and encouragement. I owe my deepest thanks to Shampa Biswas for her unending love and enormous patience. In February 2009, I lost my father, thanks to Steven Tomsovic for letting me visit home in the middle of the semester, and Gordon Johnson, Ranga Dias and Ashish Mishra for taking care of teaching my labs.

MULTI-BASELINE SEARCHES FOR STOCHASTIC SOURCES AND BLACK
HOLE RINGDOWN SIGNALS IN LIGO-VIRGO DATA

Abstract

by Dipongkar Talukder, Ph.D.
Washington State University
August 2012

Chair: Sukanta Bose

We present a framework for the detection of stochastic gravitational-wave (GW) backgrounds, from cosmological and astrophysical sources, using radiometry with a network of gravitational-wave interferometers. The search statistic itself is derived from the cross-correlations of the data across all possible baselines in a detector network, and reveals how much more sensitive a network is than any of its component baselines. We model the neutron star distribution in the Virgo cluster and apply the above framework to search for their stochastic GW signature in LIGO-VIRGO data.

We also present a template-based multi-detector coherent search for perturbed black hole ringdown signals. Like the past “coincidence” ringdown searches in LIGO data, our method incorporates knowledge of the ringdown waveform in constructing the search templates. Additionally, it checks for consistency of signal amplitudes and phases in the different detectors with their different orientations and signal arrival times. We demonstrate the advantages of implementing a coherent search in the ringdown search pipeline.

DEDICATION

There are many people in the world in poverty due to circumstances they cannot control. Even though many people fear the future, many have overcome poverty, neglect, and difficult situations to become successful. To them I dedicate my thesis.

PREFACE

The thesis focuses on the efforts to detect gravitational waves from neutron stars and black holes. The work presented here is based on three peer-reviewed journal publications [12, 13, 14], and my direct involvement in two LIGO-VIRGO searches. My participation in all of these projects has been extensive. In the context of signal processing, I studied coherent contribution of gravitational-wave detectors to extracted signal power for different types of sources. In places where I have presented results derived from LIGO data I have done so with permission from the LIGO Scientific Collaboration (LSC). A part of the methods and results presented here is under review and is potentially subject to change. The opinions expressed here are my own and not necessarily those of the LSC.

Contents

1	Introduction: Gravitational waves and their sources and detection	1
1.1	Gravitational waves (GWs) in general relativity	3
1.2	Sources of gravitational waves	6
1.3	Principle of a GW detector	8
2	Detecting an anisotropic stochastic background with multi-baseline GW radiometry	15
2.1	The stochastic GW backgrounds (SGWBs)	16
2.1.1	The detector strain due to a SGWB	19
2.1.2	Statistical properties of the signal and detector noise	22
2.2	Principle of a GW radiometer	23
2.3	Optimal search statistic	27
2.3.1	Cross correlation statistic	27
2.3.2	Detection statistic	28
2.3.3	Performance of optimal detection statistic	35
2.4	Performance of multi-baseline radiometers	41
2.4.1	Sensitivity	42

2.4.2	Sky coverage	45
2.4.3	Parameter accuracy	49
2.4.4	Map making	53
2.4.4.1	Dirty maps and clean maps	55
2.4.4.2	Maximized-likelihood-ratio statistic	57
2.5	Discussion	60
3	Searching for a SGWB from the population of neutron stars in the Virgo cluster	69
3.1	Motivation for the directed search	70
3.2	Modeling the neutron stars in the Virgo cluster	75
3.2.1	The gravitar model	76
3.2.2	A population synthesis model of millisecond pulsars	80
3.2.3	A simple power-law	82
3.3	The directed SGWB search and Olbers' paradox	82
3.4	Setting up the analysis	84
3.4.1	Methodology	84
3.4.2	Angular extension of the Virgo cluster	86
3.4.3	The analysis pipeline	86
3.4.4	Simulations	88
3.5	Discussion	90
4	Searching for perturbed black hole ringdown signals	91
4.1	Motivation for the search	92
4.2	Quasi-normal modes of black holes	94

4.2.1	Schwarzschild and Kerr black holes	95
4.2.2	Black hole perturbation	95
4.2.3	The ringdown waveform	97
4.3	Ringdown searches with matched filtering	100
4.3.1	Matched filter	100
4.3.2	Template banks	101
4.4	A coincident multi-detector search	102
4.4.1	The coincidence search pipeline	104
4.4.1.1	Data set	104
4.4.1.2	Template placement	106
4.4.1.3	Trigger generation	109
4.4.1.4	Coincidence analysis	113
4.4.2	Tuning the search	115
4.5	The coherent multi-detector search	125
4.5.1	Elliptically-polarized ringdown template	125
4.5.1.1	Fourier transformation of a generic decaying sinusoid	129
4.5.1.2	Fourier transformation of an elliptically-polarized ringdown template	131
4.5.1.3	The template normalization	132
4.5.1.4	Numerical analysis	133
4.5.1.5	SNR statistic	136
4.5.2	Coherent statistics	137
4.5.3	Performance study	140

4.6	Discussion	141
5	Aspects of a blind hierarchical coherent search for coalescing compact binaries	145
5.1	Introduction	147
5.2	Multi-detector statistics	149
5.2.1	Signal and noise	150
5.2.2	The network detection statistic	152
5.2.3	Alternative statistics	159
5.3	Coherent hierarchical inspiral analysis pipeline	162
5.4	Results	165
5.5	Discussion	168
A	Technical details	173
A.1	Antenna response	173
A.2	Parameter accuracy	176
B	Advanced detectors studies	178
B.1	Performance of multi-baseline radiometers	178
C	A directed SGWB search and Olbers' paradox	183
C.1	Virgo cluster versus the isotropic background	183
D	Notes on SNR threshold	186
D.1	SNR thresholds for the S4 ringdown search	186
E	List of abbreviations	188

List of Figures

1.1	Effect of the two polarizations of GWs on test particles	6
1.2	Schematic of an earth-based interferometric detector	10
1.3	Different noise sources that contribute to the sensitivity of the first generation LIGO detectors	11
1.4	Strain amplitude spectral densities of LIGO detectors during their S5 science runs	13
1.5	The noise in LIGO, Narrow-band (NB) LIGO-II, and Wide-band (WB) LIGO-II, and the estimated signal strengths plotted as a function of gravitational wave frequency	14
2.1	Gravitational wave spectrum as a function of frequency for SGWB sources from inflationary models	17
2.2	The 95% Bayesian upper limit of the point estimate of a constant SGWB spectrum	18
2.3	Gravitational wave spectrum as a function of observed frequency for potential AGWB sources	20
2.4	Geometry of an elementary GW radiometer	24
2.5	Illustration of a GW radiometer beam pattern	30

2.6	Designed noise amplitude spectrum of the initial and advanced LIGO and VIRGO, and the Einstein Telescope	36
2.7	The injected, dirty, and clean sky maps of a weak polar-cap GWB source	38
2.8	Histograms of the dirty maps for the noise-only data set and weak polar-cap signal	39
2.9	The distribution of the MLR statistic obtained for dirty maps generated from noise-only and weak polar-cap injection	40
2.10	The sensitivities and their area-weighted counterparts of three different baselines and their network are plotted as functions of the declination of a single-pixel SGWB source	44
2.11	The sensitivities of three single baselines and their multibaseline network plotted as functions of the central frequency of the source band	45
2.12	The standard deviation of dirty maps measured by the three LIGO-Virgo baselines and the full network for a constant source power spectrum	47
2.13	The beam functions for the three LIGO-Virgo baselines for a constant source spectrum	49
2.14	Singular values of the Fisher matrices for individual baselines and the whole network	50
2.15	The 1σ error and area-weighted 1σ error in the solid angle for locating a source in the sky with three single baselines and their network	54

2.16	Toy model of an extended source and the dirty maps made from simulated data	56
2.17	Clean maps obtained by the deconvolution of the dirty maps of Fig. 2.16	57
2.18	Difference between the clean maps of Fig. 2.17 and the injected map of Fig. 2.16(a)	58
2.19	The toy model of a localized source and the dirty maps made from simulated data	59
2.20	Clean maps obtained by the deconvolution of the dirty maps of Fig. 2.19	60
2.21	Difference between the clean maps of Fig. 2.20 and the injected map of Fig. 2.19(a)	61
2.22	Dirty maps made for simulated noise, without any injected signals	63
2.23	Clean maps obtained by the deconvolution of the dirty maps of Fig. 2.22	64
2.24	The toy model of a very weak extended source and the dirty maps made from simulated data	66
2.25	Clean maps obtained by the deconvolution of the dirty maps of Fig. 2.24	67
3.1	The distribution of observed radio pulsars	72
3.2	The spectral density of gravitational radiation from NSs in the Virgo cluster plotted as a function of GW frequency	73

3.3	The noise amplitude spectral densities of various advanced detectors are compared with the effective source amplitude spectral density	74
3.4	The distribution of observed millisecond pulsars	80
3.5	Several model-dependent spectral profiles of SGWB from NSs in the Virgo cluster	83
3.6	The map of a modeled signal-strength vector of the Virgo cluster .	86
3.7	The spherical harmonic coefficients of the modeled signal-strength vector	87
3.8	A schematic diagram of the stochastic search pipeline	88
3.9	The MLR statistic of a simulated SGWB in the Virgo cluster is plotted for different harmonic cutoff	89
4.1	Ringdown waveform for a black hole of mass $100 M_{\odot}$ and spin 0.7	98
4.2	Central frequency of the ringdown waveform as a function of mass for three spin values and quality factor as a function of spin are plotted	99
4.3	A schematic diagram of the coincidence and coherent stages of the ringdown search pipeline.	105
4.4	The ringdown horizon distance as a function of mass for a spinning black hole	107
4.5	The template bank for the LIGO-VIRGO S5/S6 ringdown search .	108
4.6	Contours of constant mismatch around templates of a constant frequency and for a portion of the template bank	109

4.7	Ringdown waveforms in the extremes of the parameter space, characterized by central frequency and quality factor	110
4.8	Decisive distance of missed and found injections is plotted against chirp mass and frequency	119
4.9	Scatter plots of simulated and estimated effective distance of found PHENOM injections	120
4.10	Scatter plots of simulated mass 2 versus mass 1 of made and found PHENOM injections and histogram of number of made and found PHENOM injections per mass-ratio bin	121
4.11	Scatter plots of simulated and estimated effective distance of found RINGDOWN injections	122
4.12	Scatter plots of simulated and estimated frequency of found RINGDOWN injections, also scatter plots of simulated and estimated mass	123
4.13	Scatter plots of simulated quality factor and frequency, and spin and mass of made and found RINGDOWN injections	124
4.14	Contour plots of H2 SNR versus H1 SNR, L1 SNR versus H1 SNR, and L1 SNR versus H2 SNR for triple coincident time-slide events	126
4.15	Contour plots of H2 SNR versus H1 SNR, L1 SNR versus H1 SNR, and L1 SNR versus H2 SNR for triple coincident injection events .	127
4.16	The H1-H2, H1-L1, and H2-L1 SNR distributions for time-slides and injections	128
4.17	Scatter plots of the old and new triple-coincidence ranking statistics	129

4.18	The efficiency of finding injections and the ROC curve are compared between the old and new triple-coincidence ranking statistics	130
4.19	The integrands of the sine and cosine template variances are plotted as functions of frequency	135
4.20	Contours of the fractional difference of sine and cosine phases of an elliptically-polarized ringdown template	136
4.21	The scatter plots for the null-stream and coherent SNR, and the bitten-L and effective-coherent SNR	142
4.22	Efficiency of finding signals using the coincidence search is compared with that of using the coherent search	143
4.23	The ROC curve of the coincidence search is compared with the ROC curve of the coherent search	144
5.1	A schematic diagram of the coherent stage in the compact binary coalescence search pipeline	166
5.2	Scatter plots of the combined and coherent SNRs of the triggers from simulated data	171
5.3	The receiver operating characteristic curves of three CBC searches are compared	172
A.1	Definition of source location and orientation angles relative to the inertial frame of a GW detector	174
A.2	The antenna response of interferometric GW detectors to GWs with plus and cross polarizations	175

B.1	The sensitivities and area-weighted sensitivities of different LIGO-VIRGO-INDIGO-KAGRA networks in their second and third generation configurations are plotted as functions of the declination of a single-pixel SGWB source	179
B.2	The beam functions of different second-generation LIGO-VIRGO-INDIGO-KAGRA baselines for a constant source PSD	180
B.3	Singular values of the Fisher matrices for different second-generation LIGO-VIRGO-INDIGO-KAGRA networks	181
B.4	The 1σ error and area-weighted 1σ error in the solid angle of locating a source in the sky with different LIGO-VIRGO-INDIGO-KAGRA networks in their second and third generation configurations	182

List of Tables

1.1	International network of gravitational-wave interferometers	13
2.1	MLR statistic of dirty maps versus clean maps for the simulated maps in Fig.s 2.16 and 2.17	62
2.2	MLR statistic of dirty maps versus clean maps for the simulated maps in Fig.s 2.19 and 2.20	62
2.3	MLR statistic of dirty maps versus clean maps for simulated noise in Fig.s 2.22 and 2.23	65
2.4	MLR statistic of dirty maps versus clean maps for the simulated maps in Fig.s 2.24 and 2.25	65
4.1	Extreme values for frequency and quality factor of the ringdown template bank	111

Chapter 1

Introduction: Gravitational waves and their sources and detection

In 1916, Albert Einstein published his famous paper entitled “Die Grundlage der allgemeinen Relativitätstheorie (The Foundation of the General Theory of Relativity)” [1]. General Relativity (GR) describes how matter and energy affects the curvature of space-time. The existence of gravitational waves is predicted in GR. A gravitational wave is a fluctuation in the curvature of space-time that propagates with the speed of light. It transports energy and momentum away from the source. When two massive objects, like neutron stars, orbit each other, space-time is stirred by their motion, and gravitational radiation ripples outward into the universe. The key possible sources of gravitational waves are colliding compact binaries, rotating non-axisymmetric neutron stars, stellar core collapse, and stochastic background.

In General Relativity, the lowest mass multipole that produces gravitational

waves is the quadrupole. The conservation of energy and momentum forbids gravitational wave emission associated with the monopole and dipole moments. Gravitational waves (GWs) decrease in amplitude as the inverse of the distance from the source. Owing to their extraordinarily weak interaction with matter, GWs travel cosmological distances with negligible absorption or distortion. This has made direct detection of gravitational waves extremely challenging. Nevertheless, the weakness of interaction enables us to obtain precise information on their sources.

Indirect evidence for the existence of gravitational waves was found by Hulse and Taylor [2]. They discovered a binary system, PSR 1913+16, that is composed of a pulsar and a companion neutron star (NS). From the long term precise observations of the pulsar frequency, the decay rate of the orbital period was found to be consistent with the predicted energy loss due to the emission of gravitational waves. For this discovery, they were awarded the Nobel Prize in physics in 1993. However, no one has yet succeeded in directly detecting gravitational waves. Several kilometer-scale gravitational-wave detectors such as LIGO and VIRGO have been constructed and a few more are in the process of being built world-wide. Detection of gravitational waves is not only important to test GR but also because it promises to open a new window for GW astronomy. It will tell us about the dynamics of large-scale events in the universe like the death of stars, and the birth of black holes (BHs).

1.1 Gravitational waves in general relativity

In this work, we adopt the following notation: The space-time coordinates are denoted by $x^\mu := (x^0, x^i) = (x^0, x^1, x^2, x^3) = (ct, x, y, z)$. While the *Greek letters* (e.g. μ, ν) are space-time indices (0, 1, 2, 3), the *Latin indices* (e.g. i, j) denote the three spatial coordinate labels, 1, 2, 3. Partial derivatives with respect to the coordinates are abbreviated using the symbols $\partial_\mu \equiv \partial/\partial x^\mu$ and $\partial^\mu \equiv \partial/\partial x_\mu$. We also define a comma-notation to indicate derivatives, i.e., $\partial_\beta f \equiv f_{,\beta}$ and $\partial^\beta f \equiv f^{,\beta}$. Repeated indices are summed over unless otherwise indicated.

The General Theory of Relativity asserts that the curvature of space-time is gravity. Curved space-time is best described in Riemannian manifolds [3] by a metric $g_{\mu\nu}$, which is a function of the space-time coordinates x^μ . The infinitesimal proper distance $d\tau$ between two space-time events separated by coordinate distance dx^μ is given by

$$d\tau^2 = g_{\mu\nu} dx^\mu dx^\nu, \quad (1.1)$$

where the Einstein summation convention is understood on the right hand side. In the limit of flat space-time, the metric $g_{\mu\nu}$ becomes the Minkowski metric $\eta_{\mu\nu} = \text{diag}(-1, 1, 1, 1)$.

The curvature and dynamics of space-time governed by the distribution and kinematics of energy are expressed geometrically by the Einstein Field Equations (EFE):

$$G_{\mu\nu}(g) = \frac{8\pi G}{c^4} T_{\mu\nu}, \quad (1.2)$$

where $G_{\mu\nu}$ is the Einstein tensor, G is Newton's constant and $T_{\mu\nu}$ is known as the stress-energy tensor. Due to its inherent nonlinearity, a complete description

of the solutions of EFE is not yet possible. One class of solutions to the EFE is obtained in the linearized theory close to flat space-time, i.e., where fields are everywhere weak.

In weak gravity, the metric is approximately Minkowskian and can be decomposed into the flat space-time metric plus a small perturbation,

$$g_{\mu\nu} = \eta_{\mu\nu} + h_{\mu\nu} , \quad |h_{\mu\nu}| \ll 1. \quad (1.3)$$

The most general coordinate transformation of the form

$$x^\mu \rightarrow x^\mu + \zeta^\mu(x) , \quad |\zeta^\mu_{,\nu}| \ll 1, \quad (1.4)$$

preserves the form of the metric given by (1.3) if the perturbations are transformed using the formula

$$h_{\mu\nu} \rightarrow h_{\mu\nu} - \zeta_{\mu,\nu} - \zeta_{\nu,\mu} . \quad (1.5)$$

To see the physical effect of a gravitational wave it is useful to choose a gauge. The Lorentz gauge freedom allows us to choose a coordinate system where the trace-reversed metric perturbations,

$$\bar{h}_{\mu\nu} := h_{\mu\nu} - \frac{1}{2}\eta_{\mu\nu}h^\alpha{}_\alpha , \quad (1.6)$$

are divergence free,

$$\bar{h}_{\mu\nu}{}^{,\nu} = 0. \quad (1.7)$$

This reduces the Einstein field equation to a simple wave equation:

$$\square \bar{h}_{\mu\nu} = -\frac{16\pi G}{c^4} T_{\mu\nu} , \quad (1.8)$$

where \square denotes the d'Alembertian operator:

$$\square := \partial_\mu \partial^\mu = -\frac{1}{c^2} \frac{\partial^2}{\partial t^2} + \nabla^2. \quad (1.9)$$

We now focus on a region of space outside the source where all the components of the stress-energy tensor are zero, i.e.,

$$\square \bar{h}_{\mu\nu} = 0. \quad (1.10)$$

This allows us to impose the transverse-traceless (TT) gauge, defined by the conditions:

$$\begin{aligned} h_{\mu\nu}{}^{,\nu} &= 0 \quad (\text{transverse}), \\ h_\mu{}^\mu &= 0 \quad (\text{traceless}), \end{aligned} \quad (1.11)$$

which assures that the trace-reversed perturbation $\bar{h}_{\mu\nu}$ is identical to the physical perturbation $h_{\mu\nu}$.

The effect of a gravitational wave on a test mass in space can be found by looking at a plane wave solution of Eq. (1.10) under TT gauge with wave vector k_σ :

$$h_{\mu\nu}(x) = A_{\mu\nu} e^{ik_\alpha x^\alpha}, \quad (1.12)$$

with $k_\alpha k^\alpha = 0$ and $A_{\mu\nu} k^\nu = A_\mu{}^\mu = 0$. Choosing the wave vector k_i along the z-axis, one can completely parameterize the amplitude $A_{\mu\nu}$ by two independent polarizations, h_+ and h_\times :

$$A_{\mu\nu} := \begin{pmatrix} 0 & 0 & 0 & 0 \\ 0 & h_+ & h_\times & 0 \\ 0 & h_\times & -h_+ & 0 \\ 0 & 0 & 0 & 0 \end{pmatrix}. \quad (1.13)$$

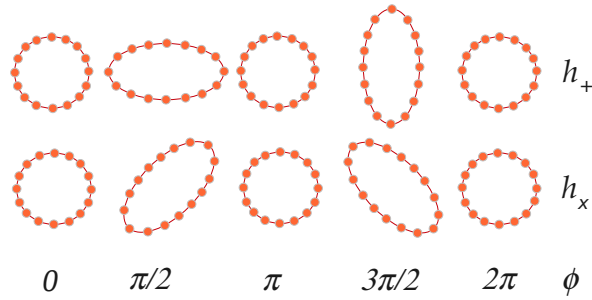


Figure 1.1: The effect of the two polarizations h_+ (*top panel*) and h_\times (*bottom panel*) of a complete cycle of sinusoidal gravitational wave propagating through the page on a ring of test particles.

A gravitational wave with h_+ polarization stretches distance along x -axis and shortens distance along y -axis during the first half cycle and does the opposite during the second half cycle. The h_\times polarization does the same thing, but in a coordinate system rotated by 45 degree. Figure 1.1 shows the effect of a gravitational wave on a ring of particles.

1.2 Sources of gravitational waves

There are different kinds of “known” and “unknown” sources which generate GW with different frequency spectra. Interferometric gravitational wave detectors have achieved unprecedented sensitivity to gravitational waves, expected from sources of different kinds. Depending on lifetimes and other characteristics, the sources can be categorized as follows:

Transient: Transient sources are those which produce a very short duration, a few milliseconds to a few minutes, gravitational wave signal. Brief transients from violent events like a coalescing compact binary, composed of massive neutron stars and/or black holes and asymmetrical core collapse in supernovae are in this category. Core collapse in massive stars has long been regarded as likely to be an important source of gravitational waves.

According to GR a binary system composed of either neutron stars and/or black holes (NS-NS, BH-NS, BH-BH) emits gravitational radiation at twice the orbital frequency, causing the orbit to shrink. As a result, the components of the system spiral in towards one another eventually combining to form a single object, most likely a black hole, which too radiates gravitational waves as it approaches a stable state. The time when the two objects orbit around one another is called “inspiral phase” and the gravitational wave emitted is reasonably well modeled. However, the final few orbits and plunge in towards one another is still “poorly” understood. This phase is called the “merger phase”. Numerical relativity plays an important role in modeling the waveform associated with the merger phase. The final phase is known as “ringdown phase”, and its gravitational radiation waveform is well modeled in black hole perturbation theory. However, a large class of transients including the most violent and catastrophic ones are unmodeled.

Continuous: Periodic sources like pulsars and inspiraling binaries which emit GW continuously over a long duration without significant change in their characteristics are called continuous sources. A rapidly spinning neutron star emits gravitational wave if its shape deviates from axisymmetry or its rotation

is wobbling. Vibrational modes of a neutron star, if driven by accretion or an instability, also would emit continuous GW for a long period of time.

Stochastic: Stochastic backgrounds of gravitational waves are produced by a superposition of a large number of independent, uncorrelated astrophysical and cosmological origin that are not individually resolvable.

Depending on source characterizations, there exists several search methods. The GW signals from compact coalescing binaries have been “precisely” modeled using post-Newtonian approximations, hence matched filtering technique is used for extracting the true GW signal buried in strong detector noise. For the unmodeled transients, most approaches involve looking for excess power in certain frequency bands at certain times. A targeted search, by correlating signals from two detectors with a time dependent phase factor that accounts for the light travel time delay between two detectors, is the best strategy for the detection of GW from known radio pulsars. Since the stochastic signals are unmodeled, the best strategy to detect stochastic sources is by correlating outputs of two detectors with appropriate time delays.

1.3 Principle of a GW detector

In a nutshell a laser interferometric gravitational-wave observatory is a sensitive interferometer that measures the change in relative spatial distance of suspended test masses induced by an impinging gravitational wave. Figure 1.2 is a schematic of an earth-based laser interferometric detector. The basic principle on which a detector works is that of interference of light waves. Each of the two

orthogonal arms of the interferometer contains a pair of mirrored test masses which form a Fabry-Perot optical cavity [4]. Laser light is divided at the beam splitter, and reflected from the cavities in each arm. This reflected light acquires a phase shift which is very sensitive to the separations of the test masses. These phase shifts are then compared when the light recombines at the beam splitter. If there is an impinging gravitational wave it will act to stretch or squeeze the surrounding space-time, effectively causing distances to shrink in one arm while stretching in the other. This then leads to an overall phase difference in the light of the two arms.

Suppose the interferometer in Fig. 1.2 is arranged such that its arms lie along the x and y axes. Suppose further that test masses are separated by a distance L along the arms. When a gravitational wave with polarization h_+ passes through the interferometer, the separation between the two masses in the x arm is given by

$$L_x(t) = \sqrt{L g_{xx}} L \approx \left(1 + \frac{h_+(t)}{2}\right) L, \quad (1.14)$$

whereas, in the y arm,

$$L_y(t) \approx \left(1 - \frac{h_+(t)}{2}\right) L. \quad (1.15)$$

The wave is thus detectable by measuring the length difference between two arms. The fractional difference in length of the two arms is given by

$$\frac{\delta L(t)}{L} := \frac{L_x(t) - L_y(t)}{L} = h_+(t). \quad (1.16)$$

Generally, both polarizations of the wave influence the test masses and hence,

$$\frac{\delta L(t)}{L} = F^+ h_+(t) + F^\times h_\times(t) \equiv h(t), \quad (1.17)$$

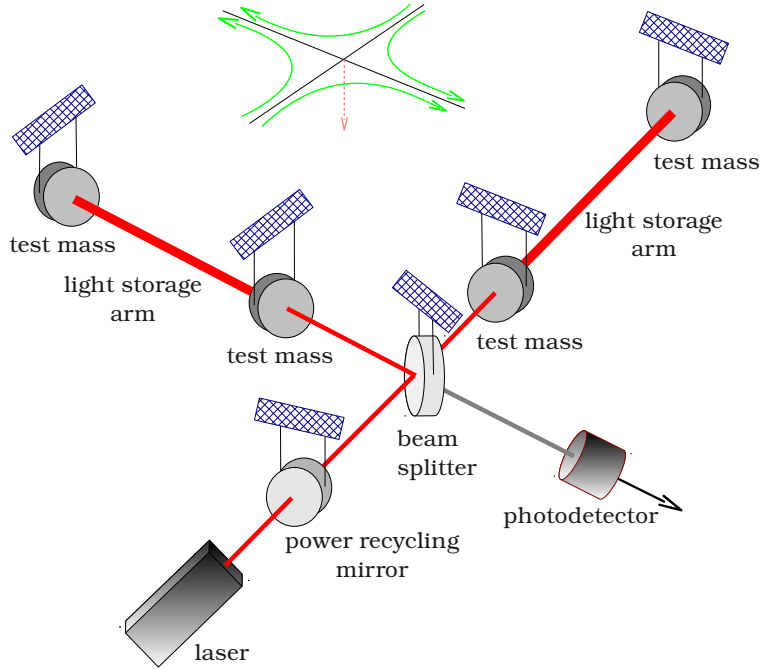


Figure 1.2: Simplified schematic of an earth-based interferometric detector, showing its primary components.

where F^+ and F^\times are antenna response functions, which depend on the source location and the detector orientation, which changes with time, as the Earth spins (see Appendix A.1). Since a gravitational wave induces a strain in the detector, $h(t)$ is often referred to as the “gravitational wave strain”. As an example, the typical strain induced by a GW from a NS-NS binary in the Virgo cluster is $h \sim 10^{-21}$. To be sensitive to such a strain, we need to measure $\delta L = hL \sim 10^{-18}$ m with 4 km long arms.

The principal noise sources affecting interferometer sensitivity are background

motions of the test masses, mainly due to seismic noise, thermal noise, and noise in sensing the test mass motion due to laser noise, quantum fluctuations of the light, and fluctuations in the number of residual gas molecules traversing the optical beams. Among them, the seismic noise and the photon shot noise limit the sensitivity of the interferometers at low and high frequencies, respectively. The thermal noise associated with thermal vibration of mirrors and their suspension limits the sensitivity of the detectors in the intermediate band. Figure 1.3 illustrates how the different noise sources contribute to the sensitivity of the first generation LIGO detectors.

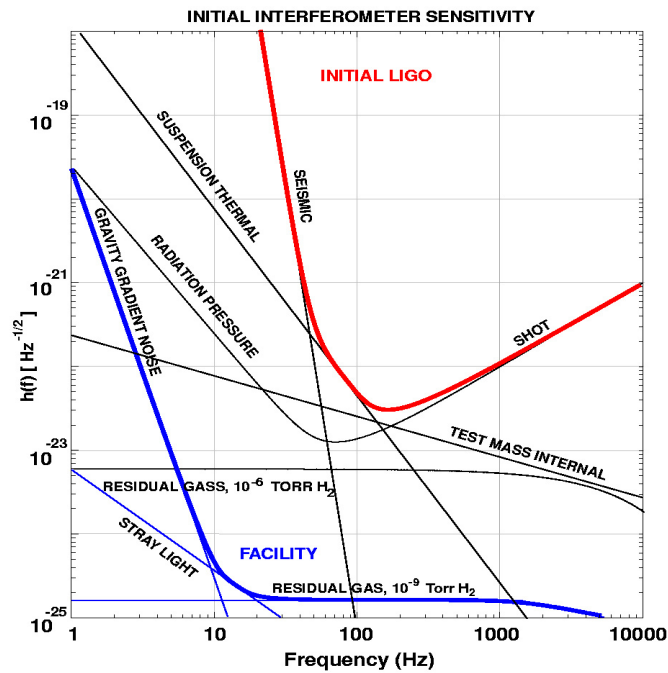


Figure 1.3: An illustration of the sensitivity of the first generation LIGO detectors along with the different noise sources that impact the sensitivity [9].

Table 1.1 specifies the locations of both existing and planned detectors all

over the world. Currently, there are three LIGO detectors: Livingston, Louisiana hosts one detector of arm length 4 km and Hanford, Washington hosts two detectors of arm lengths 2 km and 4 km. The French-Italian 3 km long VIRGO detector is located at Cascina, Italy. In the past few years, these first generation detectors have successfully operated at or near design sensitivity [5, 6]. Figure 1.4 shows the strain amplitude spectral densities of LIGO detectors during their S5 science runs. The LIGO/VIRGO detectors are currently in the process of being upgraded to advanced configurations that are due to come on line in 2015. The new detectors will improve the strain sensitivity of current instruments by a factor of ten, while also lowering the start of the sensitive frequency range from 40 Hz down to 10 Hz, resulting in a thousandfold increase in the observable volume of space. Construction of a Japanese second generation 3 km long cryogenic gravitational-wave detector, KAGRA, has been started [7]. KAGRA was previously known as LCGT for Large-scale Cryogenic Gravitational-wave Telescope. There is a proposal for an Indian detector (INDIGO), the site for which has not been selected yet. The British-German 600 m long GEO is located near Hannover, Germany and is mainly used for testing optics for LIGO/aLIGO detectors [8].

Figure 1.5 shows, along with the noise $\tilde{n}(f)$ curves, the estimated signal strengths $\tilde{h}(f)$ for various sources. The signal strength $\tilde{h}(f)$ is defined in such a way that, wherever a signal point or curve lies above the interferometer's noise curve, the signal, coming from a random direction in the sky and from a source with a random orientation, is detectable with a false alarm probability of less than one percent.

Table 1.1: The geographic location and orientation of an international network of gravitational-wave interferometers. The orientation is the geographic compass angle, measured clockwise from north, of the line bisecting the arms of the detector [10].

Detector	Label	Longitude	Latitude	Orientation
LIGO Livingston, LA	L (L1)	90° 46' 27.3" W	30° 33' 46.4" N	208.0°
LIGO Hanford, WA	H (H1 & H2)	119° 24' 27.6" W	46° 27' 18.5" N	279.0°
VIRGO, Italy	V (V1)	10° 30' 16" E	43° 37' 53" N	333.5°
KAGRA, Japan	K (K1)	137° 18' 36" E	36° 24' 36" N	16.69°
INDIGO, India	I	74° 02' 59" E	19° 05' 47" N	270.0°

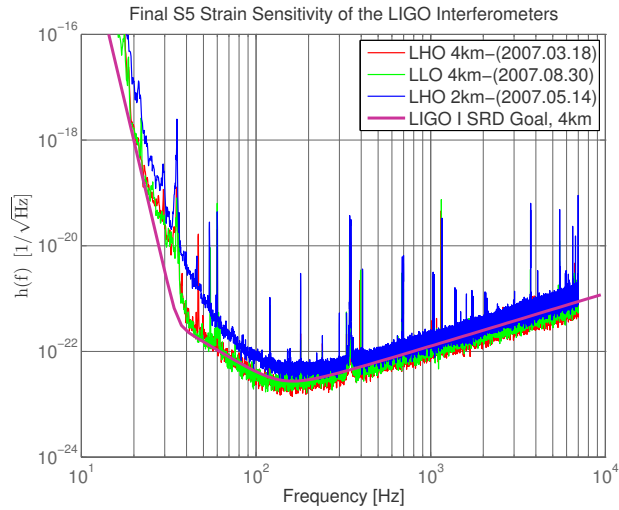


Figure 1.4: Strain amplitude spectral densities of LIGO detectors during their S5 science runs. For comparison, the solid magenta curve shows the design reference noise budget of first generation LIGO interferometers.

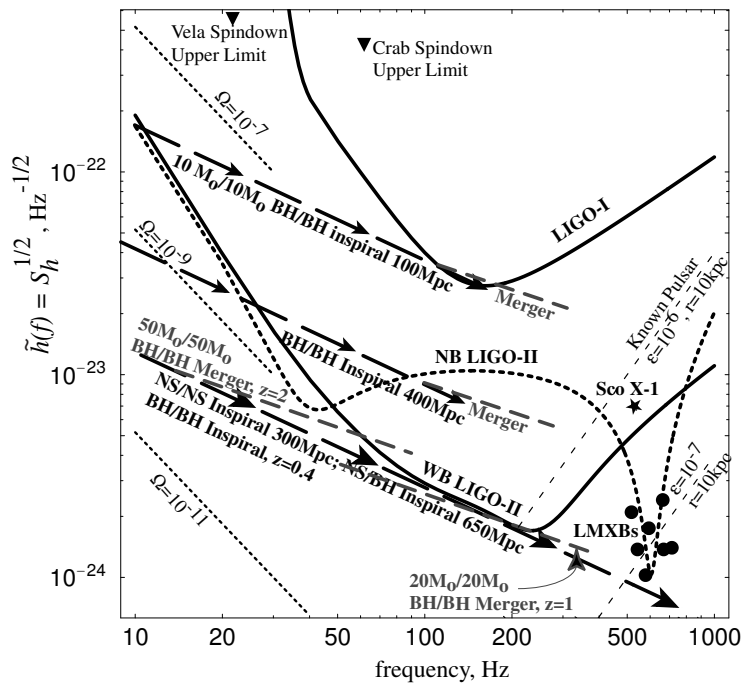


Figure 1.5: The noise $\tilde{n}(f)$ in LIGO, Narrow-band (NB) LIGO-II, and Wide-band (WB) LIGO-II plotted as a function of gravitational wave frequency f , and compared with the estimated signal strengths $\tilde{h}(f)$ from various sources [11].

Chapter 2

Detecting an anisotropic stochastic background with multi-baseline GW radiometry

The Cosmic Microwave Background (CMB) was first detected, serendipitously, in 1964 by Penzias and Wilson [15]. This discovery supports that the universe had a beginning permeated by the cosmic microwave background as predicted by earlier theories [16]. The universe is also expected to have Stochastic Gravitational Wave Backgrounds (SGWBs) of cosmological and astrophysical origin. Incoherent superposition of unmodeled and/or unresolved sources of GWs constitute a SGWB [17]. The GWs from these sources could be too weak to be detected separately. But if the number of sources that contribute to each frequency bin is much larger than one, then searching their GW profiles in LIGO and Virgo data is an interesting prospect.

The LIGO Scientific Collaboration and the Virgo Collaboration are searching for transients, continuous signals and stochastic backgrounds in the data from their detectors. The search for an isotropic stochastic GW background has caught significant attention due to its cosmological significance. This primordial GW background is a direct probe of cosmological inflation [18]. It is well established that the cosmic microwave background is isotropic, which indicates that the early universe was highly isotropic. But the assumption of isotropy for SGWB may not be true. For example, if the dominant source of stochastic gravitational waves in the frequency band of the earth-based detectors is an ensemble of nearby astrophysical sources, such as low-mass x-ray binaries or, even, coalescing compact objects, then the stochastic background will have a distinct *anisotropy*. The astrophysical GW background (AGWB) is of major interest in this chapter.

2.1 The stochastic GW backgrounds

In the early universe, inflation produced a stochastic background of gravitational waves through the parametric amplification of primordial quantum fluctuations [19]. Unfortunately this background itself is too weak to be directly detected with existing ground-based detectors. In the period following inflation there are a number of mechanisms that may have operated to produce additional SGWB from inhomogeneities in the fields that populate the early universe. For example, first-order phase transitions in the early universe can generate a stochastic background of gravitational waves that may be detectable today [20].

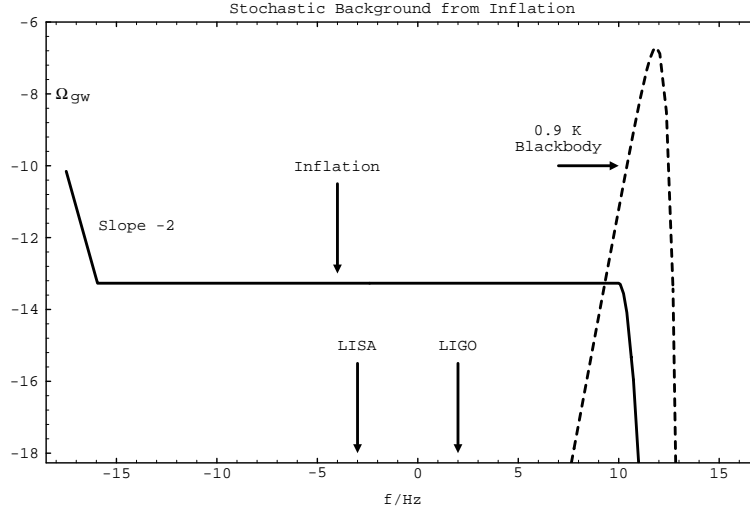


Figure 2.1: The spectrum of stochastic gravitational waves in inflationary models is flat over a wide range of frequencies, and is shown as the solid curve [17]. The horizontal axis is \log_{10} of frequency, in Hz. The vertical axis is $\log_{10} \Omega_{\text{GW}}$ defined in Eq. (2.8).

Fig. 2.1 shows the spectrum of a SGWB predicted by inflationary models that exist today over a wide range of frequencies. The inflationary spectrum rises rapidly at low frequencies and falls off above the frequency scale f_{max} associated with the fastest characteristic time of the phase transition at the end of inflation. Because the spectrum falls off as the inverse of the square of frequency at low frequencies, this is certainly too small to be detectable with either initial or advanced LIGO. Although LIGO has not yet detected a gravitational wave signal, it has ruled out some early-universe models that predict a relatively large stochastic GW background as shown in Fig. 2.2. The data rule out models of

early universe evolution with a relatively large equation-of-state parameter, as well as cosmic (super)string models with relatively small string tension that are favored in some string theory models. This search for the stochastic background improves on the indirect limits from Big Bang nucleosynthesis and cosmic microwave background at 100 Hz [18].

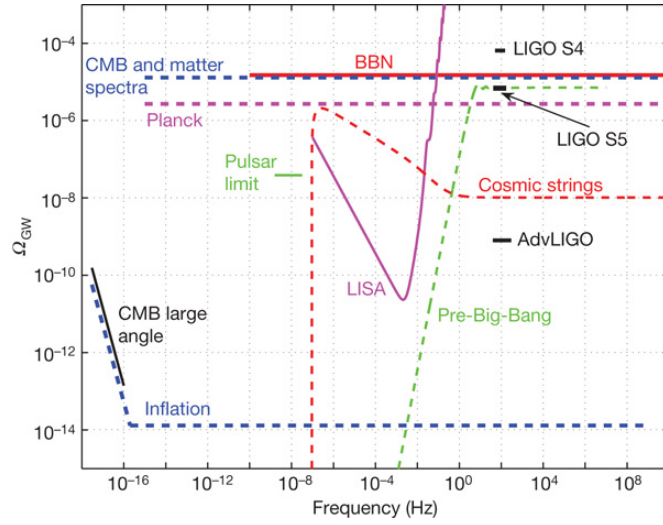


Figure 2.2: The 95% Bayesian upper limit of the point estimate of a constant SGWB spectrum, $\Omega_0 < 6.9 \times 10^{-6}$ is shown by a solid bar denoted as “LIGO S5”. The upper limit is calculated from LIGO S5 data, using LIGO S4 result as a prior for Ω_0 and is valid for the frequency band 41.5-169.25 Hz [18]. The projected advanced LIGO sensitivity (aLIGO) is also shown here.

In addition to the cosmological background, an astrophysical contribution may have resulted from the superposition of a large number of unresolved astrophysical sources, whose frequency is expected to evolve very slowly compared to the observation time [21]. These can be either short-lived burst sources,

such as stellar core collapses to neutron stars or black holes, phase transition or quickly damped oscillation modes in young neutron stars, the final stage of compact binary mergers, or long-lived sources, typically non-axisymmetric rotating neutron stars, the early inspiral phase of compact binaries or captures of stellar mass compact objects by supermassive black holes.

Fig. 2.3 shows the gravitational wave spectra plotted as a function of observed frequency for potentially significant AGWBs and their detectability using the two upcoming advanced LIGO detectors. The detectability of an AGWB is determined by the detector sensitivity, which sets the detection horizon. As the sensitivity of LIGO improves and the next generation of GW observatories come on line, it is plausible that AGWBs can be observed for the first time, providing new insights into both the sources generating them and the evolutionary history of the universe.

2.1.1 The detector strain due to a SGWB

As we saw in Chapter 1, a gravitational wave is the propagation of a metric perturbation. In the transverse traceless gauge, the spatial part of the metric perturbations due to a SGWB can be written as a superposition of plane waves

$$h_{ab}(t, \mathbf{r}) = \int_{-\infty}^{\infty} df \int_{S^2} d\hat{\Omega} e_{ab}^A(\hat{\Omega}) \tilde{h}_A(f, \hat{\Omega}) e^{i2\pi f(t + \hat{\Omega} \cdot \mathbf{r}/c)}, \quad (2.1)$$

where a and b are spatial indices, $e_{ab}^A(\hat{\Omega})$ are the components of the gravitational wave polarization tensors, $A = \{+, \times\}$ is the polarization index, and $\hat{\Omega}$ is a unit vector pointing in the direction of wave propagation. Since the GW strain $h_{ab}(t, \mathbf{r})$ is real, the complex Fourier amplitudes $\tilde{h}_A(f, \hat{\Omega})$ satisfy the reality con-

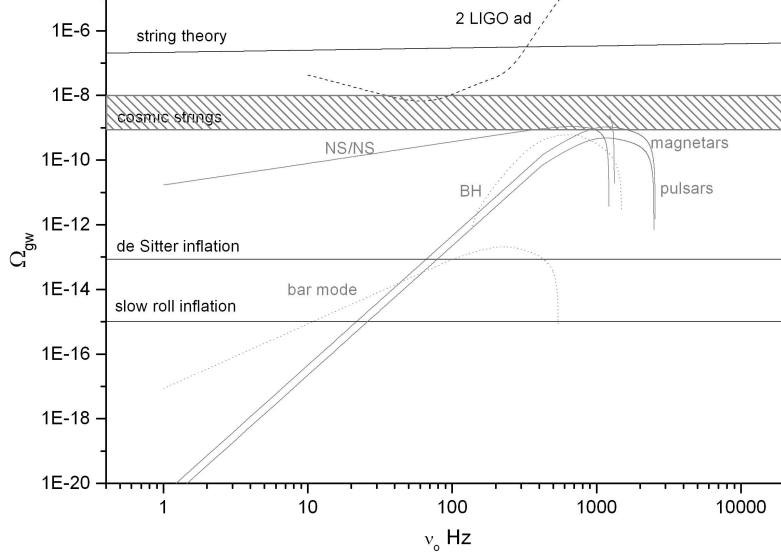


Figure 2.3: Gravitational wave spectrum as a function of observed frequency for potential AGWB sources [21]. Theoretical limits for several primordial GW background models are plotted as horizontal lines and the detection sensitivity from correlating two advanced LIGO type interferometers is shown as the dashed curve (labeled by “2 LIGO ad”).

dition, $\tilde{h}_A(-f, \hat{\Omega}) = \tilde{h}_A^*(f, \hat{\Omega})$.

The polarization tensors can be defined in terms of the spherical polar coordinates, $\theta \in [0, \pi]$, $\phi \in [0, 2\pi]$, on the sky. Let us define

$$\begin{aligned}
 \hat{\Omega} &= \sin \theta \cos \phi \hat{x} + \sin \theta \sin \phi \hat{y} + \cos \theta \hat{z} , \\
 \hat{m} &= \cos \theta \cos \phi \hat{x} + \cos \theta \sin \phi \hat{y} - \sin \theta \hat{z} , \\
 \hat{n} &= -\sin \phi \hat{x} + \cos \phi \hat{y} ,
 \end{aligned} \tag{2.2}$$

so that $\{\hat{m}, \hat{n}, \hat{\Omega}\}$ form a right-handed system of unit vectors. The axes are defined as follows: For a fixed but arbitrarily chosen origin of time $t = 0$, \hat{x} is directed towards the intersection of the equator and the longitude $\phi = 0$, \hat{z} points at the Celestial North Pole, and \hat{y} is chosen orthogonal to the previous two axes, forming a right-handed triad. Then, the polarization tensor components $e_{ab}^A(\hat{\Omega})$ are defined as

$$\begin{aligned} e_{ab}^+(\hat{\Omega}) &= \hat{m}_a \hat{m}_b - \hat{n}_a \hat{n}_b , \\ e_{ab}^\times(\hat{\Omega}) &= \hat{m}_a \hat{n}_b + \hat{n}_a \hat{m}_b . \end{aligned} \quad (2.3)$$

in the aforementioned right-handed orthogonal basis.

Understanding the signal excited in an interferometric detector by a SGWB is helped by specifying the detector's location and orientation in the above orthogonal basis. Let the I^{th} GW detector be located at $\mathbf{r}_I(t)$, and let $\hat{X}_I(t)$ and $\hat{Y}_I(t)$ be the unit vectors pointing along its arms. These three detector location and orientation vectors are all time-dependent due to the Earth's rotation. Then, the components of the I^{th} detector tensor are given by

$$d_I^{ab}(t) = \frac{1}{2} \left[\hat{X}_I^a(t) \hat{X}_I^b(t) - \hat{Y}_I^a(t) \hat{Y}_I^b(t) \right] , \quad (2.4)$$

and

$$h_I(t) = h_{ab}(t, \mathbf{r}_I(t)) d_I^{ab}(t) , \quad (2.5)$$

is the strain in it due to the SGWB.

The response of a detector to the polarization component A of a wave incident from direction $\hat{\Omega}$ is given by the antenna response function

$$F_I^A(\hat{\Omega}, t) = d_I^{ab}(t) e_{ab}^A(\hat{\Omega}) , \quad (2.6)$$

where we assumed the Einstein summation convention over the repeated indices a and b . Contracting Eq. (2.1) with the detector tensors d_I , the GW strain signal in the I^{th} detector can be expressed as

$$h(t) \equiv h_I(t) = \int_{-\infty}^{\infty} df \int_{S^2} d\hat{\Omega} \tilde{h}_A(f, \hat{\Omega}) F_I^A(\hat{\Omega}, t) e^{i2\pi f(t + \hat{\Omega} \cdot \mathbf{r}_I(t)/c)}, \quad (2.7)$$

in terms of the antenna response functions.

2.1.2 Statistical properties of the signal and detector noise

The intensity of a stochastic GW background is usually characterized by a dimensionless quantity, GW spectrum

$$\Omega_{\text{GW}}(f) := \frac{1}{\rho_c} \frac{d\rho_{\text{GW}}}{d \ln f}, \quad (2.8)$$

where $d\rho_{\text{GW}}$ is the energy density of the gravitational radiation in the frequency range f to $f + df$ and ρ_c is the critical energy density follows from the Friedman equation,

$$\begin{aligned} \rho_{\text{GW}} &= \frac{c^2}{32\pi G} \langle \dot{h}_{ab}(t, \mathbf{r}) \dot{h}^{ab}(t, \mathbf{r}) \rangle, \\ \rho_c &= \frac{3c^2 H_0^2}{8\pi G}, \end{aligned} \quad (2.9)$$

where H_0 is the Hubble expansion rate for today. Here, Ω_{GW} is not to be confused with the unit vector $\hat{\Omega}$ defined in Eq. (2.2).

The Fourier components of the strain $\tilde{h}_A(f, \hat{\Omega})$ describing a stochastic GW background are random variables whose expectation values define the statistical properties of the background. Without loss of generality we assume that these components have zero mean:

$$\langle \tilde{h}_A(f, \hat{\Omega}) \rangle = 0, \quad (2.10)$$

where the angular brackets denote statistical average. In the presence of a signal, the time series of the I^{th} detector's output $x_I(t)$ is a sum of the GW signal $h_I(t)$ and the detector noise $n_I(t)$:

$$x_I(t) = h_I(t) + n_I(t). \quad (2.11)$$

Statistically, the gravitational wave strain $h_I(t)$ is uncorrelated with the detector noise, implying that

$$\langle h_I(t) n_J(t') \rangle = 0, \quad (2.12)$$

for all I and J . We also assume that the noise is Gaussian with zero mean, i.e., $\langle n_I(t) \rangle = 0$, and is uncorrelated in different detectors, namely,

$$\langle n_I(f) n_J(f') \rangle = \frac{1}{2} \delta(f - f') \delta_{IJ} \tilde{\zeta}_{(I)}(f), \quad (2.13)$$

where $\tilde{\zeta}_{(I)}$ is the one-sided noise power spectral density (PSD) of the I^{th} detector. The last assumption is not unreasonable when the detectors are widely separated across the globe.

2.2 Principle of a GW radiometer

Radiometry or aperture synthesis is a well-known technique in radio astronomy and CMB experiments [22, 23]. The principle of earth rotation aperture synthesis can be used well for extracting the anisotropies of GW background using pairs of GW detectors [24]. Since the noise streams in different detectors are uncorrelated, the cross correlation between the outputs from a pair of detectors with an appropriate direction dependent filter is the best statistic for the estimation of the strength of stochastic signals that may be present in those outputs.

A gravitational wave radiometer can be thought of as a pair of GW detectors separated by a distance, termed as the baseline (see Fig. 2.4). Owing to the earth's rotation, the baseline vector changes direction while keeping its magnitude fixed and hence allows a time-dependent phase delay for a particular direction of the sky. This delay corresponds to the difference between the times of arrival between two detector sites of GW signals from that direction. The cross correlation of the data from the two detectors with appropriate time delays would cause potential GW signals interfere constructively from the same direction. Whereas signals from other directions will tend to cancel out because of destructive interference.

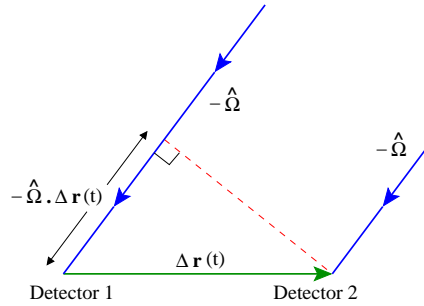


Figure 2.4: Geometry of an elementary GW radiometer [24].

In Fig. 2.4 two detectors are at locations \mathbf{r}_I (where, $I = 1, 2$), and the baseline vector joining the two sites is $\Delta \mathbf{r} := \mathbf{r}_2 - \mathbf{r}_1$. The unit vector $\hat{\Omega}$ is the direction to the source, which is fixed in the barycentric frame. The phase difference $-\hat{\Omega} \cdot \Delta \mathbf{r}(t)$ between signals arriving at two detector sites from the same direction is shown in the figure. The baseline vector $\Delta \mathbf{r}$ rotates with the rotation of the earth, while keeping its magnitude fixed. The modulation of the cross-correlation of the SGWB signals in the detector pair can be modelled for each

$\hat{\Omega}$. By searching for this modulation pattern in the detectors' data one can infer the nature and sky position of the source. A map of the SGWB can be, thus, constructed by performing this synthesis for each location in the sky, patch by patch. The sky resolution can be naively estimated from the diffraction formula $\Delta\theta \sim \lambda_{\text{GW}} / (|\Delta\mathbf{r}| \sin\theta)$, where λ_{GW} is the GW wavelength and θ is the angle of incidence. So, e.g., for $\lambda_{\text{GW}} = c/1000\text{Hz}$, $|\Delta\mathbf{r}| = 3000\text{km}$, and $\theta = 90^\circ$ (overhead source), $\Delta\theta \approx 0.1$ radians. A better estimate of the resolution follows from considerations involving the pixel-to-pixel Fisher information matrix [26, 13], in which case the solid-angle resolution scales inversely proportional to the square of the signal-to-noise ratio.

A variety of data analysis strategies to search for an anisotropic GW background have been proposed and implemented in the past [27, 28, 29, 30, 31, 32]. These searches are usually performed in one of two types of bases in the sky, namely, the pixel or spherical harmonic basis. Use of the radiometer technique for searching a GW background was proposed in Ref. [33] and was implemented in the pixel basis on data from LIGO's fourth science run [34]. An elaborate study of this method, including the maximum-likelihood (ML) estimation of the true anisotropy of GW background by deconvolving the observed sky map, was presented in [24]. Even though the pixel-based search is promising and simpler to understand, it is not the best basis for probing sources with angular spreads greater than the angular resolution of the GW radiometer. The spherical harmonic basis is expected to be better suited for detecting such sources [14]. Past attempts at probing the GW anisotropy in the spherical harmonic basis were essentially studies of the periodic modulation of the observed background in the

detector baselines. Recently, a general ML formalism was developed to search for the GW anisotropies in any basis, including the spherical harmonic basis, using a network of ground-based GW interferometers [14]. The pixel-based search is a specific application of this formalism. One of the main goals of this chapter is to perform a thorough comparison of the expected performances of individual baselines and the whole network in detecting an astrophysical stochastic gravitational wave background (SGWB) and in estimating its parameters. The pixel basis is used for this study.

Even though a pixel-based search is optimal for a localized source, the resolution of the source is limited by the length of the radiometer baselines, the orientation of the detectors, and their individual sensitivities. Probing a stochastic GW background with energy distributed across the pixelated sky demands a statistically meaningful integration of the energies received in every pixel. In order to accomplish this, we extend the maximized-likelihood ratio (MLR) statistic for a single baseline to incorporate a network of detectors or, equivalently, multiple baselines. The rest of the chapter is based on Ref. [13] and devoted to studying the performance of individual GW detector baselines and the whole network by comparing different figures of merit for their performance, e.g., sensitivity, accuracy in localizing sources, sky coverage, and faithful extraction from the data of the sky distribution of a stochastic background.

2.3 Optimal search statistic

2.3.1 Cross correlation statistic

Since the targeted source is stochastic, we search for its GW signal by looking for correlated patterns in the data of two or more detectors after accounting for time delays and detector responses consistent with a given sky location. This is done by cross-correlating the data $x_I(t)$ from the detectors, taken in pairs, with a sky-position-dependent time-frequency filter $\tilde{Q}^k(t; f)$, labeled by the sky-position index k . The cross correlation statistic combined for the observation period T for the data $x_{1,2}(t)$ from two detectors or, equivalently, for a baseline is defined as

$$S^k = 4 \Delta t \sum_{t=0}^T \int_{-\infty}^{\infty} df \tilde{x}_1^*(t; f) \tilde{x}_2(t; f) \tilde{Q}^k(t; f), \quad (2.14)$$

where $\tilde{x}_I(t; f)$ is the short-term Fourier transform of $x_I(t)$, over time interval Δt , and is defined as in Ref. [24] as

$$\tilde{x}_I(t; f) := \int_{t-\Delta t/2}^{t+\Delta t/2} dt' x_I(t') e^{-2\pi i f t'}. \quad (2.15)$$

The filter that maximizes the signal-to-noise ratio (SNR) associated with this statistic is a scalar, square-integrable function on the sky [24] and, hence, can be resolved linearly in an appropriate basis, such as a pixel basis or the spherical harmonic basis. In the former case, k is the pixel index. The SNR can be expressed in terms of the filter function and a multiplicative factor [35, 36]. One of the multiplicative factors is the square root of observation time. This multiplicative factor means that we can dig out a weak signal from noise by allowing a long enough observation time. The observation period could be from one

sidereal day to several months.

Let an astrophysical GW background be modeled such that the Fourier components of its GW strain $\tilde{h}_A^k(f)$ of polarization A from the k^{th} sky-position obey

$$\langle \tilde{h}_A^{k*}(f) \tilde{h}_{A'}^k(f') \rangle = \delta_{AA'} \delta(f - f') \delta^{kk'} \mathcal{P}_{(A)}^k H(f), \quad (2.16)$$

where $\mathcal{P}_{(A)}^k$ is a dimensionless measure of the signal strength, and $H(f)$ is its two-sided power spectral density, with units of Hz^{-1} [24]. Here, we assume the signal to be stochastic and uncorrelated in the two polarizations, different frequencies, and different sky locations. In the presence of a signal in the detector data, the cross correlation statistic is

$$S^k = \mathcal{B}_{+k'}^k \mathcal{P}_{(+)}^{k'} + \mathcal{B}_{\times k'}^k \mathcal{P}_{(\times)}^{k'} + n^k, \quad (2.17)$$

where the *beam function* $\mathcal{B}_{A k'}^k$ is analogous to the point-spread function that maps the power in the *object* (or sky) plane to that in the *image* plane. The exact form of the beam function is given in Eq. (2.22). The noise in the k^{th} sky position is n^k , and S^k is termed as the dirty map [24]. We define $\mathcal{P}_{(A)}$ as a vector, with $\mathcal{P}_{(A)}^k$ as its k^{th} component, and \mathcal{B}_A as a matrix, with $\mathcal{B}_{A k'}^k$ as its (k, k') th element.

2.3.2 Detection statistic

To get a single detection statistic, one must combine the measurements of S^k for all k . When the detector noises are Gaussian and uncorrelated, an assumption borne out to sufficient approximation for our purposes, the n^k are Gaussian with a nontrivial covariance matrix, \mathbf{N} , determined by the beam functions. The exact form of \mathbf{N} is discussed below.

If an astrophysical GW background signal, characterized by the pixel-strength vector \mathcal{P} , is present in the data, then the probability density function of the radiometer output \mathbf{S} is given by

$$p(\mathbf{S}|\mathcal{P}) = (2\pi)^{-N_{\text{pix}}/2} \exp\left[-\frac{1}{2}((\mathbf{S} - \mathcal{B} \cdot \mathcal{P})^T \cdot \mathbf{N}^{-1} \cdot (\mathbf{S} - \mathcal{B} \cdot \mathcal{P}) + \text{Tr}[\ln \mathbf{N}])\right], \quad (2.18)$$

whereas in the absence of a signal it is

$$p(\mathbf{n}) = (2\pi)^{-N_{\text{pix}}/2} \exp\left[-\frac{1}{2}(\mathbf{n}^T \cdot \mathbf{N}^{-1} \cdot \mathbf{n} + \text{Tr}[\ln \mathbf{N}])\right]. \quad (2.19)$$

By the Neyman-Pearson criterion, the optimal detection statistic is the likelihood ratio $p(\mathbf{S}|\mathcal{P})/p(\mathbf{n})$ [26].

For an unpolarized background from a source distributed across multiple pixels and quantified by the signal-strength vector $\mathcal{P} = \mathcal{P}_{(+)} = \mathcal{P}_{(\times)}$, the log-likelihood ratio maximized over $\mathcal{P} \equiv \|\mathcal{P}\|$ is

$$\begin{aligned} \lambda &= \frac{S^k (\mathbf{N}^{-1})_{kk'} (\mathcal{B} \cdot \hat{\mathcal{P}})^{k'}}{\sqrt{(\mathcal{B} \cdot \hat{\mathcal{P}})^q (\mathbf{N}^{-1})_{qr} (\mathcal{B} \cdot \hat{\mathcal{P}})^r}}, \\ &= \frac{S_k \hat{\mathcal{P}}^k}{\sqrt{\hat{\mathcal{P}}^q \mathcal{B}_{qr} \hat{\mathcal{P}}^r}}, \end{aligned} \quad (2.20)$$

where $\hat{\mathcal{P}}$ is the unit vector along \mathcal{P} . The beam matrix for an unpolarized source (see Fig. 2.5) is given by

$$\mathcal{B}_{pq} = \mathcal{B}_{+pq} + \mathcal{B}_{\times pq}, \quad (2.21)$$

$$\begin{aligned} &= 8 \Delta f \Delta t \sum_{t=0}^T \Gamma(\hat{\Omega}_q, t) \Gamma(\hat{\Omega}_p, t) \\ &\times \Re \left[\sum_{f=f_l}^{f_u} e^{2\pi i f (\hat{\Omega}_q - \hat{\Omega}_p) \cdot \Delta \mathbf{r}(t)/c} G(t, f) \right], \end{aligned} \quad (2.22)$$

where $\Gamma(\hat{\Omega}_q, t)$ is the time-varying baseline antenna-pattern, and $G(t, f)$ is a measure of the spectral strength of the source relative to the baseline's noise PSDs:

$$\Gamma(\hat{\Omega}, t) := F_1^+(\hat{\Omega}, t)F_2^+(\hat{\Omega}, t) + F_1^\times(\hat{\Omega}, t)F_2^\times(\hat{\Omega}, t), \quad (2.23)$$

$$G(t, f) := \frac{H^2(f)}{\bar{\xi}_{(1)}(t, f) \bar{\xi}_{(2)}(t, f)}. \quad (2.24)$$

Therefore the fractional energy density in gravitational waves $\Omega_{\text{GW}}(f)$ is related

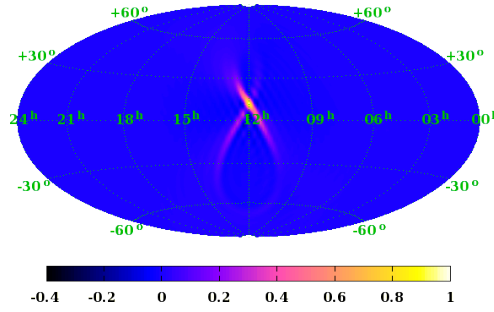


Figure 2.5: Illustration of a GW radiometer beam pattern at declination $+12^\circ$ for the LIGO detectors at Hanford and Livingston (with white noise, upper cutoff frequency of 1024 Hz, $H(f) = \text{constant}$ and observation time of one sidereal day). For low declination, the beam is shaped like the figure 8, while in the higher declination, the 8 smoothly turns into a tear drop [24].

to the strain power spectrum through ¹

$$\Omega_{\text{GW}}(|f|) = \frac{8\pi^2}{3H_0^2} |f|^3 H(f) \int_{S^2} d\hat{\Omega} \mathcal{P}(\hat{\Omega}). \quad (2.25)$$

¹For an *isotropic background* the directionality is set to unity, i.e., $\mathcal{P}(\hat{\Omega}) = 1$, which simplifies Eq. (2.25) by $\int_{S^2} d\hat{\Omega} \mathcal{P}(\hat{\Omega}) = 4\pi$.

In the weak-signal limit the noise-covariance matrix is approximately equal to the beam matrix,

$$N_{pq} \approx \mathcal{B}_{pq}. \quad (2.26)$$

Its diagonal elements inform us about the sensitivity of the network to the different pixels in the sky for an SGWB with PSD $H(f)$.

The statistic λ is the maximized (log-)likelihood ratio for a single-baseline SGWB search and is the same statistic introduced in Appendix C of Ref. [14]. Here, it is expressed specifically in terms of quantities defined in the pixel basis. It has zero mean and unit variance in the absence of a signal. When a signal is present in the data and its parameters are matched exactly by the template's, the mean of the statistic is

$$\langle \lambda \rangle = \mathcal{P} \sqrt{(\mathcal{B} \cdot \hat{\mathcal{P}})^k (\mathbf{N}^{-1})_{kk'} (\mathcal{B} \cdot \hat{\mathcal{P}})^{k'}}. \quad (2.27)$$

The variance of the statistic remains unchanged. One can extend this single-baseline statistic to the case of a multibaseline network. That statistic arises directly from maximizing the log-likelihood ratio for a network and is given by

$$\begin{aligned} \lambda_{\mathcal{N}} &= \frac{\sum_{\mathcal{I}=1}^{N_b} S_{\mathcal{I}}^k (\mathbf{N}_{\mathcal{I}}^{-1})_{kk'} (\mathcal{B}_{\mathcal{I}} \cdot \hat{\mathcal{P}})^{k'}}{\sqrt{\sum_{\mathcal{I}=1}^{N_b} (\mathcal{B}_{\mathcal{I}} \cdot \hat{\mathcal{P}})^q (\mathbf{N}_{\mathcal{I}}^{-1})_{qr} (\mathcal{B}_{\mathcal{I}} \cdot \hat{\mathcal{P}})^r}}, \\ &= \frac{\sum_{\mathcal{I}=1}^{N_b} S_{\mathcal{I}}^{\mathcal{I}} \hat{\mathcal{P}}^k}{\sqrt{\sum_{\mathcal{I}=1}^{N_b} \hat{\mathcal{P}}^q \mathcal{B}_{qr}^{\mathcal{I}} \hat{\mathcal{P}}^r}}, \end{aligned} \quad (2.28)$$

where \mathcal{I} is the baseline index and the subscript \mathcal{N} highlights that this MLR statistic is for a *network* of baselines.

The MLR statistic is a detection statistic for SGWBs in the same manner as the standard matched-filter statistic is for deterministic GW sources. The latter

is also obtained by maximizing the likelihood ratio with respect to the strength of the deterministic source. Searching for a signal from a deterministic source involves maximizing the matched-filter statistic over a bank of templates defined on the signal’s parameter space. For SGWBs, as well, the detection statistic can be the MLR, maximized further with respect to different SGWB models given by $\hat{\mathcal{P}}$, perhaps parametrized by a smaller number of parameters than the number of components of $\hat{\mathcal{P}}$. This is in contrast to the existing searches for anisotropic GW backgrounds. Past dirty-map-based searches precluded the presence of a signal by demonstrating that the map is consistent with a Gaussian distribution, up to statistical fluctuations allowed by the number of independent “samples” on the sky [34]. However, they did not provide a confidence level for the presence or absence of a broadband or spatially extended signal. A better approach is to solve the inverse problem in an orthogonal basis, namely, the pixel [24] or spherical harmonic [14] basis. This yields an estimate of the background, i.e., a “clean” (deconvolved) map and the corresponding noise-covariance matrix. However, this approach depends heavily on how well-posed the inverse problem is and how accurately it can be implemented numerically. Consequently, a detection statistic constructed on the deconvolved data can be affected by similar maladies. To work well, the inverse problem requires that the network of interferometers is sufficiently nondegenerate, which is not always the case. Indeed, the deconvolution procedure can enhance spatial noise correlations and, sometimes, even introduce artifacts, thereby adversely affecting parameter estimation and signal detection by such a procedure.

As we prove here, the detection problem does not require a well-posed in-

verse problem and exists even for a degenerate network. A detection statistic is best defined on the dirty map, as opposed to the clean map. As an added advantage, a dirty-map-based statistic is faster to compute, since it obviates the computational overhead required for obtaining the clean map. While it is possible to use an arbitrary sky model, such as the *one-dimensional* basis $\hat{\mathcal{P}}$, and estimate the strength of the SGWB for that particular model, the MLR statistic in Eq. (2.20) provides a well-understood construct that can be maximized over a set of parameters for selecting the model that best fits the data.

To elaborate further on the way the new statistic works, let us consider the example of a directed pixel-space search, which is performed for only one source and assumes that the angular extent of the source is, at most, one pixel. In the standard radiometer search [25, 24], the dirty map S^k is computed for each pixel k in the sky. The (signal part of the) dirty map is generally peaked at the source pixel and has broad structures, including large negative patches, around it. One way of inferring the presence or absence of a source in this image requires deconvolving it. However, as we show later, deconvolution of a relatively weak source can result in a clean map with significant errors, especially when the sky is divided into around 3000 pixels or more. (A network resolution of several square degrees requires a few thousand pixels across the sky.) Also, computing the noise-covariance matrix can be numerically challenging. The MLR is a good choice in this situation, since it combines all the pixel values to provide a single number for the detection statistic that is simple to use in drawing inferences on the presence or absence of a signal in the network data.

If a parametrized model of the background is available, one can construct the

likelihood-ratio statistic from the dirty map and maximize it over the parameter space. The maximized likelihood-ratio statistic can also be used to perform a more advanced blind search, where no prior information is available about angular distribution of the power in the SGWB. For each basis component, one can assert that only that basis component is present in the signal and compute the statistic with the corresponding sky model. Thus, using the dirty maps of “point estimate” or SNR obtained by the existing radiometer search, our prescription takes one step forward and can provide a map of likelihood ratios, which is statistically a more robust and meaningful quantity, given a set of highly correlated observations.

The construction of the MLR statistic on a dirty map is simple. Eq. (2.20) shows that it is the scalar product of the observed map S^k and a sky-model-dependent normalized “template.” The template is proportional to $\mathcal{B} \cdot \mathcal{P}$, which is the expected signal in the dirty map for a sky model $\hat{\mathcal{P}}$. The inverse of the noise-covariance matrix is the metric in the pixel space. The sky model can be defined in a straightforward way. For instance, to search for a point source localized to a single pixel, one would use a $\hat{\mathcal{P}}$ with all but one component, namely, the component corresponding to that pixel, set to zero. Indeed, $\mathcal{B} \cdot \mathcal{P}$ is simply the point-spread function of the pixel with the nonzero component of $\hat{\mathcal{P}}$. Also notice that the inverse of the noise-covariance matrix, being proportional to the beam matrix, cancels out algebraically in the expression for the MLR. Therefore, unlike for deconvolution, for MLR construction the computation of this matrix is not needed. Otherwise, the latter procedure would have been computationally similar to solving the inverse problem, avoiding which is one

of the main motivations for this work.

To complete the discussion, we note that the construction of a MLR statistic is not limited to dirty maps and can be implemented for clean maps. A clean map can be expressed as

$$\tilde{\mathcal{P}} = \mathcal{P} + \mathbf{n}_c, \quad (2.29)$$

where \mathcal{P} is the true sky map, and \mathbf{n}_c is Gaussian noise with covariance Σ , which is related to the dirty-map noise-covariance matrix through the relation $\Sigma = (\mathcal{B}^T \mathbf{N}^{-1} \mathcal{B})^{-1}$. Therefore, following the same procedure as that for the dirty map, one can write the MLR statistic for a clean map as

$$\lambda_c = \frac{\tilde{\mathcal{P}} \cdot \Sigma^{-1} \cdot \mathcal{P}}{\sqrt{\mathcal{P} \cdot \Sigma^{-1} \cdot \mathcal{P}}}, \quad (2.30)$$

and, thereby, obtain model-based or blind likelihood-ratio maps.

2.3.3 Performance of optimal detection statistic

We numerically study the performance of the optimal statistic and compare with the existing method. We use the LIGO 4km detectors located in Hanford (H1) and Livingston (L1). Unless otherwise stated, the noise PSDs of all detectors are taken to be their (smoothed) first-generation design sensitivities as shown in the solid curves of Fig. 2.6. The frequency band considered here spans 40 – 1024Hz, with a bin size $\Delta f = 1\text{Hz}$. The source PSD is taken to be a constant, $H(f) = 1.516 \times 10^{-48}/\text{Hz}$. Note that the spectral index of the source PSD has a significant effect on the resolution of the network. Predictions from astrophysical and cosmological models suggest the nominal range of the spectral index to be between -3 and 1 . The higher the spectral index, the higher the resolution, and

the more computationally expensive the directed search. We take the spectral index to be zero here by setting $H(f)$ as a constant.

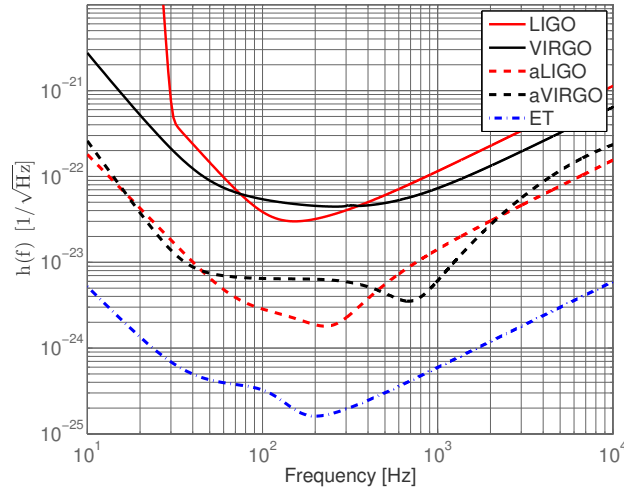


Figure 2.6: Designed noise amplitude spectrum of the initial LIGO and VIRGO (solid curves), advanced LIGO and VIRGO (dashed curves), and the Einstein Telescope (dotted-dashed curve) [39, 40, 41].

The directed search is performed by dividing the (simulated) strain data from all detectors into segments with a duration of 192 sec. The noise is taken to be stationary. The sky is tessellated into 3072 pixels by using the Hierarchical Equal Area isoLatitude Pixelization [37, 38]. The choice of the signal integration duration is taken to be a sidereal day, which leads to the azimuthal symmetry of the baseline sensitivities and sky resolutions. The justification for choosing the above parameter values can be found in [24].

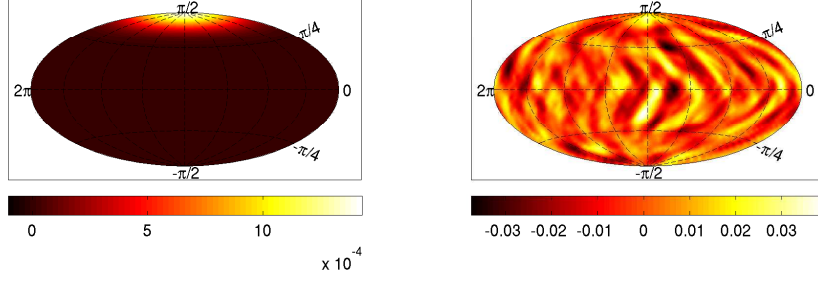
We first construct simulated data sets of two kinds, one with only noise and the other with a weak signal from a “polar-cap” source added to that noise. The sky map of the latter case is shown in the first plot in Fig. 2.7. We make dirty

maps for these two cases using single-pixel source templates for each of the 3072 pixels. These maps are essentially the maps of SNR for the directed search, as can be seen by substituting

$$\hat{\mathcal{P}}^k = \begin{cases} 1 & \text{for target pixel,} \\ 0 & \text{for remaining pixels,} \end{cases} \quad (2.31)$$

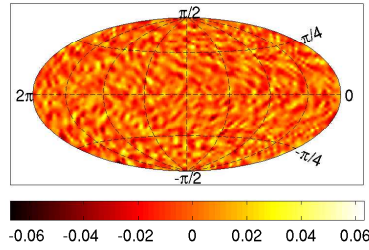
into Eq. (2.20) [24]. The dirty maps for both cases look very similar, and only one of them, namely, the one for the polar-cap source, is shown in the second plot of Fig. 2.7. Not surprisingly, it is also similar to the dirty map presented in [34] for real data. Indeed, the MLR values over the dirty-map pixels appear to follow a normal distribution, as shown in Fig. 2.8. This is consistent with the distribution presented in [34]. Following that reference, we also plot the 1σ error envelope around the Gaussian fit for 400 degrees of freedom and observe that the tops of every bar in the histogram lie within that envelope. The important point to note here is that, for both noise-only and weak-signal (polar-cap) data sets the distributions in Fig. 2.8 are very similar and consistent with a normal distribution.

If we now pretend that we know the broad shape of the GWB sky and use the $\hat{\mathcal{P}}^k$ of the polar-cap signal as our template for computing the MLR statistic, we find that the above two cases can be distinguished better: In the noise-only case, the MLR statistic equals -0.023 , while with the weak polar-cap signal it is 1.400 , which is significantly larger than the former, as explained below. To corroborate this claim, we computed the MLRs on an ensemble of 4000 realizations of noise, with and without the weak polar-cap signal. In Fig. 2.9, we show the distribution of the MLR statistic (λ) for noise-only (top) and weak-signal (bot-



(a) Injected map

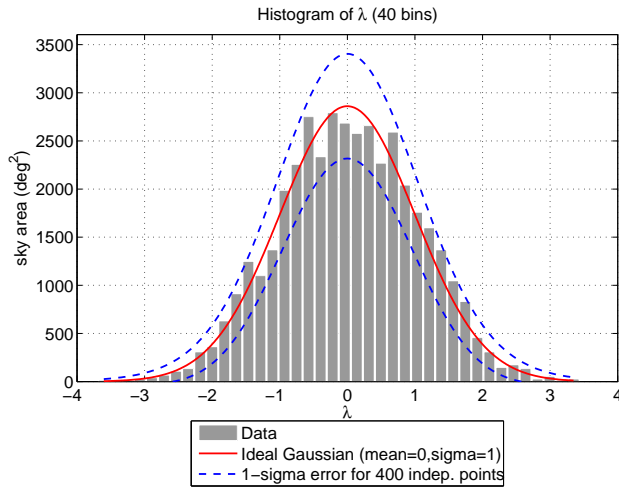
(b) Dirty map



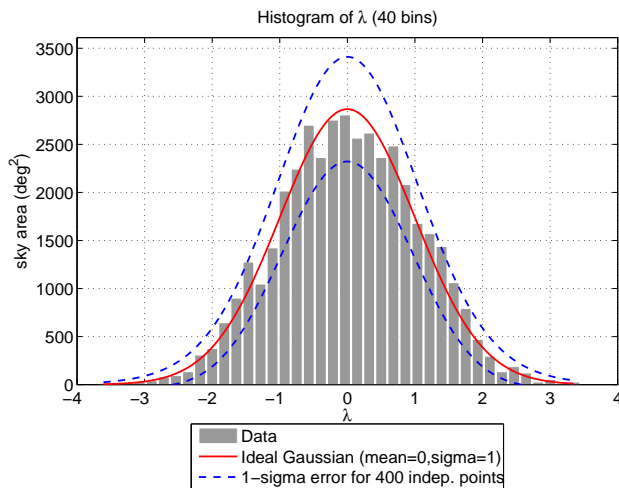
(c) Clean map

Figure 2.7: The \mathcal{P}^k sky map of a weak polar-cap GWB source is shown in (a). The dirty (b) and clean (c) maps for this source were constructed using the radiometer algorithm for the LIGO H1L1 baseline. The last two maps for this weak source are visually very similar to those for the noise-only case (which is not shown here).

tom) cases. Clearly, the noise-only λ values are normally distributed with a zero mean, and the weak-signal λ values are normally distributed with a mean of $\sim 1.4\sigma$, where $\sigma \approx 1$. This experiment confirms that, given our assumptions on the detector noise and the signal, the MLR statistic can considerably enhance the detectability of a weak diffuse stochastic background, if a reasonable model

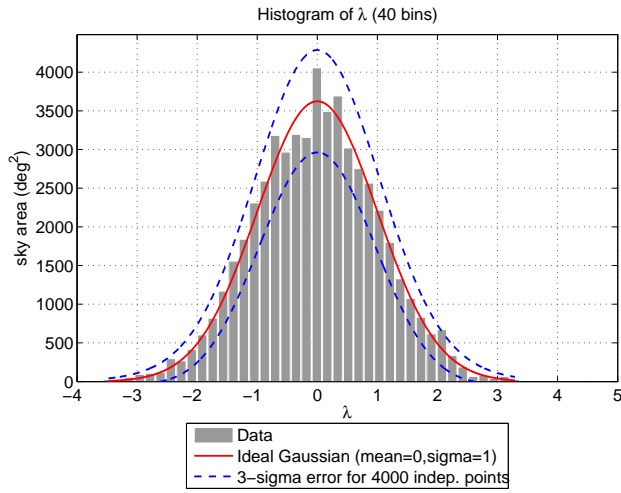


(a) Noise

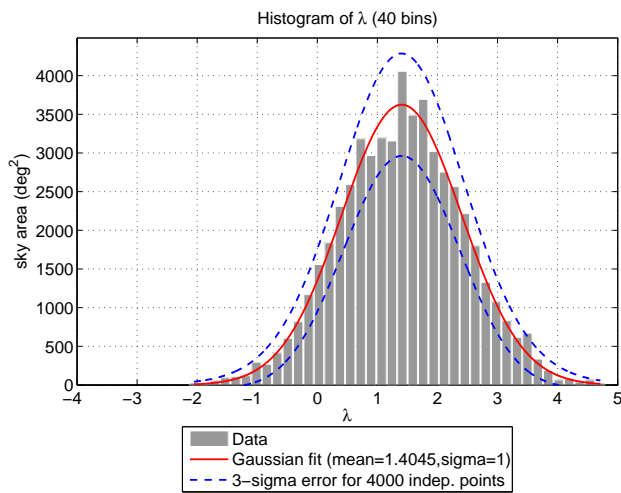


(b) CAP

Figure 2.8: Histograms of the dirty maps for the noise-only data set (top) and weak polar-cap signal (bottom), which is depicted in Fig. 2.7, are shown here. These two histograms are consistent with that of zero-mean Gaussian data (solid curved line), up to 1σ errors: Following [34], the 1σ error boundaries for 400 degrees of freedom have also been overlaid for a consistency check.



(a) Noise



(b) CAP

Figure 2.9: Monte Carlo simulations with 4000 noise realizations were performed to study the performance of the MLR statistic. The distribution of the MLR statistic obtained for dirty maps generated from noise-only (top) and weak polar-cap injection (bottom) are shown. Clearly, the MLR statistic detects the signal at $\sim 1.4\sigma$ level. Notice that the “CAP” histogram has shifted to the right.

of the background is available. This is true even when the distribution of the dirty-map pixel values for that source is close to zero-mean Gaussian.

2.4 Performance of multi-baseline radiometers

In this section we define a set of figures of merit to compare the performance of a network of baselines with that of its individual baselines for a directed search of a SGWB.

A single figure of merit may not suffice in capturing all the attributes of a baseline or a network of detectors benefiting a SGWB search. A certain baseline or network configuration can have good sensitivity if the detectors are optimally oriented, but have poor resolution if they are proximally located. Optimally oriented detectors may be very sensitive to certain anisotropy modes, but insensitive to others, making the estimation problem highly degenerate. On the other hand, a network of detectors that are oriented differently may have moderate, yet uniform, sensitivity to all spherical harmonic modes of a SGWB, thereby mitigating the ill-posedness of the estimation problem. Such a network, however, will perform worse than one where all the detectors are aligned similarly in a low-frequency, all-sky isotropic search. Therefore, the relevance of a figure of merit is determined by the kind of search one is undertaking. Here, we propose a set of figures of merit that are relevant to current searches of anisotropic stochastic background and that are special cases of the general ML framework presented in [14].

For the numerical simulation studies below, we use the same detector char-

acteristics as mentioned in Sec. 2.3.3, but we now include the Virgo detector (V1) in Cascina, Italy to construct a three-baseline network. The baselines and their network are named by concatenating the symbols for the participating detectors; e.g., the Hanford-Livingston baseline is termed as H1L1, and the network of the above three detectors is termed as H1L1V1. A similar study for the second and third generation detectors is presented in Appendix B.1.

2.4.1 Sensitivity

The first figure of merit is the “sensitivity” of a network and is motivated by a similar quantity defined in [42] for the all-sky isotropic search. In practice, a greater sensitivity implies a better confidence level, at which detection can be made or upper limits can be inferred.

We define the single-baseline sensitivity for a directed search as the expectation value of the MLR in Eq. (2.27) for a SGWB source with \mathcal{P} set to unity,

$$\begin{aligned} \text{Sensitivity} &= \sqrt{(\mathcal{B} \cdot \hat{\mathcal{P}})^k (\mathbf{N}^{-1})_{kk'} (\mathcal{B} \cdot \hat{\mathcal{P}})^{k'}}, \\ &= \sqrt{\hat{\mathcal{P}}^k \mathcal{B}_{kk'} \hat{\mathcal{P}}^{k'}}. \end{aligned} \quad (2.32)$$

The sensitivity can be expressed in the spherical harmonic basis as follows:

$$\text{Sensitivity} = \sqrt{\mathcal{P}_{lm} \mathcal{B}^{lm l' m'} \mathcal{P}_{l' m'}}, \quad (2.33)$$

where

$$\mathcal{P}_{lm} = \int d\hat{\Omega} \hat{\mathcal{P}}(\hat{\Omega}) Y_{lm}^*(\hat{\Omega}), \quad (2.34)$$

$$\mathcal{B}_{lm l' m'} = \int \int d\hat{\Omega} d\hat{\Omega}' Y_{lm}^*(\hat{\Omega}) \mathcal{B}(\hat{\Omega}, \hat{\Omega}') Y_{l' m'}(\hat{\Omega}'). \quad (2.35)$$

Owing to the statistical independence of the baselines, the multibaseline sensitivity squared is the sum of squares of the individual baseline sensitivities, as was also noted for the isotropic-background baseline sensitivities in [42]:

$$\text{Sensitivity}_{\mathcal{N}}^2 = \sum_{\mathcal{I}} \text{Sensitivity}_{\mathcal{I}}^2 . \quad (2.36)$$

For an unpolarized background from a single pixel, say, labeled k , and with $\hat{\mathcal{P}}^r = \delta^{r(k)}$, the sensitivity expression simplifies to

$$\text{Sensitivity}_{(k)} = \sqrt{\mathcal{B}^{q(k)} (\mathbf{N}^{-1})_{qr} \mathcal{B}^{r(k)}} = \sqrt{\mathcal{B}^{(k)(k)}} . \quad (2.37)$$

Unless otherwise mentioned, there is no sum over the repeated parenthetic indices in this chapter.

In the top panel of Fig. 2.10, we compare the sensitivities of the baselines and the whole network as a function of declination. (As noted above, the sensitivities are azimuthally symmetric.) For a fair comparison, we also replot them after weighting them with the cosine of the latitude, in effect, to assign equal weight to every pixel on the sky. It is clear that the H1L1 baseline has much better sensitivity due to the similar orientations of the two detectors. Still, inclusion of Virgo, which is oriented quite differently relative to H1 and L1, improves the sensitivities of the network by $\sim 10\%$ (which corresponds to an increase in the observational volume by $\sim 30\%$), especially in the regions where the H1L1 baseline does not perform well. However, this network improvement is highly superseded by all other performance improvements indicated by corresponding figures of merit introduced in this section.

In Fig. 2.11 we plot the narrowband (5Hz) sensitivities at two locations, namely, the Celestial North Pole (top) and the equator (bottom). Performance

improvement of a network for a narrow band search at high frequencies is better than the (frequency integrated) broadband search.

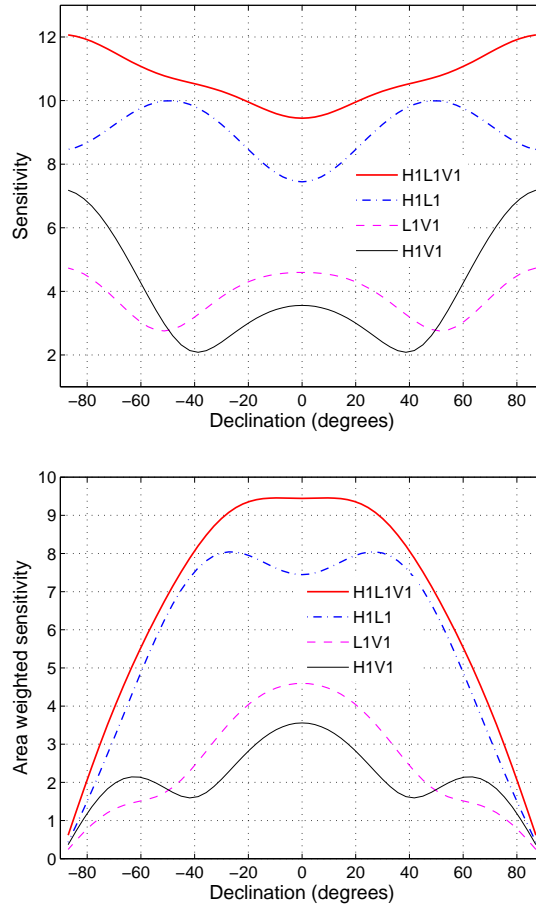


Figure 2.10: The sensitivities (top) and their area-weighted counterparts (bottom) of three different baselines and their network are plotted as functions of the declination of a single-pixel SGWB source. The source PSD ($H(f) = 1.516 \times 10^{-48}$ strain/Hz) is chosen such that it has maximum SNR= 10 in the H1L1 baseline. (Note that the source parameter \mathcal{P} is set to unity for these plots.) The signal band considered here is 40-1024 Hz.

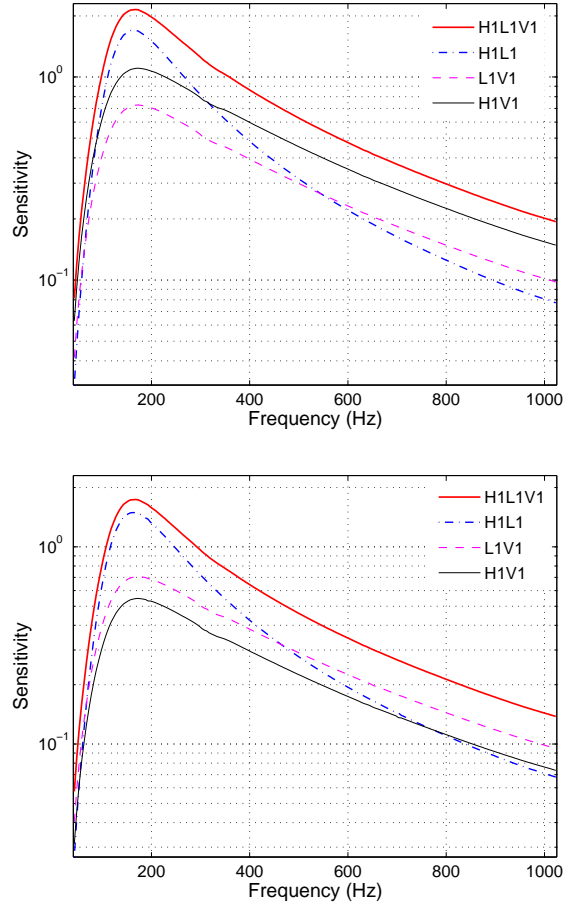


Figure 2.11: The sensitivities of three single baselines and their multibaseline network plotted as functions of the central frequency of the source band. The source is chosen to have a constant $H(f) = 1.516 \times 10^{-48}$ strain/Hz and a band width of 5Hz. The top panel represents the sensitivities at the celestial poles, and the bottom panel represents those at the celestial equator.

2.4.2 Sky coverage

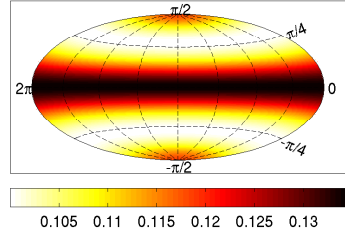
In a directional search, the main advantage of a network lies in the fact that it vastly improves sky coverage, which, in turn, leads to better parameter estima-

tion, including localization and sky-map reconstruction considered later in this section. In this subsection, we illustrate the advantage of using a network of detectors, as compared to using its individual baselines, to this end.

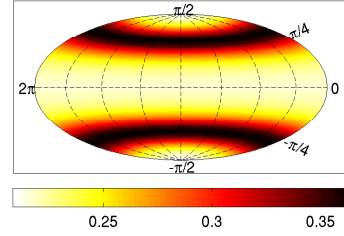
In general, one radiometer baseline cannot sample the whole sky uniformly; the measurement errors in some parts of the sky are much worse than those in the other parts. Introduction of new baselines with different orientations improves filling in these “holes” by scanning the sky with different antenna-pattern functions. In the first three plots in Fig. 2.12, we show the standard deviation in measuring the dirty map by the three individual baselines, namely, H1L1, H1V1, L1V1, and their network H1L1V1². The azimuthal symmetry mentioned before is explicitly observed here. The H1L1 baseline has the least deviation at most declinations, due to the optimal orientations of the H1 and L1 detectors. Again, H1V1 and L1V1 baselines have low deviation in the regions where H1L1 does not perform well. Since the dirty maps from different baselines are operationally combined with an inverse-noise-variance weight, the harmonic mean of the variances provides the effective variance of the combined dirty map. The last plot in Fig. 2.12 shows the effective deviation for a network of detectors. Clearly, the deviation now has smaller spread and also, by construction (harmonic mean), the deviations are smaller than those for the individual baselines.

Most importantly, a network also complements the single-baseline observations in terms of angular resolution. The beam functions for each radiometer baseline are highly asymmetric, which means that a given position on the sky is

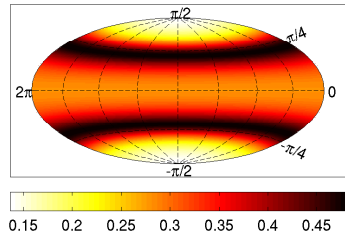
²The absolute scales of the plots are not important since the emphasis here is on relative performance of the different baselines and their network.



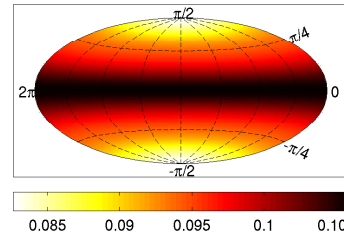
(a) H1L1



(b) L1V1



(c) H1V1



(d) H1L1V1

Figure 2.12: The standard deviation of dirty maps measured by the three LIGO-Virgo baselines and the full network for a constant $H(f)$ are plotted here. The aim of this figure is to show how individual baselines complement each other, thereby making the “effective deviation” (i.e., the square root of the harmonic mean of variances of the individual baselines) of the combined map observed by the network nearly uniform. Note that the color scale in the network plot has lesser spread than the individual baselines. The absolute scale of the maps depends on the normalization of the filter, and only the relative scale is important here. The azimuthal symmetry is present because we are considering a whole sidereal day’s observation, with stationary noise.

probed with quite different angular resolutions in the tangential directions. To illustrate this aspect, the typical beam functions for the three LIGO-Virgo baselines in the direction of the Virgo cluster are shown in Fig. 2.13. If we consider the beam for the H1L1 baseline, the sensitive part of the beam is similar to a highly eccentric ellipse, suggesting that the angular resolution along the minor axis is much finer than that along the major axis. The beams for the baselines in a network involving the Virgo detector provide better resolution due to the longer baselines: The beams are finer along the major axis of the H1L1 beam, thus complementing the H1L1 observation, which is a major motivation for using a network. This, in turn, improves the condition number of the Fisher information matrix, thereby, reducing the numerical errors in the anisotropy estimation problem at “high” resolution, i.e., near or beyond the diffraction limited resolution, and significantly improves source localization accuracy.

Singular value decomposition of the Fisher information matrices provides a more quantitative verification of the above claim. Figure 2.14 shows the singular values of the Fisher matrices for the individual baselines and the whole network. The LIGO baseline has very small singular values at higher resolutions (dashed curved line), which implies that estimation of anisotropy at those resolutions is an ill-defined problem. The network reduces the difference between high and low singular values and regularizes the inverse problem at high resolution (solid curved line).

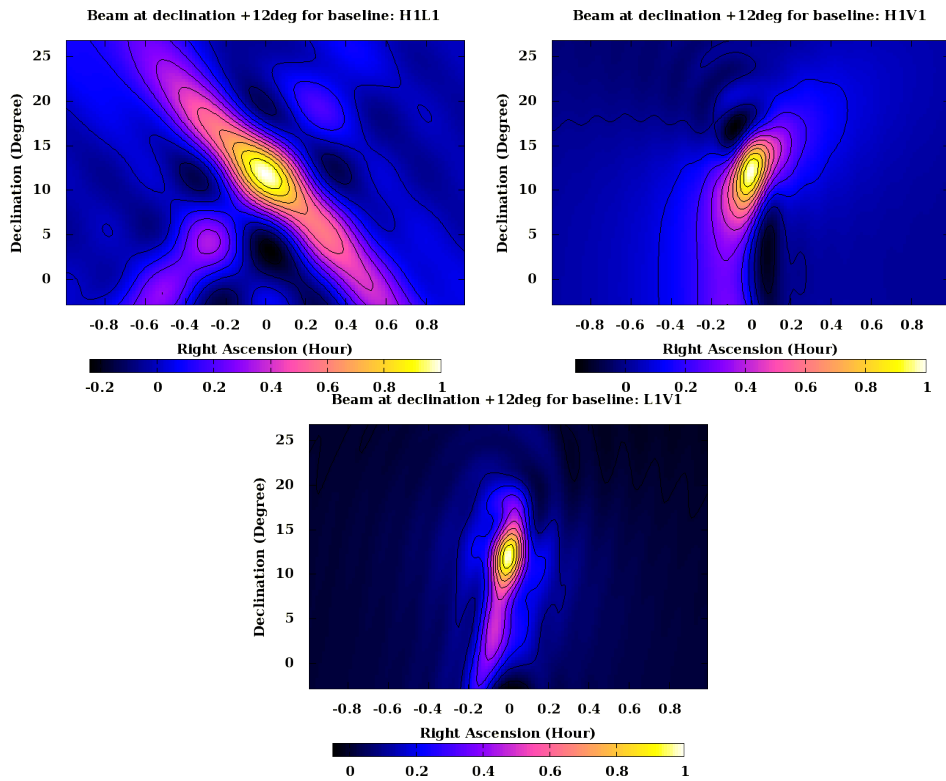


Figure 2.13: The beam functions for the three LIGO-Virgo baselines for $H(f) = \text{constant}$ are shown here. This figure illustrates that different baselines also complement each other in terms of angular resolution along different tangential sky directions.

2.4.3 Parameter accuracy

An important figure of merit for a directed search is how well a point source can be localized or its other parameters be constrained. In a noise-dominated mapping experiment, it is not easy to identify sources in the observed images. If there are candidate sources that have been modeled by other astronomical observations, one can utilize that information to detect or constrain parameters

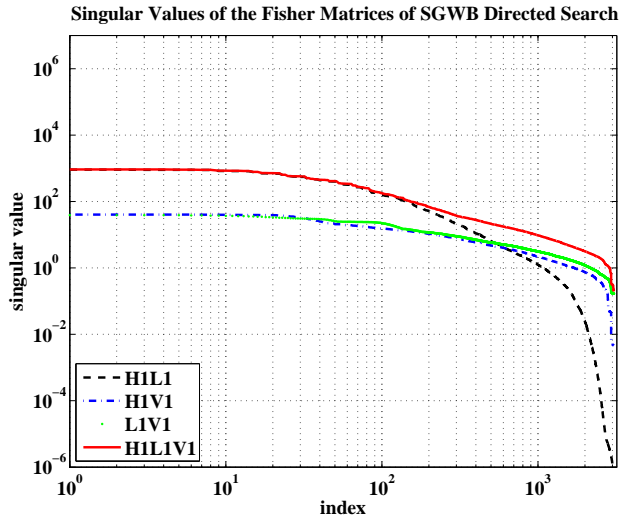


Figure 2.14: Singular values of the Fisher matrices for individual baselines and the whole network are plotted in this figure. The LIGO H1L1 baseline (dashed curved line) has very small singular values at high resolutions; therefore, estimation of anisotropy at those resolutions is an ill-defined problem. The network (solid curved line) makes the singular values much more uniform, thereby regularizing the inverse problem.

of such sources. If the source was very accurately modeled, the optimal strategy would be to design a specific search focused on that source. But, in practice, with very limited knowledge of sources, the optimal strategy would be to vary the parameters within a reasonable range and maximize the log-likelihood ratio.

One of the main advantages of the MLR statistic is that it allows estimation of parameters of the source, given a model. For example, if there is an extended source, such as a cluster of galaxies, with an angular scale comparable to the resolution of the radiometer, and there exists a reasonable model for its mass

distribution, one can maximize the log-likelihood ratio to find the center of the cluster ³. Even for a blind search, this method may prove to be advantageous to perform a finer search around the poorly estimated parameters of a potential candidate source.

In this section, we assess the accuracy with which a pointlike (single-pixel) source can be located using a network of GW detectors as compared to its individual baselines. The parameter estimation accuracy is deduced from the elements of the Fisher information matrix [26].

For an unpolarized background from a single pixel, labeled k , and with $\hat{\mathcal{P}}^r = \delta^{r(k)}$, the single-baseline detection statistic follows from Eq. (2.20) to be

$$\lambda_{(k)} = \frac{S^p (\mathbf{N}^{-1})_{pq} \mathcal{B}_{(k)}^q}{\sqrt{\mathcal{B}_{(k)}^r (\mathbf{N}^{-1})_{rs} \mathcal{B}_{(k)}^s}}, \quad (2.38)$$

which can be interpreted as the inner product of the data, \mathbf{S} , and a unit-norm template $\hat{\mathcal{B}}_k$. Hence, the *match* [43] between the unit-norm templates for the k^{th} and the k'^{th} pixels is

$$\begin{aligned} M &= \frac{\mathcal{B}_{(k)}^p (\mathbf{N}^{-1})_{pq} \mathcal{B}_{(k')}^q}{\sqrt{\mathcal{B}_{(k)}^r (\mathbf{N}^{-1})_{rs} \mathcal{B}_{(k)}^s} \sqrt{\mathcal{B}_{(k')}^{r'} (\mathbf{N}^{-1})_{r's'} \mathcal{B}_{(k')}^{s'}}}, \\ &= \frac{\mathcal{B}_{(k)(k')}}{\sqrt{\mathcal{B}_{(k)(k)}} \sqrt{\mathcal{B}_{(k')(k')}}}, \end{aligned} \quad (2.39)$$

where the inner products are all defined in terms of \mathbf{N}^{-1} . Define $\Theta_{(k)} \equiv \{\mu_k, \phi_k\}$ as the pixel coordinates, where $\mu_k \equiv \cos \theta_k$, with θ_k and ϕ_k being the declination and right ascension of the k^{th} pixel, respectively. Since the *match* has a maximum

³Note that the image of the source may be too faint to be visually prominent in the dirty or clean maps.

value of unity at $k' = k$, one can expand M in a Taylor series about $\Delta\mu_{(k)} = 0$ and $\Delta\phi_{(k)} = 0$ as

$$\begin{aligned} M &\approx 1 + \frac{1}{2} \left(\frac{\partial^2 M}{\partial \Theta_{(k')}^\mu \partial \Theta_{(k')}^\nu} \right) \Big|_{\Theta_{(k')} = \Theta_{(k)}} \Delta\Theta_{(k)}^\mu \Delta\Theta_{(k)}^\nu, \\ &\approx 1 - \frac{\Gamma_{(k)\mu\nu}}{(\text{SNR})_{(k)}^2} \Delta\Theta_{(k)}^\mu \Delta\Theta_{(k)}^\nu, \end{aligned} \quad (2.40)$$

where $\Gamma_{(k)\mu\nu} \equiv \Gamma_{\mu\nu}(\Theta_{(k)})$ are the components of the Fisher information matrix $\mathbf{\Gamma}_{(k)}$, and $(\text{SNR})_{(k)}$ is the signal-to-noise ratio in the k^{th} pixel.

For large SNR, the error variance-covariance matrix obeys

$$\left(\mathbf{\Gamma}_{(k)}^{-1} \right)^{\mu\nu} \approx \left\langle \Delta\Theta_{(k)}^\mu \Delta\Theta_{(k)}^\nu \right\rangle. \quad (2.41)$$

The estimation error in the measurement of the sky-position solid angle (in steradians) is given by [44]⁴

$$\Delta\Omega_{(k)} = 2\pi \sqrt{\left\langle (\Delta \cos \theta_{(k)})^2 \right\rangle \left\langle (\Delta\phi_{(k)})^2 \right\rangle - \left\langle \Delta \cos \theta_{(k)} \Delta\phi_{(k)} \right\rangle^2}. \quad (2.42)$$

The Fisher information matrix for multiple baselines is just the sum of the Fisher matrices for the individual baselines,

$$\left[\mathbf{\Gamma}_{(k)\mu\nu} \right]_{\mathcal{N}} = \sum_{\mathcal{I}} \Gamma_{\mathcal{I}(k)\mu\nu}, \quad (2.43)$$

where \mathcal{I} is the baseline index, and $\Gamma_{\mathcal{I}(k)\mu\nu}$ is the Fisher information matrix of the \mathcal{I}^{th} baseline, as given in Eq. (2.40). Hence, the error variance-covariance matrix for the network is

$$\left(\left[\mathbf{\Gamma}_{(k)} \right]_{\mathcal{N}}^{-1} \right)^{\mu\nu} \approx \left\langle \Delta\Theta_{(k)}^\mu \Delta\Theta_{(k)}^\nu \right\rangle_{\mathcal{N}}, \quad (2.44)$$

⁴See Appendix A.2 for the detailed expression in terms of beam function and its derivatives.

for large SNR. Therefore, the 1σ estimation error in solid angle for locating a pixel source with the multibaseline network is expressed as

$$\left[\Delta\Omega_{(k)}\right]_{\mathcal{N}} = 2\pi\sqrt{\left\langle(\Delta\cos\theta_{(k)})^2\right\rangle_{\mathcal{N}}\left\langle(\Delta\phi_{(k)})^2\right\rangle_{\mathcal{N}} - \left\langle\Delta\cos\theta_{(k)}\Delta\phi_{(k)}\right\rangle_{\mathcal{N}}^2}. \quad (2.45)$$

Note that this error diminishes with SNR as $1/\text{SNR}^2$, i.e., localization is more accurate at higher SNR.

We present the source-localization errors for the individual LIGO-Virgo baselines and the network in the top panel of Fig. 2.15. We also show the corresponding area-weighted plots obtained by multiplying these errors with the cosine of the latitudinal angle in the bottom panel of Fig. 2.15. The network clearly outperforms individual baselines by about 1 order of magnitude or more for almost all declination angles.

The primary focus of this analysis was to obtain statistics that are based on dirty-map constructs. However, it is straightforward to extend it to be applicable to clean maps. Similarly, although we considered broadband signals, it is possible to easily extend our study to narrow band signals.

2.4.4 Map making

Finally, we compare the quality of sky maps made by the individual baselines and their network since they are among the primary products of anisotropic searches. Here, we consider two figures of merit, namely, the MLR statistic and the normalized mean square error (NMSE) for comparing maps. To compare the dirty maps, we use the MLR statistic introduced earlier, and, to compare clean maps, we use both the MLR statistic and the NMSE (defined below).

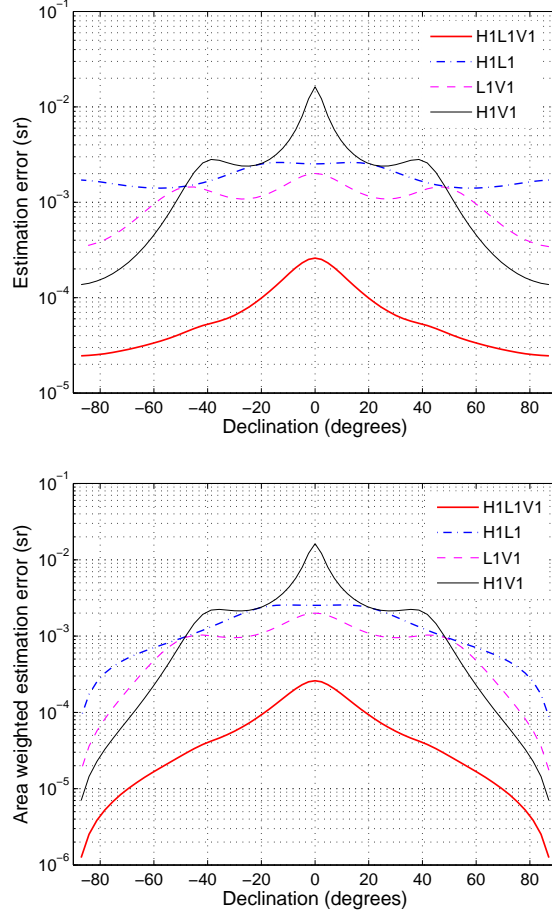


Figure 2.15: The 1σ error (top) and area-weighted 1σ error (bottom) in the solid angle for locating a source in the sky with three single baselines and the whole network. The network accuracy is better by about 1 order of magnitude or more at most of the declinations. Note that an error of $1\text{sr} \simeq 3282.81$ sq-degrees, and that the error here decreases as $1/\text{SNR}^2$.

For an unpolarized and anisotropic gravitational wave background, the maximum likelihood estimators of the signal-strength vector are given by

$$\tilde{\mathcal{P}}^k = (\mathcal{B}^{-1})^k_{k'} S^{k'}, \quad (2.46)$$

where S^k are components of the dirty map (2.17) and $\tilde{\mathcal{P}}^k$ are components of the deconvolved (clean) map. Note that the clean map, $\tilde{\mathcal{P}}$, are the values of \mathcal{P} that maximize the statistic. We extend this single-baseline analysis to a multibaseline one by simply adding the dirty maps and beam matrices as $S_{\mathcal{N}}^k = \sum_{\mathcal{I}=1}^{N_b} S_{\mathcal{I}}^k$ and $\mathcal{B}_{\mathcal{N}k'}^k = \sum_{\mathcal{I}=1}^{N_b} \mathcal{B}_{\mathcal{I}k'}^k$. So, the maximum-likelihood estimators for a multibaseline network are given by

$$\tilde{\mathcal{P}}^k = (\mathcal{B}_{\mathcal{N}}^{-1})_{k'}^k S_{\mathcal{N}}^{k'}. \quad (2.47)$$

We simulate the data with signal as [24]

$$\begin{aligned} \tilde{x}_1^*(t, f) \tilde{x}_2(t, f) &= \langle \tilde{h}_1^*(t, f) \tilde{h}_2(t, f) \rangle + \tilde{n}_1^*(t, f) \tilde{n}_2(t, f), \\ \langle \tilde{h}_1^*(t, f) \tilde{h}_2(t, f') \rangle &= \delta_{ff'} H(|f|) \sum_i \mathcal{P}^i \gamma(\hat{\Omega}_i, t, |f|), \end{aligned} \quad (2.48)$$

where \mathcal{P}^i is the injected source strength at the i^{th} pixel, and γ is the direction-dependent overlap reduction function. We use a conjugate gradient (CG) method to solve the set of linear equations (2.46) and (2.47).

The mismatch between two maps, injected and estimated, is measured using

$$\text{NMSE} := \frac{|\tilde{\mathcal{P}} - \mathcal{P}|^2}{|\mathcal{P}|^2}, \quad (2.49)$$

which is called normalized mean square error.

2.4.4.1 Dirty maps and clean maps

We performed numerical comparison of map-making performance for two types of toy sky patterns – (i) extended, multideclination sky (Fig.s 2.16 and 2.17), mimicking the (partially masked) image of the sky constructed by the WMAP satellite [45], where essentially a modified galactic structure stands out; and (ii) a relatively localized source peaked at the north pole (Fig.s 2.19 and 2.20).

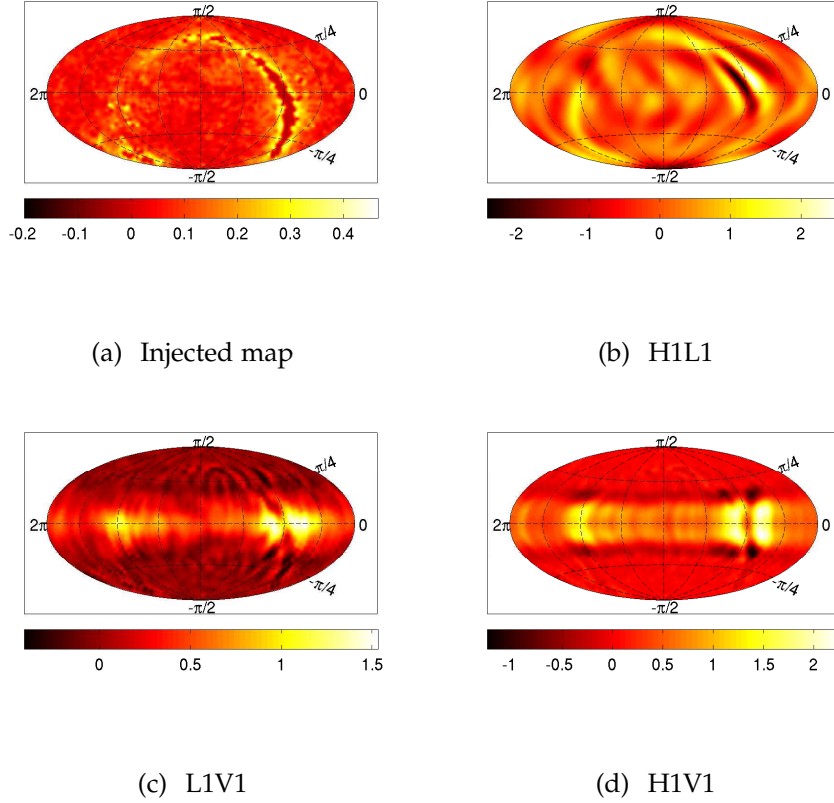


Figure 2.16: Toy model of an extended source is shown in (a). Dirty maps made from simulated data containing signal from that source are shown in the last three panels for the three LIGO-Virgo baselines.

In both cases, the dirty maps from different baselines are quite distorted compared to the injected maps. (Compare the last three plots with the first one in Fig. 2.16 and in Fig. 2.19). However, the deconvolution procedure yields reasonably resolved maps for all the baselines (Figs 2.17 and 2.20), signifying that none of the beam matrices are completely degenerate. The clean maps from the network are, however, of better quality, as can be seen from the corresponding low NMSE. To demonstrate this visually, we also show the difference between

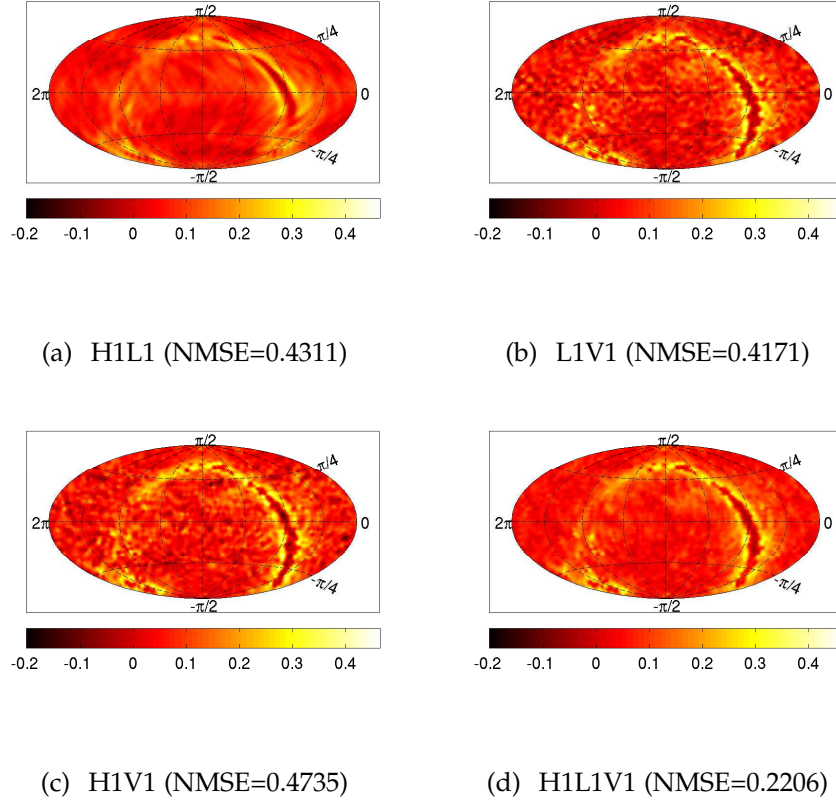
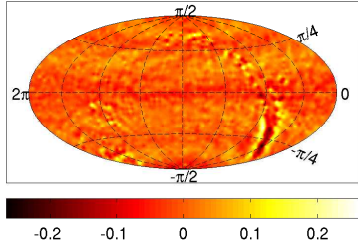


Figure 2.17: Clean maps obtained by the deconvolution of the dirty maps of Fig. 2.16, using 20 CG iterations, are shown here.

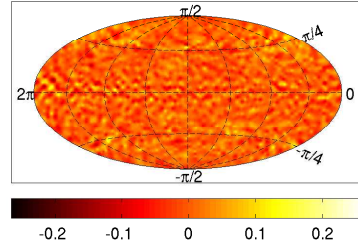
the clean and injected maps for the respective cases in Figs. 2.18 and 2.21. As expected, the difference maps for the network look less noisy and uniform across the sky than the individual baselines.

2.4.4.2 Maximized-likelihood-ratio statistic

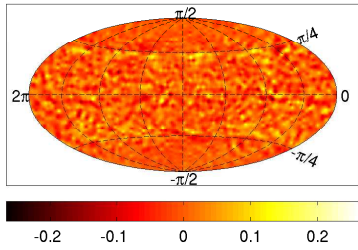
We finally compute the MLR statistic introduced in Sec. 2.3.2 as a figure of merit and, also, to demonstrate how this statistic can be powerful in identifying signal in noisy maps. The MLR statistic for both dirty and clean maps for the two types



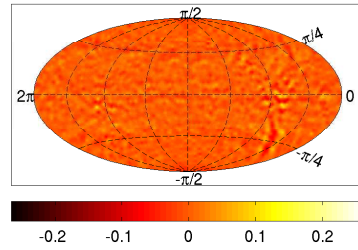
(a) H1L1



(b) L1V1



(c) H1V1



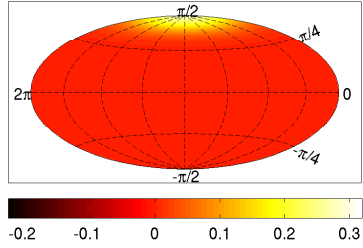
(d) H1L1V1

Figure 2.18: Difference between the clean maps of Fig. 2.17 and the injected map of Fig. 2.16(a).

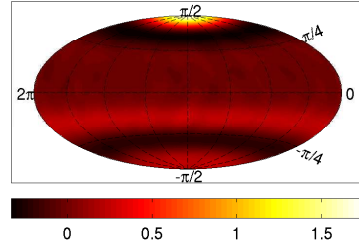
of sources considered here have been listed in Tables 2.1 and 2.2.

It is intriguing to note that, for both dirty and clean maps, one obtains similar values. This suggests that a deconvolution effected with only a few tens of conjugate-gradient basis vectors does not cause a significant amount of information loss.

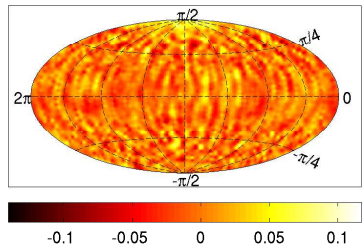
To understand the significance of the MLR statistic in the present context, we perform two more exercises. First, we study the no-injection case; that is, we make dirty maps of simulated noise (Fig. 2.22), deconvolve it (Fig. 2.23), and



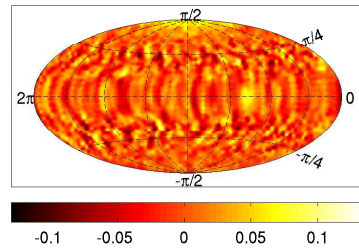
(a) Injected map



(b) H1L1



(c) L1V1

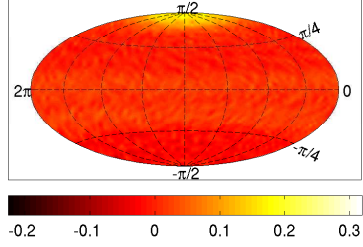


(d) H1V1

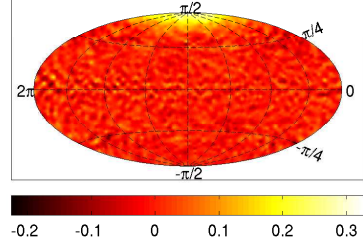
Figure 2.19: The toy model of a localized source is shown in (a). Dirty maps made from simulated data from three LIGO-Virgo baselines are shown in the last three panels.

obtain its MLR (Table 2.3). The similarity of the values of this statistic for the dirty and clean maps proves the unitarity of our deconvolution method. One can see that the MLR statistic (Table 2.3) is small (≈ 1) in all these cases. We then introduce a small signal – the same as the extended (galaxylike) source considered before, but at a much reduced strength.

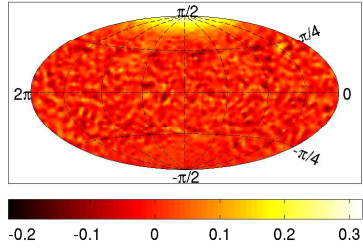
Visually, the dirty maps are now weaker (Fig. 2.24), and clean maps almost do not show the obvious presence of any source (Fig. 2.25), but the MLR statistic



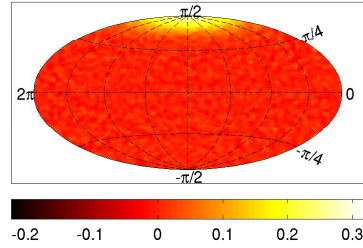
(a) H1L1 (NMSE=0.6642)



(b) L1V1 (NMSE=1.2939)



(c) H1V1 (NMSE=1.4750)



(d) H1L1V1 (NMSE=0.4961)

Figure 2.20: Clean maps obtained by the deconvolution of the dirty maps of Fig. 2.19, using 20 CG iterations, are shown here.

(Table 2.4) provides a clear and reliable indication of the presence of a signal, thus proving its usefulness in the search for signal in a noisy map.

2.5 Discussion

The search for an anisotropic stochastic gravitational wave background plays an important role in present GW research. In addition to setting interesting upper limits on astrophysical and cosmological backgrounds, the simplicity of the con-

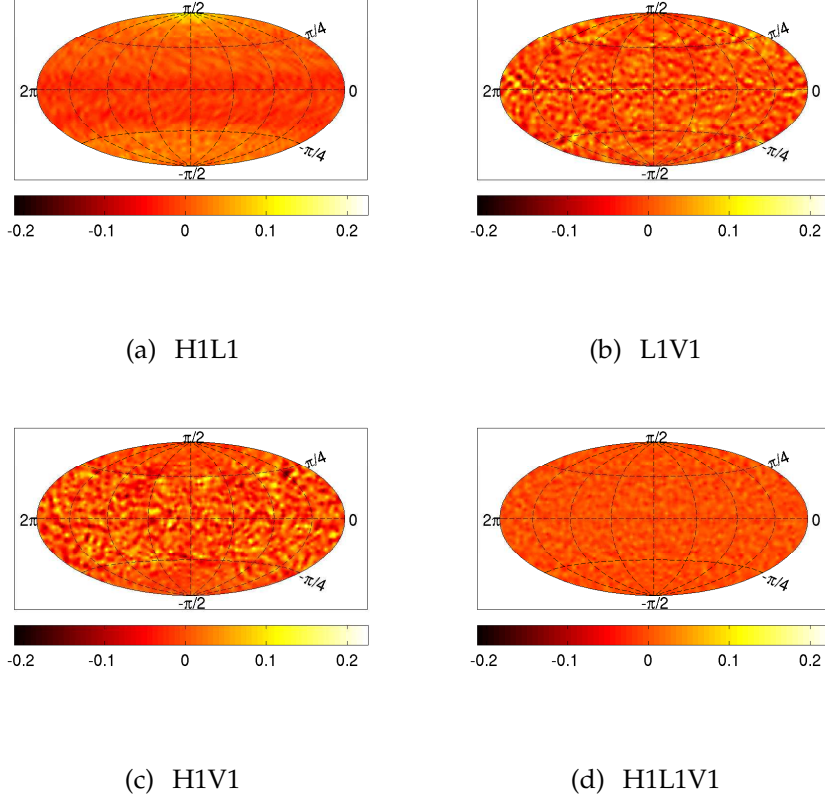


Figure 2.21: Difference between the clean maps of Fig. 2.20 and the injected map of Fig. 2.19(a).

comitant analysis reveals invaluable knowledge about the coherent performance of the GW detector network.

So far, detailed analysis strategies have been developed to search for anisotropic background in pixel and spherical harmonic spaces, and a general maximum-likelihood-based framework has been established to search in any convenient basis. The spherical harmonic search has been demonstrated using a network of detectors [14]. In this paper, for the first time, we numerically implement the directed radiometer search, including deconvolution, for a network of detec-

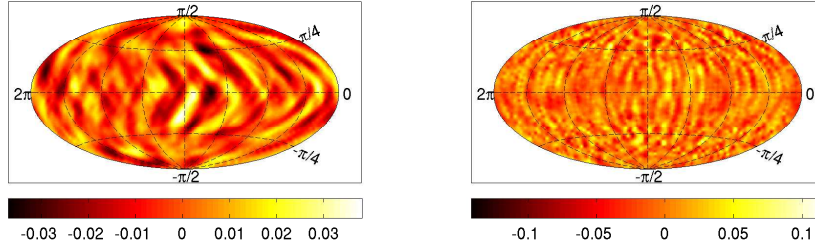
Table 2.1: MLR statistic of dirty maps (λ) versus clean maps (λ_c) for the simulated maps in Fig.s 2.16 and 2.17.

Baseline	λ	λ_c
H1L1	785.555	783.271
L1V1	359.004	358.940
H1V1	315.717	315.662
H1L1V1	919.594	917.600

Table 2.2: MLR statistic of dirty maps (λ) versus clean maps (λ_c) for the simulated maps in Fig.s 2.19 and 2.20.

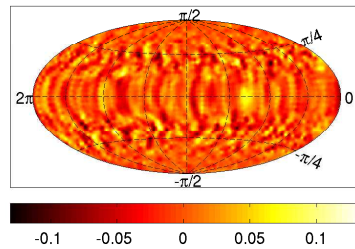
Baseline	λ	λ_c
H1L1	284.652	284.173
L1V1	39.308	39.377
H1V1	64.129	64.113
H1L1V1	294.419	293.961

tors. These methods, in the past, were focused primarily on showing that the observed map is consistent with Gaussian noise or in estimating sky maps. The latter required the inversion of the convolution equation, which itself assumed the network of detectors to be nondegenerate. Neither of these methods may work in the presence of excessive noise and weak signal. Most importantly, a statistically meaningful, all-sky combined statistic, in the form of an optimal “detection statistic,” was needed in order to make precise statements about the presence or absence of a given background model in a map. Here, we proposed



(a) H1L1

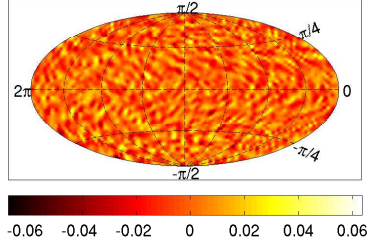
(b) L1V1



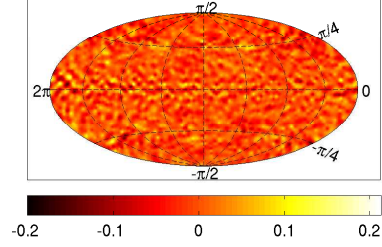
(c) H1V1

Figure 2.22: Dirty maps made for simulated noise, without any injected signals.

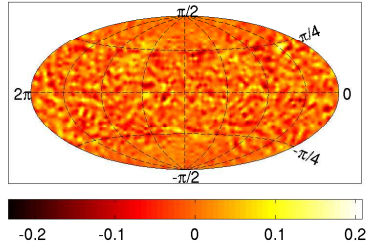
a MLR statistic, which yields a single number when computed on the dirty or the clean map and can be used as a detection statistic. By computing the MLR statistic for a couple of toy models of the background, we observe that the detection statistic is much larger than the noise-only case, even in the presence of weak signals that are barely visible in dirty or clean maps. We corroborated these statements with results obtained from extensive Monte Carlo simulations of a diffuse background of known shape in an ensemble of noise realizations. However, a more detailed study using signals from a variety of background models is surely worth pursuing in order to determine how accurate the templates need



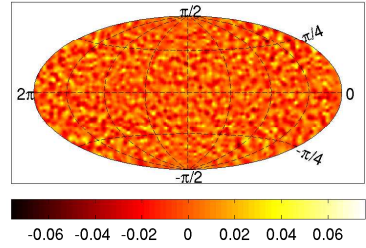
(a) H1L1



(b) L1V1



(c) H1V1



(d) H1L1V1

Figure 2.23: Clean maps obtained by the deconvolution of the dirty maps of Fig. 2.22, using 20 CG iterations.

to be in order to extract meaningful information from weak backgrounds.

We also compared the performance of individual baselines and the whole network for the directed radiometer search using different figures of merit. Evaluating the performance of a network of GW detectors in SGWB searches is relatively straightforward compared to other GW signal searches [46, 47, 48, 49, 50, 51]. This exercise was useful in drawing insights about the characteristics of a network that are particularly helpful in boosting its performance. Our overall observation, not surprisingly, is that the network improves performance in mainly

Table 2.3: MLR statistic of dirty maps (λ) versus clean maps (λ_c) for simulated noise (which actually has an extremely weak signal added) in Fig.s 2.22 and 2.23.

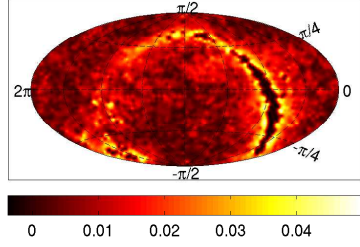
Baseline	λ	λ_c
H1L1	0.512	0.433
L1V1	-1.549	-1.542
H1V1	1.105	1.120
H1L1V1	0.208	0.149

Table 2.4: MLR statistic of dirty maps (λ) versus clean maps (λ_c) for the simulated maps in Fig.s 2.24 and 2.25.

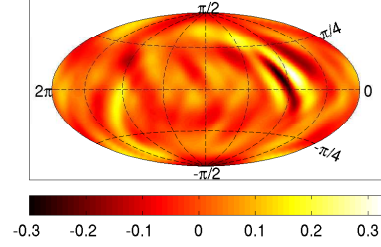
Baseline	λ	λ_c
H1L1	98.643	98.670
L1V1	43.520	43.536
H1V1	40.432	40.475
H1L1V1	115.132	115.176

three ways, namely, (1) by increasing the sensitivity by observing each direction a greater number of times, (2) by observing the sky more uniformly, and (3) by probing each direction on the sky with additional detectors on the globe. The latter two enhancements lead to better localization of pointlike sources. This can be understood via the behavior of the Fisher information matrix: More detectors reduce its degeneracy and improve the well-posedness of the inverse problem. This, in turn, leads to a more accurate production of clean maps.

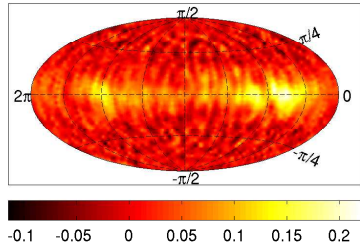
Another question worth addressing in the future is about how closely spaced



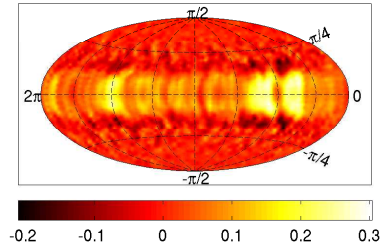
(a) Injected map



(b) H1L1



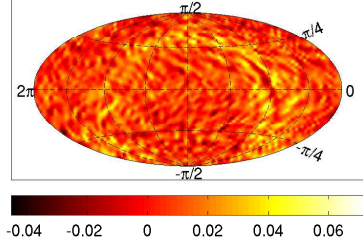
(c) L1V1



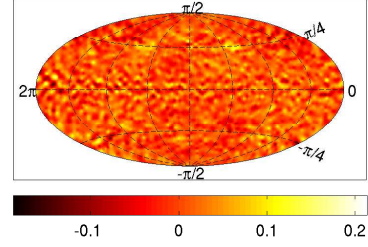
(d) H1V1

Figure 2.24: The toy model of a very weak extended source is shown in (a). Dirty maps made from simulated data from three LIGO-Virgo baselines are shown in the last three panels.

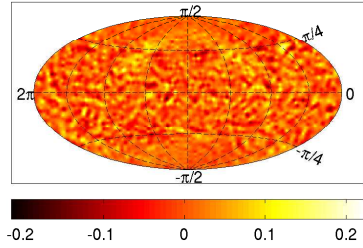
must the templates be on the parameter space to maximize the chances of detection with available computational resources. Indeed, the proposal for templated searches for SGWB signals is not new to this paper. For example, it has been addressed earlier in the context of isotropic searches (see Ref. [53] and the references therein). Ref. [53] also introduced a metric on the parameter space of those signals so as to enable an experimenter to infer what the principle axes are on that space and how fine a template bank one can afford based on the com-



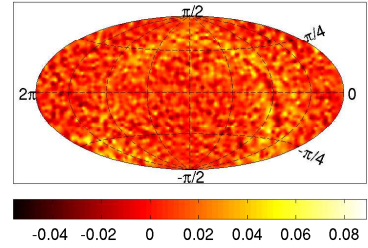
(a) H1L1 (NMSE=1.0694)



(b) L1V1 (NMSE=3.3557)



(c) H1V1 (NMSE=3.8406)



(d) H1L1V1 (NMSE=1.3503)

Figure 2.25: Clean maps obtained by the deconvolution of the dirty maps of Fig. 2.24, using 20 CG iterations.

putational resources available. A similar study can be carried out for finding a more optimal spacing of templates for directed searches than the one used here.

Whereas results presented here were derived for Gaussian noise, the codes used can be applied to real data as well. Indeed, the performance of the proposed statistic in real data sets from the LIGO and Virgo detectors can be determined through hardware injections that were done in the recent science runs, such as the ones described in Ref. [54], and supplementing them with multiple software injections to improve the statistics. The expected improvement

of network sensitivity over individual baselines, as demonstrated here, merits the investment required for extending the current single-baseline analysis efforts [24, 25] to a multibaseline one. This conclusion is strengthened by the fact that adding a detector to a baseline can potentially mitigate the contribution of cross correlated environmental noise that affects only one of the three resulting baselines. Including V1, which is on a different continental plate than the H1L1 baseline, can serve this purpose. Employing a null-stream statistic [52, 51] to complement the detection statistic might also help in discriminating against such noise.

Chapter 3

Searching for a SGWB from the population of neutron stars in the Virgo cluster

One of the promising applications of the methods presented in the previous chapter is to search for a stochastic background from the population of rotating non-axisymmetric neutron stars (NSs) in the Virgo cluster. The Virgo cluster is the nearest and best-studied rich cluster of galaxies whose center is at a distance of about 16.5 Mpc away in the constellation Virgo. At present, more than 1300 member galaxies of the Virgo cluster are known. Estimates suggest that there are approximately 10^{11} neutron stars in the Virgo cluster [55], of which a small fraction would emit GWs with frequencies within the sensitivity band of earth-based detectors. As such, it offers the best hope to detect a SGWB produced by the population of the neutron stars in the Virgo cluster, if such a background

exists and is reachable by the current and advanced detectors.

A recent study [55] suggests that the stochastic nature of gravitational waves from the population of rotating non-axisymmetric neutron stars/pulsars in the Virgo cluster can reveal itself as a GW hot spot in our searches. We begin this chapter by reviewing a series of assumptions made in this reference. We then detail the steps that are taken towards a meaningful model-based search for SGWB from NSs in the Virgo cluster.

3.1 Motivation for the directed search

The GW strain due to a rotating neutron star can be expressed as [56]

$$h = 4\pi^2 \alpha \frac{G\epsilon I}{c^4 r} f^2, \quad (3.1)$$

where $\alpha(\leq 1)$ is the orientation factor, ϵ is the (equatorial) ellipticity of the neutron star, I its principal moment of inertia, r is the distance to the source, G the Newton's gravitational constant, c the speed of light, and f is the GW frequency. If the rotation axis is optimally oriented with respect to the detector, then α becomes unity.

The total number of Galactic neutron stars is estimated to be about $10^8 - 10^9$ [57]. This is obtained by assuming the mean neutron star birth rate of 10^{-2} yr^{-1} and the Galactic age of about 10 Gyr. What is more uncertain for the study reported in Ref. [55] is the number of neutron stars whose rotation period is of the order of milliseconds. From the survey of radio pulsars in our Galactic disk, the population of millisecond pulsars is estimated to be at least 40000 [58]. This implies a mean birth rate of $4 \times 10^{-6} \text{ yr}^{-1}$. To date, roughly 2000 NSs have been

observed, not all of which are millisecond pulsars and the majority of which are identified as isolated radio pulsars (PSRs) with ages $\lesssim 100$ Myr.

In Fig. 3.1, we show the distribution of observed radio pulsars. This distribution indicates two different populations: Each population is Gaussian distributed and has mean and standard deviation different from the other's. Hence, the distribution is approximated as a bimodal Gaussian with the components as follows:

$$P_1(\log f_r)d(\log f_r) = \frac{1}{\sqrt{2\pi}\sigma_1} e^{-((\log f_r - \log \mu_1)^2 / 2\sigma_1^2)} d(\log f_r), \quad (3.2)$$

(for $f_r > 50\text{Hz}$),

$$P_2(\log f_r)d(\log f_r) = \frac{1}{\sqrt{2\pi}\sigma_2} e^{-((\log f_r - \log \mu_2)^2 / 2\sigma_2^2)} d(\log f_r), \quad (3.3)$$

(for $f_r < 50\text{Hz}$),

where $\mu_1 = 219$ Hz, $\sigma_1 = 0.238$, $\mu_2 = 1.71$ Hz and $\sigma_2 = 0.42$, and $f_r = f/2$. Here, P_1 and P_2 are normalized to unity when integrated from $f_r = 0$ to infinity. We assume a similar bimodal form of distribution of NSs in the Virgo cluster. We assume that the total number of neutron stars in our Galaxy is 10^8 for $f_r < 50$ Hz, and 40000 for $f_r > 50$ Hz. Since there are of the order of 10^3 galaxies in the Virgo cluster, the total number of NSs in the Virgo cluster is $N_{\text{low}} \sim 10^{11}$ for $f_r < 50$ Hz, $N_{\text{high}} \sim 4 \times 10^7$ for $f_r > 50$ Hz. So, the distribution of NSs in the Virgo cluster can be expressed as

$$N(f)df = \left(N_{\text{high}} P_1(\log f_r) + N_{\text{low}} P_2(\log f_r) \right) \frac{df_r}{f_r \ln 10}. \quad (3.4)$$

For a bandwidth of $\sim 10^3$ Hz, the number of NSs in each mHz frequency bin is ~ 10 for $f > 100$ Hz. In the low frequency regime this number is much larger.

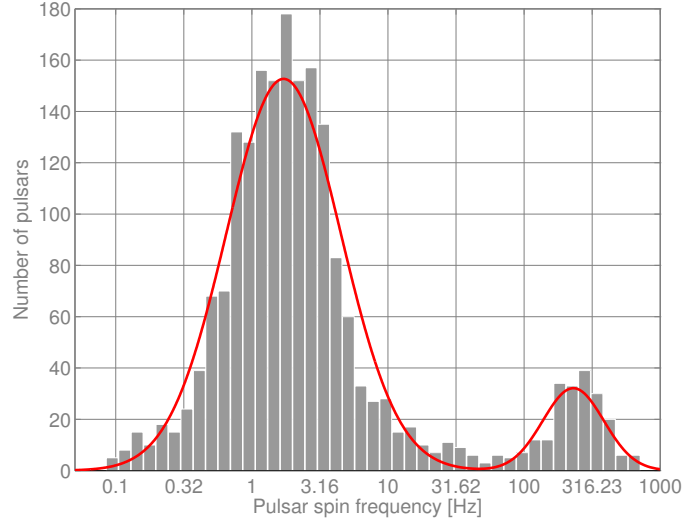


Figure 3.1: The distribution of observed radio pulsars [59]. The horizontal axis is $\log(f_r)$ where f_r is the rotational frequency of pulsars. The red solid line is the two component Gaussian-fit to the distribution [55].

Thus, it is not possible to resolve the signal from each NS and, therefore, the GW signal from the NS population in the Virgo cluster is expected to be stochastic in nature.

The spectral density of gravitational radiation from NSs in the Virgo cluster is given by

$$H(f) = \langle h^2 \rangle N(f), \quad (3.5)$$

$$= \left[7.05 \times 10^{-34} \left(\frac{\epsilon}{10^{-5}} \right) \left(\frac{I}{1.1 \times 10^{45} \text{g cm}^2} \right) \right]^2 \langle \alpha^2 \rangle f^4 N(f), \quad (3.6)$$

where the unit of $H(f)$ is Hz^{-1} , $\langle \alpha^2 \rangle$ represents the average of the orientation factor with respect to the inclination and polarization angles. Here, we used $r = 16.5$ Mpc, the distance to the Virgo cluster. Assuming a uniform distribution of the sources over those angles, we have $\langle \alpha^2 \rangle = 0.4$. Figure 3.2 shows the

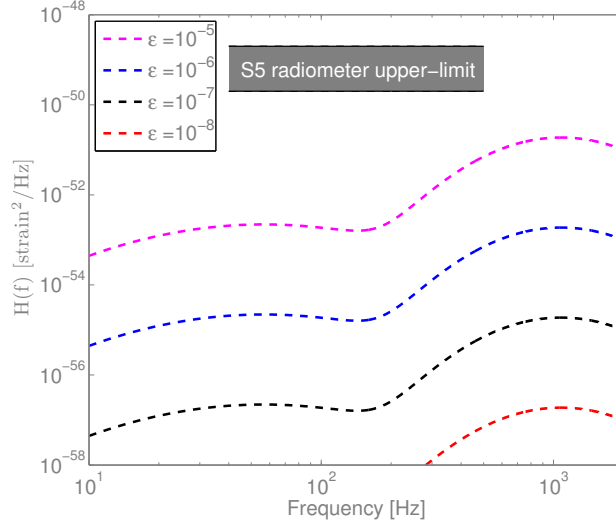


Figure 3.2: The spectral density of gravitational radiation from NSs in the Virgo cluster is plotted as a function of GW frequency for different choices of average ellipticity, $\epsilon \in \{10^{-5}, 10^{-6}, 10^{-7}, 10^{-8}\}$. The shaded area labeled “S5 radiometer upper-limit” illustrates the radiometer upper-limit of GW strain power using S5 LIGO data [60].

spectral density as a function of GW frequency for different choices of average ellipticity.

In order to obtain a rough idea of how large the $H(f)$ is compared with the noise PSD, a figure of merit “effective source spectral density”, $H_{\text{eff}}(f)$, is defined

$$H_{\text{eff}}(f) = \sqrt{8 T_{\text{obs}} \langle \Gamma^2 \rangle_{1\text{day}} f} H(f), \quad (3.7)$$

such that the signal-to-noise ratio can be expressed as

$$\rho = \sqrt{\int_{f_l}^{f_u} \frac{df}{f} \frac{H_{\text{eff}}^2(f)}{\xi_{(1)}(f)\xi_{(2)}(f)}}, \quad (3.8)$$

where T_{obs} is the observation time and $\langle \Gamma^2 \rangle_{1\text{day}}$ is the average of the square of Γ (see Eq. (2.23)) over a sidereal day. The noise amplitude spectral densities (ASDs) of various detectors as well as the effective source ASD are plotted in Fig. 3.3. Here, we assume $T_{\text{obs}} = 1 \text{ yr}$ and $\sqrt{\langle \Gamma^2 \rangle_{1\text{day}}} = 0.2$.

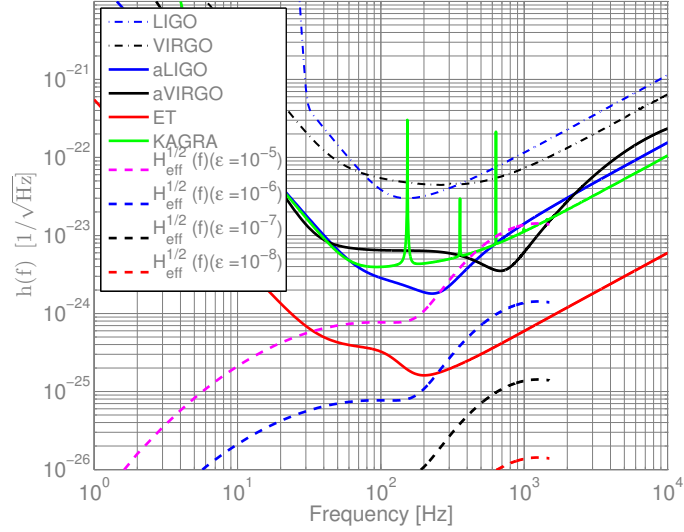


Figure 3.3: The noise amplitude spectral densities of various first, second and third generation detectors, as well as the effective source ASD, $\sqrt{H_{\text{eff}}}$, are plotted here. In this plot, $T_{\text{obs}} = 1 \text{ yr}$ and $\langle \Gamma^2 \rangle_{1\text{day}} = 0.04$. This figure is reproduced from Ref. [55].

The analysis results shown here strongly depend on the value of average ellipticity of the NSs. If $\epsilon \leq 10^{-6}$, it will be difficult to observe stochastic GW profiles of the NSs in the Virgo cluster with aLIGO, aVIRGO, and KAGRA detectors. Only when detectors have ET like sensitivity will it be possible to detect such a signal for average $\epsilon = 10^{-6}$. The detectability improves if we employ several baselines of a network of detectors and a longer observation time [13].

3.2 Modeling the neutron stars in the Virgo cluster

Radio pulsars are highly magnetized, rapidly spinning neutron stars which emit beams of radio waves. The wave is observed only when the beam crosses the line of sight. It is important to note that the observed distribution of the period of radio pulsars is not necessarily the true representation of the entire population [61]. This is because various selection effects cause the number of detected pulsars to be much smaller. For example, we can not observe the pulsars whose radio beams do not cross the earth or whose radio emission is too weak to be detected. The aperture of the emission cone decreases with the period as well as the luminosity.

The optimal way of searching for stochastic GW profiles from the neutron stars in the Virgo cluster is to cross-correlate the data from the detectors, taken in pairs, with a sky-position dependent time-frequency filter. To do that we need to assume what the spectral shape is of the targeted source. If the true spectrum does not match with the modeled spectrum, the statistic becomes sub-optimal. However, the source spectrum derived in Eq. (3.6) is severely affected by the radio selection effects. To model such a spectrum a set of corrections needs to be applied to the known pulsar sample [62]. Here we propose to simulate the expected spin frequency distribution assuming a power law, and then analyze the data with a few different spectral index choices. If no detection is made, we will present the upper limits on the average ellipticity of neutron stars in the Virgo cluster as a function of the spectral index. In the following sections, we justify three spectral index choices for the search.

There are several mechanisms by which neutron stars generate gravitational waves. These include free precession, spinning non-axisymmetric deformation, and unstable oscillation. Free precession occurs if a neutron star's rotation axis is misaligned with respect to its symmetry axis. There are a number of mechanisms that may lead to a neutron star being deformed away from axisymmetry. The non-axisymmetric rotating neutron stars are the most promising sources for continuous GWs. Unstable oscillation modes in the fluid part of a neutron star can occur during the birth of the star, close encounter with another star or an accretion phase.

3.2.1 The gravitar model

We consider a population of non-axisymmetric rotating neutron stars having negligible magnetic field so that the dominant energy loss, due to a deviation from axisymmetry, goes into the production of gravitational waves. These objects are often called “gravitars” [63, 64, 65]. There might exist such a population, which is electromagnetically invisible. Detecting its GW profile with ground-based GW detectors is an interesting prospect. Even if gravitars do not exist, they provide a relevant upper bound on the GW emission by objects that do exist, such as rapidly-rotating NSs. The GW spin-down due to a gravitar's non-axisymmetric shape is given by

$$\dot{f} = -\frac{32\pi^4}{5} \frac{GI}{c^5} \epsilon^2 f^5, \quad (3.9)$$

where $\epsilon = \frac{I_1 - I_2}{I}$ is the ellipticity of the gravitar, with I_1 , I_2 and I being the moment of inertia with respect to the three principal axes. Note that the gravitational-

wave frequency is twice the NS's spin frequency. Integrating Eq. (3.9) gives the GW frequency at time t as

$$f(t) = \left(f_0^{-4} + \beta^{-1} \epsilon^2 t \right)^{-1/4}, \quad (3.10)$$

where f_0 is the initial (birth) GW frequency and

$$\beta = \frac{5}{128\pi^4} \frac{c^5}{GI}. \quad (3.11)$$

The constant β approximates to

$$\beta^{1/3} = 5.3 \left(\frac{10^{38} \text{ kg m}^2}{I} \right)^{1/3} \text{ kHz}. \quad (3.12)$$

The frequency evolution of gravitars is determined by the distribution of spin frequencies at birth, ellipticity, and the age since birth.

We considered a model motivated from the observed pulsars for the distribution of the initial spin frequencies. It is the one found as the maximum likelihood model by population synthesis [66, 63]. It is described by a standard log-normal distribution

$$P_{f_0}(f_0) df_0 = \frac{1}{\sqrt{2\pi}\sigma f_0} \exp \left[-\frac{1}{2\sigma^2} (\ln(f_0) - \ln(\bar{f}_0))^2 \right] df_0, \quad (3.13)$$

where the unit of f_0 is Hz and the values $\sigma = 0.69$ and $\bar{f}_0 = 400$ Hz are taken from the Ref. [66]. Gravitars with $f_0 > 4$ kHz are excluded from the simulation.

The value of the ellipticity depends on the neutron star properties. The typical ellipticity of neutron stars is unknown, and the possible maximum value is very uncertain. At present, the values $10^{-9} < \epsilon < 10^{-6}$ are considered plausible. Following [63], we use a probability distribution which satisfies the principle of maximum entropy and is given by

$$P_\epsilon(\epsilon) = a(\tau) e^{-\epsilon/\tau}, \quad (3.14)$$

where

$$a(\tau) = \frac{1}{\tau(1 - e^{-\epsilon_{\max}/\tau})}, \quad (3.15)$$

with ϵ_{\max} being the maximum possible value for ϵ . The relation between the parameter τ and the mean value of the distribution, $\bar{\epsilon}$, is given by

$$\tau = \bar{\epsilon} + \frac{\epsilon_{\max}}{\exp(\epsilon_{\max}/\tau) - 1}. \quad (3.16)$$

It is straightforward to derive an evolved distribution in frequency, given an initial distribution of frequency, birth rate and ellipticity [65]. We define the conditional frequency distribution $p_f(f|\epsilon, t)$ at time t such that

$$dP_f = p_f(f|\epsilon, t) df \quad (3.17)$$

is the probability of finding a gravitar in the frequency range f to $f + df$, assuming an ellipticity ϵ and an age t . Let dP_{f_0} be the probability of the birth frequency in the frequency range f_0 to $f_0 + df_0$. The corresponding probability density $p_{f_0}(f_0)$ is defined by

$$dP_{f_0} = p_{f_0}(f_0) df_0. \quad (3.18)$$

A frequency change by redshift is neglected since all the gravitars considered here are within the local universe (a few Mpc). To compute $p_f(f|\epsilon, t)$ from the initial $p_{f_0}(f_0)$, consider a single gravitar with ellipticity ϵ whose current frequency is f , and let $f_0(\epsilon, f, t)$ denote the gravitar's frequency at time t in the past. Solving Eq. (3.10) for the birth frequency yields

$$f_0(f, \epsilon, t) = \left(f^{-4} - \beta^{-1} \epsilon^2 t \right)^{-1/4}. \quad (3.19)$$

The fraction of gravitars at birth in the frequency range f_0 to $f_0 + df_0$ is the same as the fraction at present in the frequency range f to $f + df$, so the intensity $p_f df = p_{f_0} df_0$ yields

$$p_f(f|\epsilon, t) df = p_{f_0}(f_0(f, \epsilon, t)) \frac{\partial f_0(f, \epsilon, t)}{\partial f} df, \quad (3.20)$$

$$= p_{f_0}(f_0(f, \epsilon, t)) \frac{f_0^5(f, \epsilon, t)}{f^5} df. \quad (3.21)$$

The probability dP of finding a gravitar in a volume characterized by $df d\epsilon dt$ is

$$dP = p_f(f|\epsilon, t) p_t(t) p_\epsilon(\epsilon) df d\epsilon dt, \quad (3.22)$$

where $p_t(t)$ and $p_\epsilon(\epsilon)$ are the probability distributions for the time and ellipticity, respectively. Note that the distributions of the initial frequency, time and ellipticity are assumed to be normalized, such that $\int_0^\infty p_x(x) dx = 1$. Then the evolved frequency distribution is obtained by marginalizing dP over t and ϵ as

$$p_f^{\text{ev}}(f) df = \int_0^T dt \int_0^\infty d\epsilon p_f(f|\epsilon, t) p_t(t) p_\epsilon(\epsilon) df. \quad (3.23)$$

Some of these expressions, between Eqs. 3.14 and 3.23, are re-derived from Benjamin Knispel's Ph.D. thesis [65]. For a fixed age of all sources, which is obtained by marginalizing Eq. (3.22) over ellipticity only, the evolved frequency distribution can be expressed as

$$p_f^{\text{ev}}(f|t) df = \int_0^\infty d\epsilon p_f(f|\epsilon, t) p_\epsilon(\epsilon) df, \quad (3.24)$$

$$= \frac{a(\tau)}{1.73 f^5} \int_0^\infty \frac{e^{-1.05(-\frac{1}{4}\ln(f^{-4}-\beta^{-1}\epsilon^2t)-5.992)^2}}{f^{-4}-\beta^{-1}\epsilon^2t} e^{-\epsilon/\tau} d\epsilon \quad (3.25)$$

$$= \frac{a(\tau) \tau}{1.73 f} e^{-1.05(\ln(f)-5.992)^2}, \quad (3.26)$$

where the last expression is obtained by setting $t = 0$ Myr.

3.2.2 A population synthesis model of millisecond pulsars

The population of the millisecond pulsars (MSPs) was the primary focus of the study reported in Sec. 3.1. Since MSPs are observed to spin down relatively slowly, it is unrealistic to consider high ellipticity ($\epsilon \approx 10^{-5}$) for such a population. Figure 3.4 shows the distribution of observed MSPs and it certainly does not represent the entire population since only a small fraction of the estimated Galactic MSPs are observed. Also, the Virgo cluster is an elliptical rich cluster. These facts should be taken into consideration when deriving the estimated number of MSPs in the Virgo cluster. To take these into account, we begin with a population synthesis of radio pulsars in the Galactic disk [67, 68].

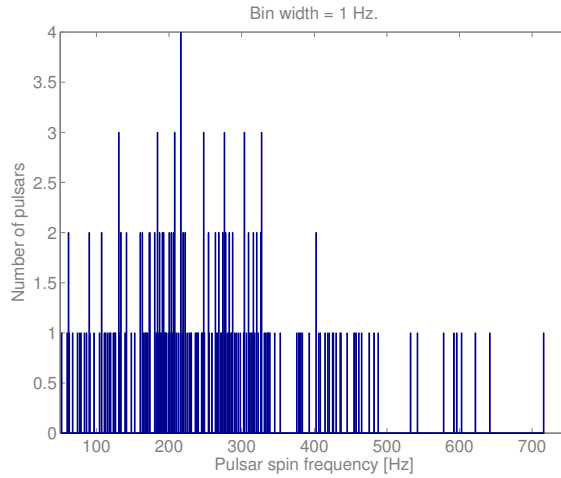


Figure 3.4: The distribution of observed millisecond pulsars [59]. The frequency bin width considered here is 1 Hz.

In a recent study, S. A. Story *et al.* used a population synthesis to investigate the initial properties of MSP [67]. This study does not account for the population of MSP observed in globular clusters. The spatial distribution of millisecond

pulsars is modeled by assuming their birth in the Galactic disk with a random kick velocity and by evolving them to the present within the Galactic potential.

Following [67], we derive the distribution of the actual period, by evolving a set of simulated MSPs from the end of the spin-up phase to present ¹. For each pulsar, we proceed as follows:

- We assume a uniform birth rate distributed between 0 and 12 Gyr.
- The initial magnetic field B_0 is drawn from a uniform distribution in the range from 10^8 to 10^{12} Gauss. In this model, there is no dissipation of the magnetic field.
- The initial period is derived from the formula

$$P_0 = 0.18 \times 10^{3\delta/7} B_0^{6/7}, \quad (3.27)$$

where P_0 is in ms and B_0 is in units of 10^8 G. The dithering parameter δ varies from 0 to 2.8.

- Finally, having the initial period, magnetic field and age, we calculate the actual period from the usual dipole formula [71]:

$$P(t) = \sqrt{P_0^2 + 0.154 B_0^2 t}, \quad (3.28)$$

where P and P_0 are in ms, B_0 in units of 10^8 G, and t in Gyr.

The Monte Carlo simulations for 10000 MSPs with $P < 50$ ms are done by Tania Regimbau [72]. One could improve the model considered here by allowing

¹Similar studies for normal pulsars can be found in Refs. [69, 70].

magnetic field decay and simulating them in an elliptical rich galaxy. However, if we account that one third of the total luminosity of the Virgo cluster comes from spiral type galaxies and two third from ellipticals, then the total number of MSPs in the Virgo cluster is about 275 times larger than that in the Milky Way [73].

3.2.3 A simple power-law

Here we consider a crude approximation that there are equal numbers of NSs in every frequency bin, i.e, $N(f) = \text{constant}$.

In Fig. 3.5, we show different SGWB spectra calculated using the models described above. For comparison, the SGWB spectrum obtained from observed radio pulsars (without correcting for radio selection effects) is also plotted here. Note that the quantity $\bar{H}(f)$ is defined such that $\bar{H}(f) = H(f)/H(f = 100)$. For the gravitar model we assumed the average ellipticity to be $\bar{\epsilon} = 10^{-7}$, maximum ellipticity $\epsilon_{\text{max}} = 2.5 \times 10^{-6}$, and an age in the range $[0, 10]$ Myr. Spectra with different ages in the range $[0, 10]$ Myr are not much different. This is because we assume a small average ellipticity for the gravitars. It is interesting to note that these model-based spectra are not much different from each other. But each of these three spectra is different from the spectrum of the observed population.

3.3 The directed SGWB search and Olbers' paradox

Following Olbers' paradox, for a putative SGWB from NSs in the Virgo cluster, one may not need to invoke a directional search. An all-sky search should be

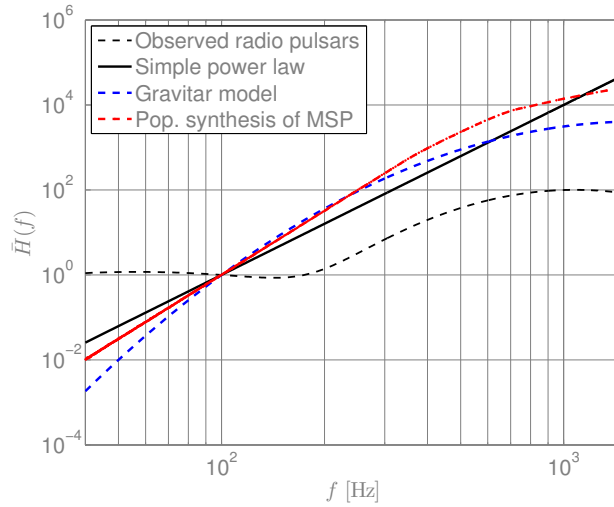


Figure 3.5: Several model-dependent spectral profiles of SGWB from NSs in the Virgo cluster. Note that $\tilde{H}(f) = H(f)/H(f = 100 \text{ Hz})$.

enough to add up coherent cross-power from all such sources thought the universe, out to a redshift beyond which stars were not yet forming. To address this concern, let us begin by stating the Olbers' paradox: Light from the stars should make the sky as bright as the sun in all directions. The darkness of the night sky conflicts with the assumption of an infinite and static universe. In other words, the number of stars per unit solid angle increases with distance-squared. Whereas, their intensity at the earth decreases as inverse distance-squared. This means that the intensity per unit area per unit solid angle should be the same in every direction.

There are many solutions to this paradox depending on the models about the universe's structure and/or its evolution. For our case, the solution to Olbers' paradox becomes obvious when we include the expansion of the universe. The

gravitational waves themselves are redshifted, which introduces the additional decrease in flux and makes the distant universe darker. One can compare the relative strengths of an anisotropic SGWB and the isotropic SGWB created respectively by the local and distant universe. By counting the number of Galaxies per unit solid angle per unit distance, one finds that the population in the direction to the Virgo cluster is roughly 8 times denser than that from all-sky up to 4 Gpc [74]. However, a better study considering the expansion of the universe is done in Ref. [75]. For a universe which is currently dust dominated, it is found that the Virgo cluster is about 50 times brighter than the background created by the distant sources (see Appendix C.1 for details). Hence, it makes sense to do a directed search for GW from the Virgo cluster.

3.4 Setting up the analysis

The choice of basis for an analysis, in principle, should not affect the physical search results. However, in practice, such a choice can bear on computational costs of a search and also on the systematic errors affecting observational results. For these reasons, we expect that while searching for GW from a point source, pixel basis is the natural choice. Whereas searching for a diffuse background, a spherical harmonic basis is a better choice.

3.4.1 Methodology

Since the angular extension of the Virgo cluster is about 8 degrees, we carry out the data analysis using a spherical harmonic (SpH) basis [14]. An extended

source with an arbitrary angular distribution can be characterized by spherical-harmonic coefficients \mathcal{P}_{lm} such that

$$\mathcal{P}(\hat{\Omega}) = \sum_{lm} \mathcal{P}_{lm} Y_{lm}(\hat{\Omega}), \quad (3.29)$$

which is consistent with Eq. (2.34). The series is truncated at $l = l_{\max}$, allowing for angular scale $\sim 2\pi/l_{\max}$. In SpH basis, the MLR statistic introduced in Eq. (2.20) can be written as

$$\lambda = \frac{\mathcal{P}^{\mu\dagger} X_{\mu}}{\sqrt{\mathcal{P}^{\nu\dagger} \Gamma_{\nu\tau} \mathcal{P}^{\tau}}}, \quad (3.30)$$

where $\mu \equiv \{l, m\}$, X_{ν} is the dirty map, and $\Gamma_{\mu\nu}$ is the beam matrix or Fisher matrix and are given by [14]

$$X_{\nu} = \sum_{ft} \gamma_{\nu}^*(f, t) \frac{H(f)}{\xi_{(1)}(f, t) \xi_{(2)}(f, t)} C(f, t), \quad (3.31)$$

$$\Gamma_{\mu\nu} = \sum_{ft} \gamma_{\mu}^*(f, t) \frac{H^2(f)}{\xi_{(1)}(f, t) \xi_{(2)}(f, t)} \gamma_{\nu}(f, t), \quad (3.32)$$

where $\gamma_{\mu}(f, t)$ is the angular decomposition of the overlap reduction function $\gamma(\hat{\Omega}, f, t)$, which characterizes the orientation and frequency response of the detectors:

$$\gamma_{lm}(f, t) \equiv \int_{S^2} d\hat{\Omega} \gamma(\hat{\Omega}, f, t) Y_{lm}(\hat{\Omega}), \quad (3.33)$$

$$\gamma(\hat{\Omega}, f, t) = \frac{1}{2} F_1^A(\hat{\Omega}, t) F_{2,A}(\hat{\Omega}, t) e^{2\pi i f \hat{\Omega} \cdot \Delta \mathbf{r}(t)/c}, \quad (3.34)$$

and $C(f, t) = \frac{2}{\Delta t} \tilde{x}_1^*(f, t) \tilde{x}_2(f, t)$ is the cross spectral density generated for each interferometer pair.

3.4.2 Angular extension of the Virgo cluster

We model the signal-strength vector of the Virgo cluster such that its non-zero components follow a Gaussian distribution, centered at 12h 26m 32s RA and $+12^\circ 43' 24''$ Dec, extended over 12h–13h RA and $5^\circ - 20^\circ$ Dec. Figure 3.6 shows the map of the signal-strength vector $\mathcal{P} \equiv \mathcal{P}_{\text{model}}$. The spherical-harmonic coefficients \mathcal{P}_{lm} are set to zero for $l > (l_{\text{max}} = 30)$ as shown in Fig. 3.7. This corresponds to an angular scale about 12 degrees.

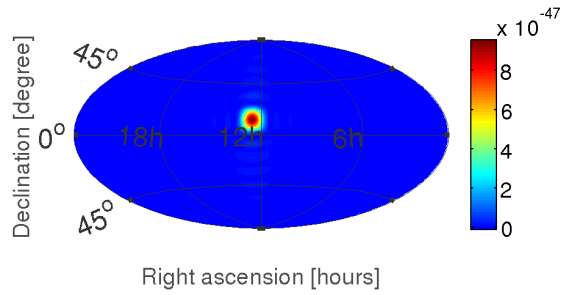


Figure 3.6: The map of a modeled signal-strength vector of the Virgo cluster. In this map, the spherical harmonic coefficients are set to zero for $l > (l_{\text{max}} = 30)$.

3.4.3 The analysis pipeline

We analyze data from LIGO's 4 and 2 km detectors (H1, H2 & L1, excluding H1-H2 pair) and VIRGO's 3 km detector during their S5 and S6 and VSR1, VSR2, and VSR3 science runs. The HLV network lifetime is about 3.2 years. The search bandwidth considered here is 40-1500 Hz. We parse the time series into 60 second intervals, Hann-windowed, 50%-overlapping segments, coarse-grained

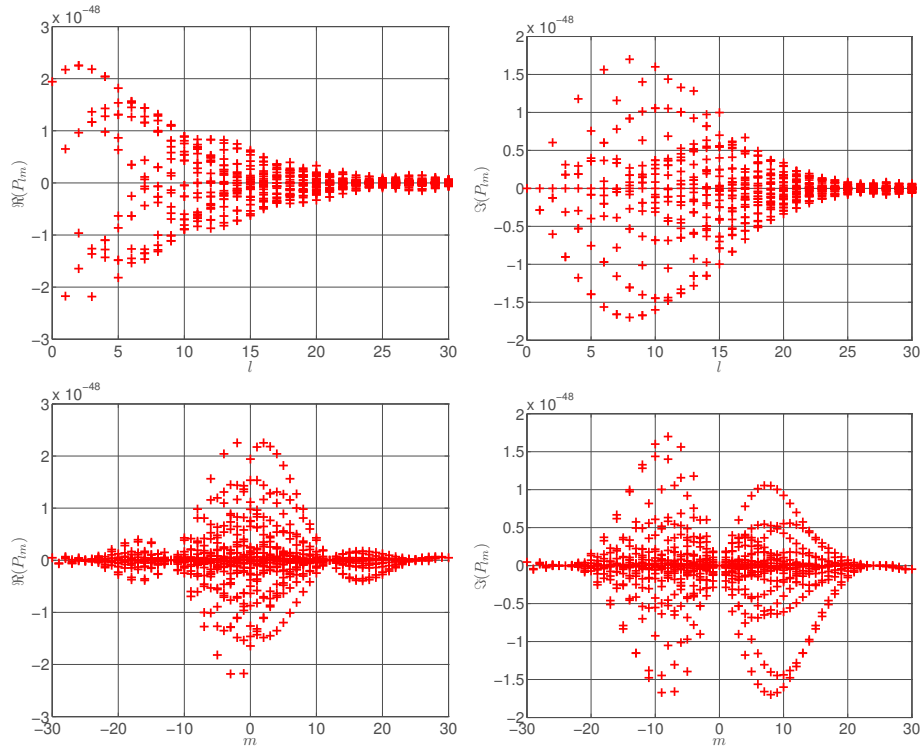


Figure 3.7: The spherical harmonic coefficients of the modeled signal-strength vector in Fig. 3.6. In the top panel, the real (left) and imaginary (right) parts of \mathcal{P}_{lm} are plotted for different m as a function of l . Whereas in the bottom panel, the real (left) and imaginary (right) parts of \mathcal{P}_{lm} are plotted for different l as a function of m .

to achieve 0.25 Hz resolution. We also mask frequency bins associated with instrumental lines. The cross-correlation analysis is performed on each segment. The results from the segments are then combined into the final result. Figure 3.8 shows a schematic of the stochastic search pipeline used for this search. For each baseline, given a model \mathcal{P} , the MLR statistic is computed based on the dirty map and beam matrix. The MLR statistics from the different baselines are then

combined to find a network MLR statistic. The whole process is repeated but with time-shifted data to estimate the background. The results are collected at the end and post-processed if needed. Note that the upper stream of the pipeline is common to both all-sky and directed searches. This pipeline has been tested with hardware and software injections, and reviewed on many occasions.

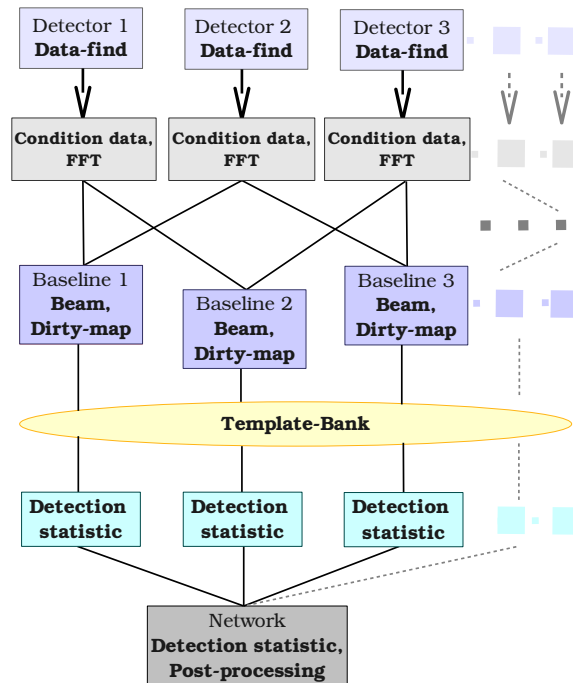


Figure 3.8: A schematic diagram of the stochastic search pipeline.

3.4.4 Simulations

It is simple, using the spherical harmonics basis, to specify a resolution cutoff by only allowing $l \leq l_{\max}$. This avoids oversampling and reduces the number of

required basis vectors. Also, since extending this cutoff to a larger l_{\max} does not affect the original basis vectors, it is straightforward to run the analysis with a higher resolution, and later follow up at a lower resolution. The computationally dominant part of the analysis is the calculation of the Fisher matrix. The Fisher matrix has $(l + 1)^4$ elements, with $(l + 1)^2$ the number of basis vectors. The symmetries in the spherical harmonic basis help to reduce the computational load. However, reading, writing and saving the Fisher matrices and the dirty maps are memory and disk space limited. The larger the l , the higher the memory and disk space requirements.

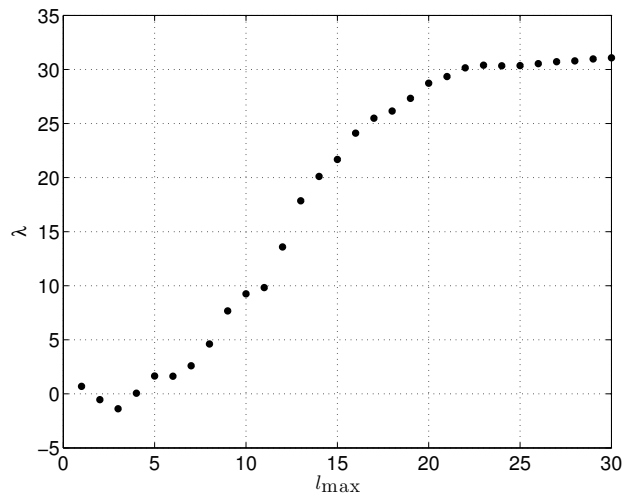


Figure 3.9: The MLR statistic of a simulated SGWB in the Virgo cluster is computed and plotted for different harmonic cutoff.

Here we do a Monte Carlo simulation to choose the harmonic cutoff. Following the diffraction formula, the larger the baseline, the higher the resolution. However, we consider 15 days of data from S5 science run with coincident between H1 and L1. We inject a signal, following the above $\mathcal{P}_{\text{model}}$ and simple

power-law spectrum, into the data stream. The data were first processed with $l_{\max} = 30$, and later with different lower l_{\max} . The MLR statistic for different choices of l_{\max} cutoff is presented in Fig. 3.9. It is obvious from the plot that λ saturates at $l_{\max} = 25$. So, we adopt $l_{\max} = 25$ to search for the SGWB from NSs in the Virgo cluster. It is also found in a similar study that the known sky-distribution of the source contributes about 10% more to the signal-to-noise ratio than the unknown counterpart.

3.5 Discussion

Since the search is ongoing and it requires internal review, we do not report the data analysis results here. The actual population of NSs in the Virgo cluster is unknown. Searching for their SGWB profile with current and advanced detectors has a merit if the actual number exceeds our expectation. The analysis itself is nevertheless interesting, because even if we do not detect the signal, we can put an upper limit on the average ellipticity of the NSs in the Virgo cluster. In addition to searching for SGWB targeting the Virgo cluster, we perform an all-sky search using the same spectra. This will allow us to compare the results from targeting the Virgo cluster with those from an all-sky search, and hence address Olbers' paradox. Extending this analysis to other targets (e.g., NSs in the Coma cluster) and searching for them in advanced detectors' data are straightforward.

Chapter 4

Searching for perturbed black hole ringdown signals

In this chapter, we study the methods of detecting the *ringdown* phase of a GW signal that arises from a perturbed black hole. Such a black hole can result from the coalescence of a compact binary, a massive object falling into a BH or the formation of a BH through the asymmetric core collapse of a massive star. This signal is initially in the form of a superposition of quasi-normal modes [122]. However, at late times the waveform, which is known as a ringdown, is expected to be dominated by a single mode. The existence of intermediate-mass black holes (IMBHs), which have masses from hundreds to tens of thousands of solar masses, has not yet been corroborated observationally. However, these objects are of great interest for astrophysics and their discovery by LIGO and VIRGO in the GW spectrum is an interesting possibility.

The optimal method for searching such a signal buried in detector noise is

to match-filter the detectors' output with theoretically modeled waveforms. The coherent network statistic is optimal for detecting these signals in stationary, Gaussian noise [46, 47]. But in real noise, which is non-Gaussian and non-stationary, that statistic is sub-optimal unless additional discriminators of noise artifacts are employed [12]. Here, we describe a hierarchical method for coherently searching ringdown signals in a network of detectors that is aided by such discriminators.

4.1 Motivation for the search

A black hole itself does not emit any signals from within its horizon classically, thus making it invisible and difficult to detect directly. However, astronomers can infer the presence of a black hole by electromagnetically observing the influence of its strong gravity on nearby matter. In recent years, evidence has mounted for both stellar-mass black holes and supermassive black holes. Stellar-mass BHs are born in the collapse of massive stars and have masses in the range $3 M_{\odot} \leq M \leq 20 M_{\odot}$. From the discovery of a number of bright X-ray sources, it is evident that there are many binaries in our Galaxy and other galaxies that consist of a stellar-mass BH, which accretes matter from a stellar companion [76, 77, 78, 79]. Supermassive BHs, which are believed to be the engines behind quasars, have masses of $10^6 M_{\odot}$ to $10^{10} M_{\odot}$. Observations of the stellar environment near galactic centers, especially the high luminosity and small size of active galactic nuclei, provide the strongest empirical evidence for the existence of massive black holes in the center of most galax-

ies [80, 81, 82, 83, 84, 85, 86, 87, 88, 89]. The formation of supermassive BHs is not as well established as the formation of stellar-mass BHs, but it is theorized that they are produced during collisions between galaxies, or in a series of collisions between BHs that have masses greater than those of stellar-mass BHs, but significantly less than those of supermassive BHs.

Observations of ultraluminous X-ray sources in galaxies and presence of excess dark mass in globular-cluster cores suggest that there may exist a population of intermediate-mass black holes with masses $M \sim 10^2 - 10^4 M_{\odot}$ [90]. But the existence of IMBHs has never been confirmed [91]. Several IMBH formation mechanisms have been proposed: (a) Formation of IMBHs in young clusters via runaway collapse of stars [92, 93, 94]. (b) Formation of IMBHs in globular clusters through repeated mergers of stellar-mass BHs in binaries [95, 96]. (c) Formation of lower mass single IMBHs by the stalled supernova of early Population III stars [90, 97]. (d) Formation of IMBHs from progressive accumulation of mass into a large seed black hole via coalescence of a population of smaller-mass BHs [95]. (e) IMBHs could be the relics of very massive metal-free stars [98]. The existence of binaries with IMBH components remains uncertain since stellar winds may stall the growth of the IMBH progenitors in the runaway collision scenario [99], or the merger recoil may also eject a newly formed black hole from the globular cluster [100, 101].

Some recent observations indicate that IMBHs could exist in the core of globular clusters [102, 103, 104, 105]. These objects are thought to grow from accretion of smaller compact objects [106]. It has been suggested that IMBHs are the engines powering ultraluminous X-ray sources, such as M82 X-1 [107, 108, 109]

and NGC 1313 X-2 [110, 111]. Ultraluminous X-ray sources are found off-center in young star clusters in starburst galaxies: X41.4 + 60 in M82 has approximate mass range of $500 - 10^5 M_{\odot}$ [112, 113] and HLX-1 in ESO 243-49 has a lower mass limit of approximately $500 M_{\odot}$ [114].

The detection of GWs from IMBHs could have important consequences for theories about the formation of supermassive black holes and the dynamics and evolution of globular clusters [115, 116] and could ascertain information about their masses and spin parameters. The merger and ringdown phases of the GW signal are important for detection of IMBH sources because for massive systems the characteristic frequencies of the inspiral phase are usually outside a detector's frequency band.

4.2 Quasi-normal modes of black holes

According to GR, a black hole (BH) is a region of space-time where gravity is so strong that nothing, not even light, can escape it. At the center of a black hole, space-time has a curvature singularity. That singularity is enclosed by an "event horizon", a mathematically defined surface that marks the point of no return for an object falling in. Black holes can have masses varying from a few solar masses to millions of solar masses. In general, a black hole can be completely characterized by three parameters, namely, its mass, spin and charge. And only the mass and spin are likely to be significant for any astrophysical black hole.

4.2.1 Schwarzschild and Kerr black holes

The Kerr-Newman metric is a stationary and axisymmetric solution of the Einstein-Maxwell equations, describing the space-time geometry in the region surrounding a charged, rotating black hole [117]. The other stationary black hole solutions can be obtained as particular cases of the Kerr-Newman solutions. The space-time geometry outside an uncharged non-spinning spherical black hole of mass M is given by the Schwarzschild metric

$$ds^2 = - \left(1 - \frac{2GM}{c^2 r}\right) c^2 dt^2 + \left(1 - \frac{2GM}{c^2 r}\right)^{-1} dr^2 + r^2 d\theta^2 + r^2 \sin^2 \theta d\phi^2. \quad (4.1)$$

And the space-time geometry outside an uncharged spinning black hole of mass M and angular momentum J is described, in terms of the Boyer-Lindquist coordinates (r, θ, ϕ) , by the Kerr metric

$$ds^2 = - \left(1 - \frac{2GMr}{c^2 \Sigma}\right) c^2 dt^2 - \frac{4GMra \sin^2 \theta}{c \Sigma} d\phi dt + \frac{\Sigma}{\Delta} dr^2 + \Sigma d\theta^2 + \left(r^2 + a^2 + \frac{2GMra^2 \sin^2 \theta}{c^2 \Sigma}\right) \sin^2 \theta d\phi^2, \quad (4.2)$$

where $a \equiv J/cM$ is the spin parameter, $\Sigma \equiv r^2 + a^2 \cos^2 \theta$ and $\Delta \equiv r^2 - 2GMr/c^2 + a^2$. From this point on, unless otherwise mentioned, we refer to the spin by a dimensionless spin parameter $\hat{a} = Jc/GM^2$. This parameter can take values ranging from 0 (Schwarzschild BH) to 1 (extreme Kerr BH).

4.2.2 Black hole perturbation

The theory of black hole perturbations and the associated radiation has a long history. The study of BH perturbations was initiated by the pioneering work of

Regge and Wheeler [118] and was continued by Zerilli [119] and Chandrasekhar and Detweiler [120, 121]. Their study found that black holes remain stable if subjected to a small perturbation. Their study also showed that the solution to the linearized Einstein Equation can be expressed in terms of spherical harmonics Y_{lm} . The existence of *quasi-normal modes* (QNMs) of a BH was first pointed out by Vishveshwara [122] in calculations of the scattering of gravitational waves by a Schwarzschild black hole. In GR, quasi-normal modes arise as perturbations of stellar or black hole space-time. QNM oscillations have been found in perturbation calculations of particles falling into Schwarzschild [123] and Kerr black holes [124, 125] and in the collapse of a star to form a black hole [126, 127, 128]. A nice review of quasi-normal modes can be found in Ref. [129]. A BH can be perturbed in a variety of ways, e.g., by the incidence of GWs, by an object falling into it, by the interaction with a companion, by the accretion of matter surrounding it, or by the formation process in a gravitational collapse. There are no normal mode oscillations associated with non-radial perturbations. This is in contrast with the normal modes of Newtonian gravity, because in GR they are damped by the emission of GWs and, hence, they are called quasi-normal modes. Each mode has a characteristic complex frequency, whose real part represents the actual frequency of the oscillation and whose imaginary part represents the inverse of the damping time. We express the angular frequency ω_{lm} in terms of the oscillation frequency f_{lm} and the quality factor Q_{lm} as

$$\omega_{lm} = 2\pi f_{lm} - i\tau_{lm}^{-1} = 2\pi f_{lm} - i\frac{\pi f_{lm}}{Q_{lm}}, \quad (4.3)$$

where τ is the damping time.

4.2.3 The ringdown waveform

Numerical simulations (see for example, Refs. [130, 131]) have demonstrated that the fundamental mode, $l = m = 2$, dominates the GW emission. Far from the source, the plus and cross polarizations of a ringdown waveform can be expressed in terms of the central frequency $f_0 \equiv f_{22}$ and the quality factor $Q \equiv Q_{22}$ as [132, 133, 134, 135]

$$h_+(t) = \mathcal{A} (1 + \cos^2 \iota) e^{-\frac{\pi f_0 t}{Q}} \cos(2\pi f_0 t), \quad (4.4)$$

$$h_\times(t) = \mathcal{A} (2 \cos \iota) e^{-\frac{\pi f_0 t}{Q}} \sin(2\pi f_0 t), \quad (4.5)$$

where \mathcal{A} is the amplitude of the $l = m = 2$ mode, and ι is the inclination angle of the source. The strain produced in the detector is then

$$h(t) = h_+(t)F_+(\theta, \phi, \psi) + h_\times(t)F_\times(\theta, \phi, \psi), \quad (4.6)$$

where $F_{+,\times}$ are the detector antenna-pattern functions (see Appendix A.1 for more details), with ψ being the wave-polarization angle and (θ, ϕ) being the sky-position of the source. For a given source at a distance r , one defines the effective distance as

$$D_{\text{eff}} = \frac{r}{\sqrt{F_+^2 (1 + \cos^2 \iota)^2 / 4 + F_\times^2 \cos^2 \iota}}. \quad (4.7)$$

The effective distance gives the distance to a BH as if it were optimally located and oriented.

Following Refs. [136, 133, 135], the ringdown waveform is approximated by

$$h_0(t - t_0) = \mathcal{A} e^{-\frac{\pi f_0 t}{Q}} \cos(2\pi f_0 t - \varphi_0), \quad (4.8)$$

were φ_0 is the signal's initial phase and t_0 is the time of arrival at the detector. If ϵ is the fraction of the black hole's mass radiated as gravitational waves, then the amplitude is given by [134]

$$\mathcal{A} = \sqrt{\frac{5}{2}} \epsilon \left(\frac{GM}{c^2 r} \right) Q^{-1/2} F(Q)^{-1/2} g(\hat{a})^{-1/2}, \quad (4.9)$$

where $g(\hat{a}) = [1.5251 - 1.1568(1 - \hat{a})^{0.1292}]$ and $F(Q) = 1 + \frac{7}{24Q^2}$, M is the black hole mass, c is the speed of light, G is the gravitational constant, and r is the distance to the source. An example of a ringdown waveform is shown in Fig. 4.1. The frequency and quality factor for each quasi-normal mode can be related

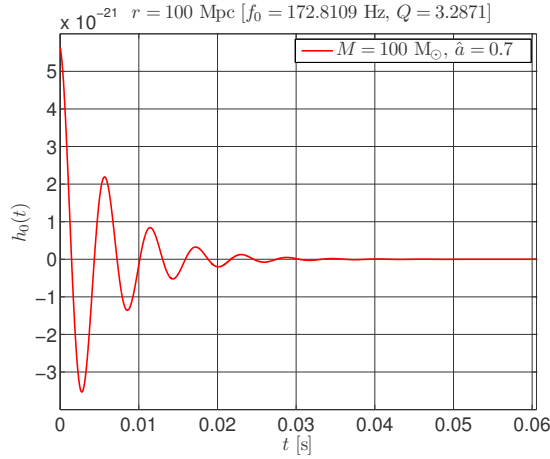


Figure 4.1: Ringdown waveform for a black hole of mass $M = 100 M_\odot$ and spin $\hat{a} = 0.7$ corresponding to frequency $f_0 = 172.8109$ Hz and quality $Q = 3.2871$, at a distance of $r = 100$ Mpc.

to the black hole mass M and dimensionless spin parameter \hat{a} through fitting

formula [141, 142, 143, 144, 145]. For the $l = m = 2$ mode, we have

$$Q = 0.7000 + 1.4187(1 - \hat{a})^{-0.4990}, \quad (4.10)$$

$$f_0 = \frac{1}{2\pi} \frac{c^3}{GM} \left[1.5251 - 1.1568(1 - \hat{a})^{0.1292} \right], \quad (4.11)$$

and the inverse relationship is given by

$$\hat{a} = 1 - \left(\frac{Q - 0.7000}{1.4187} \right)^{-2.0040}, \quad (4.12)$$

$$M = \frac{1}{2\pi} \frac{c^3}{Gf_0} \left[1.5251 - 1.1568 \left(\frac{Q - 0.7000}{1.4187} \right)^{-0.2589} \right]. \quad (4.13)$$

Note that Q is determined by \hat{a} and f_0 is determined by M and \hat{a} . Figure 4.2 shows how frequency and quality factors are related to mass and spin.

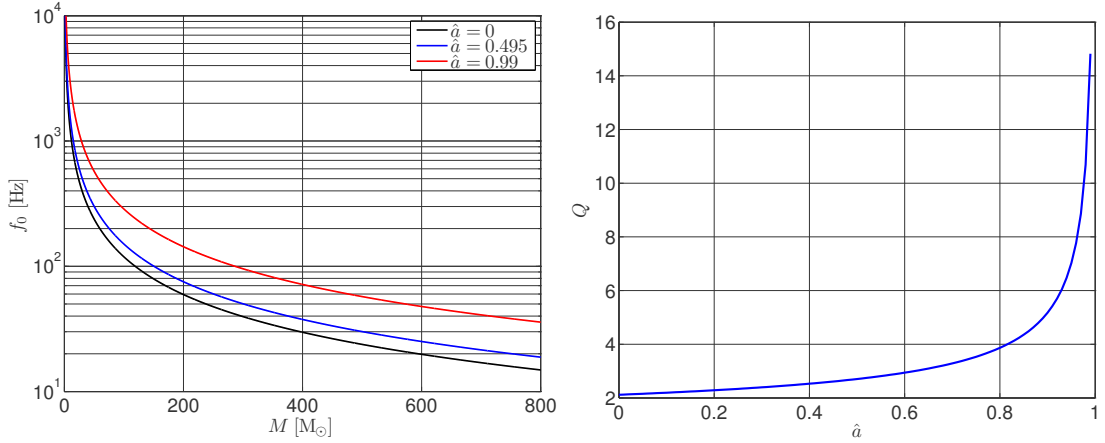


Figure 4.2: Central frequency of the ringdown waveform is plotted as a function of mass for three spin values (left). The mass range (above a few solar masses) reflects the sources that earth-based detectors are most sensitive to. Quality factor is plotted as a function of the dimensionless spin parameter (right).

4.3 Ringdown searches with matched filtering

When the signal is known, the optimal method of extracting the signal from Gaussian noise is matched filtering [26]. We filter the strain data from a detector with each template characterized by either mass and spin or frequency and quality factor. A trigger is generated when the signal-to-noise ratio (SNR) yielded by matched filter crosses a pre-defined threshold for a given filter. Of course, the threshold is chosen carefully so as to minimize the false dismissal rate for a given false-alarm rate. The higher the threshold, the more significant the trigger. However, as the noise in the data stream is non-stationary and non-Gaussian, matched filtering alone is not enough to establish the significance of a trigger as a GW signal. Noise can often mimic the signal we are searching for, and so a large effort goes into characterizing the noise to best separate it from a potential gravitational wave signal.

4.3.1 Matched filter

In GW data analysis, the data from multiple detectors is match-filtered with templates derived from theoretical waveforms to test the presence or absence of signals in the data. Filtering the data $x(t)$ with an elliptically-polarized template $h_{\text{ep}}(t; \mu_i)$ characterized by the source parameters μ_i yields the SNR statistic given by

$$\rho_{\text{ep}}(h_{\text{ep}}) = \frac{|\langle x, h_{\text{ep}} \rangle|}{\sqrt{\langle h_{\text{ep}}, h_{\text{ep}} \rangle}} \equiv \frac{|\langle x, h_{\text{ep}} \rangle|}{\sigma_{\text{ep}}}, \quad (4.14)$$

where $\langle x, h_{\text{ep}} \rangle$ denotes the noise-weighted scalar product of the data and the template defined in Eq. (5.10). The data $x(t)$ may or may not contain a signal

and is expressed as

$$x(t) = \begin{cases} n(t), & \text{if signal is absent.} \\ n(t) + h(t), & \text{if signal is present.} \end{cases} \quad (4.15)$$

Far from the source, the ringdown template can be expressed as

$$h_{\text{ep}}(t) = e^{-\frac{\pi f_0 t}{Q}} \{\cos(2\pi f_0 t) - i \sin(2\pi f_0 t)\}. \quad (4.16)$$

This choice is equivalent to modeling the template as $e^{-\frac{\pi f_0 t}{Q}} \cos(2\pi f_0 t - \varphi_0)$ in matched filter searches. For each template, triggers that have SNRs greater than a pre-defined threshold are retained. These triggers are used for determining coincidence across different detectors.

4.3.2 Template banks

Although the form of the signal is known, the exact values of the intrinsic parameters are unknown. For the ringdown waveform, these parameters are the central frequency f_0 and the quality factor Q . We create a bank of templates to search over the range of intrinsic parameters of interest. We then filter the data with each of the templates in the bank. The templates are placed discretely in the parameter space. If the signal parameters match those of a template and the SNR crosses the pre-defined threshold, we record the template parameter, the time of the trigger and other relevant information. In general, more than one template in the bank can generate a trigger for a given signal. We then obtain an estimate of the intrinsic parameters for the source of the signal from the template that provided the largest SNR.

In order to understand how to place templates in the parameter space, we define two templates $\tilde{u}(f; \boldsymbol{\mu}, \boldsymbol{\lambda})$ and $\tilde{u}(f; \boldsymbol{\mu} + \Delta\boldsymbol{\mu}, \boldsymbol{\lambda} + \Delta\boldsymbol{\lambda})$ characterized by intrinsic parameters $\boldsymbol{\lambda}$ and extrinsic parameters $\boldsymbol{\mu}$, such as time of arrival and phase. The *match*, M , between two templates is defined as the inner product maximized over the extrinsic parameters:

$$M(\boldsymbol{\lambda}, \Delta\boldsymbol{\lambda}) \equiv \max_{\boldsymbol{\mu}, \Delta\boldsymbol{\mu}} \langle u(\boldsymbol{\mu}, \boldsymbol{\lambda}), u(\boldsymbol{\mu} + \Delta\boldsymbol{\mu}, \boldsymbol{\lambda} + \Delta\boldsymbol{\lambda}) \rangle. \quad (4.17)$$

This is the fraction of the SNR achieved by filtering a signal with parameters $\boldsymbol{\lambda}$ against a template with parameters $\boldsymbol{\lambda} + \Delta\boldsymbol{\lambda}$ [43]. Expanding M in a power series about $\Delta\boldsymbol{\lambda}$ gives

$$M(\boldsymbol{\lambda}, \Delta\boldsymbol{\lambda}) \approx 1 + \frac{1}{2} \left(\frac{\partial^2 M}{\partial \Delta\lambda^i \partial \Delta\lambda^j} \right)_{\Delta\lambda^k=0} \Delta\lambda^i \Delta\lambda^j. \quad (4.18)$$

The metric in the template bank is defined by the *mismatch*, $(1 - M)$, which is just the square of the proper distance between templates

$$ds^2 \equiv 1 - M = g_{ij} \Delta\lambda^i \Delta\lambda^j, \quad (4.19)$$

where the metric is given by

$$g_{ij}(\boldsymbol{\lambda}) = -\frac{1}{2} \left(\frac{\partial^2 M}{\partial \Delta\lambda^i \partial \Delta\lambda^j} \right)_{\Delta\lambda^k=0}. \quad (4.20)$$

Having defined this metric on the intrinsic parameter space, we can now use it to calculate the spacing of the discrete template family required to retain a given fraction of the ideal event rate.

4.4 A coincident multi-detector search

The first LSC ringdown search was carried out by Creighton [136] with a single filter on data from the LIGO 40 m prototype in 1994 using the GRASP soft-

ware [137]. In 2004, Adhikari [138] performed a coincident ringdown search on 300-hour-long data from the LIGO S2 science run using LAL software [176]. The TAMA collaboration also carried out a search for ringdown signals using data from their 300 m interferometer [139]. In 2009, a 90%-confidence upper limit was placed on the rate of ringdowns from black holes with mass between $85 M_{\odot}$ and $390 M_{\odot}$ in the local universe, assuming a uniform distribution of sources, of $3.2 \times 10^{-5} \text{ yr}^{-1} \text{ Mpc}^{-3}$ [133, 134]. This search was carried out on data from LIGO S4 science run, which took place between February 22 and March 24, 2005. Let us name it the “LIGO S4 ringdown search”. This includes a total of 567.4 hours of analyzable data from H1, 571.3 hours from H2, and 514.7 hours from L1. This yielded 360 hours of data in coincidence among H1, H2, and L1. To check whether a signal is in coincidence between detectors, a test is applied separately on time, frequency and quality factor. The upper limit was presented based on the study of simulated ringdown only signals added in the data stream by software. A weakly modeled burst search for GWs from mergers of non-spinning intermediate-mass binary black holes was performed on data from LIGO S5 and VIRGO VSR1 science runs. A 90%-confidence upper limit of $0.13 \text{ Myr}^{-1} \text{ Mpc}^{-3}$ is placed on the rate of non-spinning sources with component masses $m_1 = m_2 = 88 M_{\odot}$ [140]. In the following sections, we present the method for searching for GWs from perturbed BH ringdown signals in the data from LIGO S5/S6 and VIRGO VSR2/VSR3 science runs. We refer to it as the “LIGO-VIRGO S5/S6 ringdown search”.

4.4.1 The coincidence search pipeline

The “ringdown search pipeline”, illustrated in Fig. 4.3, is a multi-detector data analysis pipeline designed for searching the $l = m = 2$ quasi-normal mode of gravitational waves from perturbed black holes [134, 133]. Here we summarize the main steps. The first stage of the pipeline involves reading in and conditioning the data from each of the detectors. We read in uncalibrated data at a sampling rate of 16384 Hz, low-pass filter it to remove any power above 4096 Hz as a part of downsampling it to 8192 Hz to reduce the computational cost. The data is then high-pass filtered to remove power below 40 Hz. This is converted to strain by applying the detector response function. The one-sided power spectral density is calculated for each 2176s long segment of the calibrated data. The data is then broken further into sets of 16 overlapping blocks, each 256s in length, and filtered using a bank of ringdown templates. This segmentation is discussed in more detail in Ref. [185]. Once the triggers are generated, we require coincidence of a trigger from at least two detectors in waveform parameters to increase the confidence level for the presence of a signal. At this stage we also veto triggers occurring during times when data quality flags are on.

4.4.1.1 Data set

The search uses data from LIGO S5 and S6 science runs and from VIRGO VSR2 and VSR3 science runs. LIGO S5 science run took place between 2005 November 4 and 2007 October 1, during which time the detectors reached the initial LIGO (iLIGO) design sensitivity. The detectors had duty factors of 78% for H1, 79% for H2, and 66% for L1. We exclude data from VIRGO VSR1 science run. That

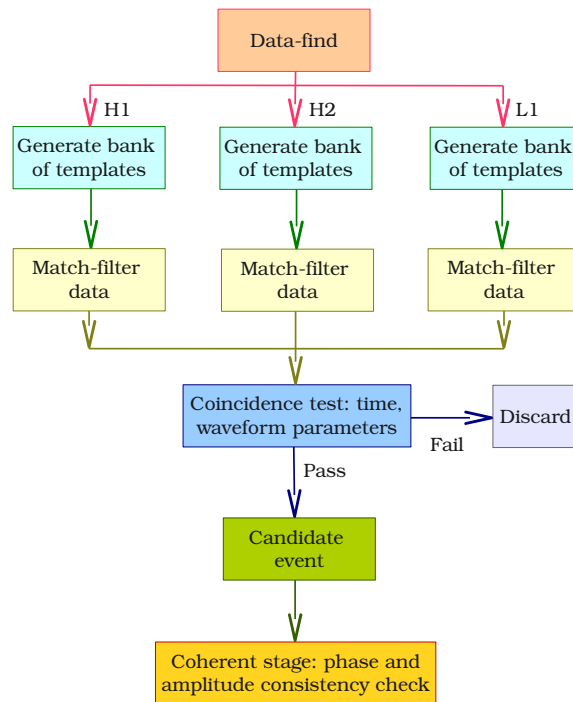


Figure 4.3: A schematic diagram of the coincidence and coherent (see Section 4.5) stages of the ringdown search pipeline. The LIGO detectors (H1, H2 and L1) are considered as an example of this diagram.

means we only analyze data from H1, H2, and L1 detectors during S5/VSR1. We sometimes refer to this as the “LIGO S5 ringdown search”. LIGO S6 science run was held from 2009 July 07 to 2010 October 20. During this run, the 4 km H1 and L1 detectors were operated at sensitivities that surpassed that of the previous S5 run, with duty factors of 52% and 47%. The 2 km H2 detector was not operated during S6. VIRGO VSR2 science run was held from 2009 July 07 to 2010 January 08 with an improvement in sensitivity roughly a factor of

2 over VIRGO VSR1 science run. VIRGO VSR3 was held from 2010 August 11 to 2010 October 20. The overall Virgo duty cycle over VSR2 and VSR3 was 78%. Figure 1.4 shows the best sensitivities, in terms of noise spectral density, of the LIGO interferometers during S5 science run. Using the power spectrum we can estimate a detector's horizon distance, D_H , which is the distance at which a specified source with optimal location and orientation produces a SNR of 8 in that detector. We consider a spinning black hole with $\hat{a} = 0.7$ and $\epsilon = 0.01$ (where ϵ is the fraction of BH mass emitted as GWs). Figure 4.4 shows the horizon distance as a function of mass for LIGO/VIRGO detectors at the best sensitivities during their joint S5/VSR1 science run.

4.4.1.2 Template placement

The ringdown analysis pipeline constructs a two-dimensional lattice template bank in the (f_0, Q) space where the mismatch between two templates differing in ringdown frequency by df_0 and in quality factor by dQ is given by the metric [133].

$$ds^2 = \frac{1}{8} \left[\frac{3 + 16Q^4}{Q^2(1 + 4Q^2)^2} dQ^2 - 2 \frac{3 + 4Q^2}{f_0 Q(1 + 4Q^2)} dQ df_0 + \frac{3 + 8Q^2}{f_0^2} df_0^2 \right], \quad (4.21)$$

which assumes white noise. The mismatch is defined in terms of $\phi \equiv \log(f_0)$ so that the metric coefficients in the (Q, ϕ) variables are independent of f_0 :

$$ds^2 = \frac{1}{8} \left[\frac{3 + 16Q^4}{Q^2(1 + 4Q^2)^2} dQ^2 - 2 \frac{3 + 4Q^2}{Q(1 + 4Q^2)} dQ d\phi + (3 + 8Q^2) d\phi^2 \right], \quad (4.22)$$

$$= g_{QQ} dQ^2 + g_{Q\phi} dQ d\phi + g_{\phi\phi} d\phi^2. \quad (4.23)$$

Currently, the population algorithm uses only the diagonal terms containing df_0^2 and dQ^2 . Starting with the smallest central frequency and quality factor, the

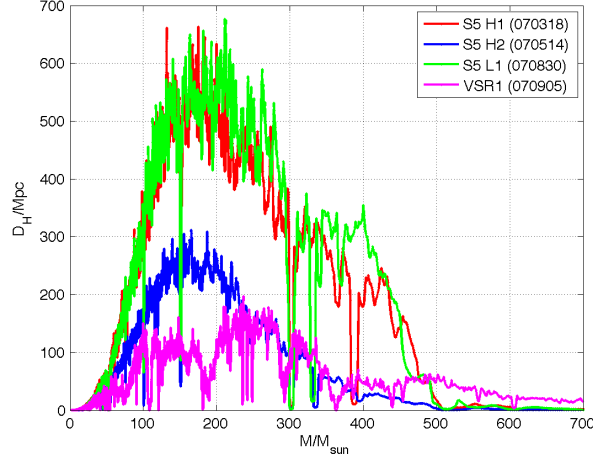


Figure 4.4: The ringdown horizon distance as a function of mass for a black hole with spin $\hat{a} = 0.7$ and $\epsilon = 0.01$ plotted for LIGO and VIRGO detectors. For LIGO 4 km detectors during S5 science run, the ringdown horizon distance for a black hole of mass $210 M_{\odot}$ reached about 600 Mpc. The quantity in parentheses represents date in YYMMDD format when the horizon distance shown here was measured.

algorithm places templates along Q in steps of [145, 146]

$$dQ = \frac{ds_{\text{eff}}Q(1 + 4Q^2)}{\sqrt{3 + 16Q^4}}, \quad (4.24)$$

and along $d\phi = d \log(f)$ in steps of

$$d\phi = \frac{ds_{\text{eff}}}{\sqrt{3 + 8Q^2}}, \quad (4.25)$$

where $ds_{\text{eff}} = 4\sqrt{(1 - \text{MM})}$ and MM is the specified minimal match between the template and signal. The templates are placed in $\log(f_0)$ and Q space such that the mismatch between any signal and its closest template is 3% or less. Figure 4.5 shows the ringdown template bank for $f_0 \in [50, 2000]$ Hz, $Q \in [2.1187, 20]$

used in this study. For this bank, $ds^2 = 0.03$ and it has a total of 615 templates. The frequency spacing of the templates is finer for lower frequencies and for higher quality factors. The template placement can be well understood by looking at the contours of constant mismatch around each template in the bank. These contours form overlapping ellipses in the template parameter space. Each contour covers a region in the template parameter space so that any given signal in that region will match a template by no less than 97%. Figure 4.6 illustrates the contours around templates for a single frequency and for a snippet of the template bank.

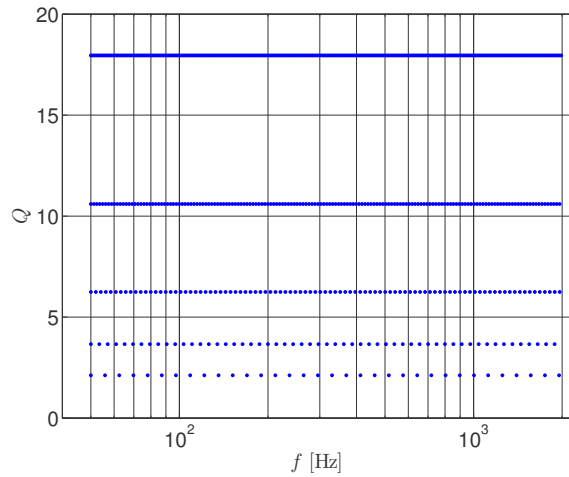


Figure 4.5: The template bank for the LIGO-VIRGO S5/S6 ringdown search.

Following Refs. [133, 136, 134], the template used in this search is given by

$$h_c(t) = e^{-\frac{\pi f_0 t}{Q}} \cos(2\pi f_0 t), \quad 0 \leq t \leq t_{\max} \quad (4.26)$$

with a length of 10 e-folding times, $t_{\max} = 10\tau$, where $\tau = Q/\pi f_0$. In order to illustrate the parameter space covered in this search, we plot expected signals

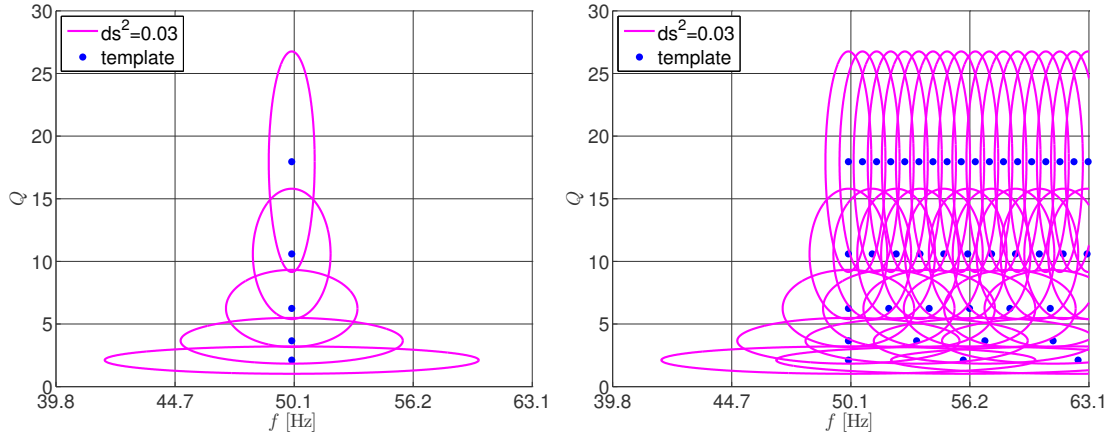


Figure 4.6: Contours of $ds^2 = 0.03$ around templates of a constant frequency (left) and for a portion of the template bank (right).

in time domain (see Fig. 4.7), in the extremes of the parameter space. Figure 4.7 shows the signals in the extremes of the parameter space characterized by frequency and quality factor. Using the relations given in Eqs. (4.12) and (4.13), we tabulate the masses and spins, corresponding to the extreme frequencies and quality factors, in Table 4.1.

4.4.1.3 Trigger generation

For the ringdown template given in Eq. (4.26), the SNR is

$$\rho_c(h_c) = \frac{|\langle x, h_c \rangle|}{\sqrt{\langle h_c, h_c \rangle}} \equiv \frac{|Z_c|}{\sigma_c}. \quad (4.27)$$

In practice, the detector output is not continuous but is a discretely sampled quantity with sampling interval Δt seconds,

$$x_j \equiv x(t_j), \quad (4.28)$$

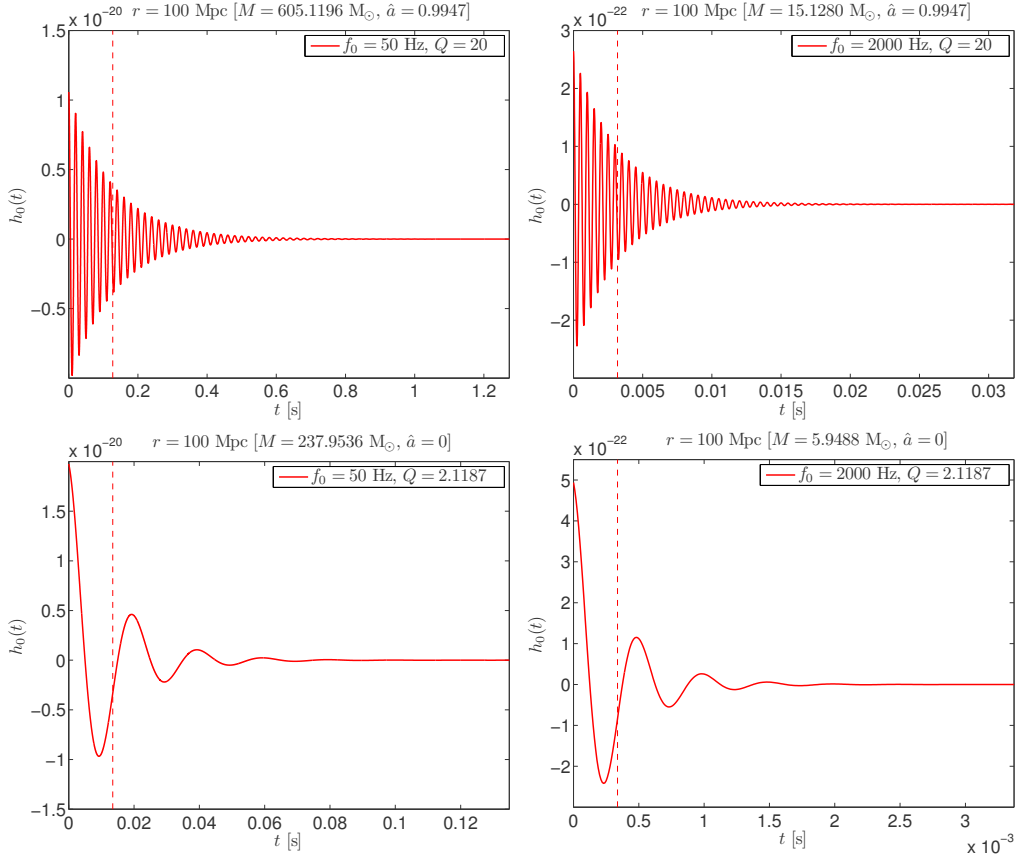


Figure 4.7: Ringdown waveforms in the extremes of the parameter space, characterized by central frequency and quality factor. To illustrate the short nature of these waveforms, the e-folding time is also marked with a dashed line.

where $t_j = j\Delta t$. Thus, in order to filter the data we need to recast the expressions described above. The digital matched filter operates on a single data segment consisting of N consecutive samples of $x(t_j)$. The length of this data segment is $T = N\Delta t$ s. The frequency domain quantity $\tilde{x}(f_k)$ denotes the value of the continuous function $\tilde{x}(f)$ at a particular frequency, labeled

$$f_k = \frac{k}{N\Delta t}. \quad (4.29)$$

Table 4.1: Extreme (pair) values for frequency and quality factor of the ringdown template bank, together with their corresponding masses and spins.

f_0 (Hz)	Q	M (M_\odot)	\hat{a}
50	2.1187	237.9536	0
2000	2.1187	5.9488	0
50	20	605.1196	0.9947
2000	20	15.1280	0.9947

If the units of x_j are counts, then $\tilde{x}(f_k)$ has units of counts/Hz. We define \tilde{x}_k by

$$\tilde{x}_k = \frac{\tilde{x}(f_k)}{\Delta t}, \quad (4.30)$$

which has units of counts. Negative k defines negative frequencies. Since $x(t_j)$ is sampled at intervals of Δt , the sampling theorem implies that $x(t_j)$ is bandwidth limited to the frequency range $-f_{\text{Ny}} \leq f \leq f_{\text{Ny}}$, where $f_{\text{Ny}} = 1/(2\Delta t)$ is the Nyquist frequency. Any power in $x(t)$ at frequencies above f_{Ny} will be aliased into the range $-f_{\text{Ny}} \leq f \leq f_{\text{Ny}}$, thus, corrupting the data. To prevent this, data of frequency higher than f_{Ny} are removed using analog low-pass filters before the data is digitized. Therefore, $x(t_j)$ completely determines the data $x(t)$ in the band of interest. Thus the Fourier transformed data is expressed as

$$\tilde{x}_k = \sum_{j=0}^{N-1} x_j e^{-i2\pi jk/N}, \quad (4.31)$$

and its inverse Fourier transform is given by

$$x_j = \frac{1}{N} \sum_{k=0}^{N-1} \tilde{x}_k e^{i2\pi jk/N}. \quad (4.32)$$

Similarly, the template used in this search is given in its discrete form by

$$h_{cj} \equiv h_c(t_j) = e^{-\frac{\pi f_0 j \Delta t}{Q}} \cos(2\pi f_0 j \Delta t), \quad (4.33)$$

The template time series is Fourier transformed to get $\tilde{h}_{ck} \equiv \tilde{h}_c(f_k)$.

The filtering is done in Fourier domain template by template for each of the sixteen 256s overlapping block of data in a 2176s analysis segment. Then the filter output is inverse Fourier transformed to get the time series

$$|Z_{cj}| = \frac{2}{N\Delta t} \Re \left\{ \sum_{k=1}^{N/2-1} \frac{S_v^{-1}}{dyn R} (\Delta t \tilde{x}_k^*) (\Delta t \tilde{h}_{ck}) e^{-i2\pi jk/N} \right\}, \quad (4.34)$$

where the inverse calibrated power spectrum

$$\frac{1}{\xi(f)} = \frac{1}{dyn^2 R^2} S_v^{-1} \quad (4.35)$$

is expressed in terms of uncalibrated spectral density $S_v(f)$, response function $R(f)$, and the ‘‘dynamical range factor’’ $dyn = 10^{20}$ [134]. The numerical value of the response function is very small, so to save the computational cost of extra precision we scale this quantity by the dynamical range factor. Note that in Eq. (4.34) we set the DC ($k = 0$) term and the Nyquist frequency ($k = N/2$) term to zero. The variance of the template is evaluated as

$$\sigma_c^2 = \frac{4}{N\Delta t} \sum_{k=1}^{N/2-1} \frac{S_v^{-1}}{dyn^2 |R|^2} \left[(\Re \{ \Delta t \tilde{h}_{ck} \})^2 + (\Im \{ \Delta t \tilde{h}_{ck} \})^2 \right] dyn^2. \quad (4.36)$$

Using the pre-defined threshold on the SNR, ρ_{c*} , we calculate the equivalent threshold on the filter output, $|Z_c|_*$. For a given template we compute

$$|Z_c|_* = \rho_{c*} \frac{\sigma_c}{2 dyn} \quad (4.37)$$

and compare it with $|Z_c|$. We cluster those triggers above threshold in time of 1s sliding window [134]. The trigger with the loudest SNR in a cluster of triggers

is marked as the trigger to be recorded. The SNR of the clustered triggers is calculated as

$$\rho_c(t_j) = |Z_c(t_j)| \frac{2 \text{ dyn}}{\sigma_c}. \quad (4.38)$$

The amplitude \mathcal{A} is calculated (according to Eq. (4.9)) from the template parameters f_0 and Q , and with $\epsilon = 0.01$ and the distance to the source $r = 0.5$ Mpc. The effective distance is a derived quantity based on the amplitude and the sensitivity of the detector to a source at 1 Mpc. This sensitivity is calculated as

$$\sigma^2 = (1 \text{ Mpc}) \sigma_c^2 \mathcal{A}^2, \quad (4.39)$$

from which the effective distance of the trigger is estimated

$$D_{\text{eff}} = (1 \text{ Mpc}) \frac{\sigma}{\rho_c}. \quad (4.40)$$

All of the parameters mentioned here are recorded for each trigger.

4.4.1.4 Coincidence analysis

Once triggers are found in one detector they are checked for parameter consistency and time delay with triggers from other detectors, operating concurrently. This is commonly known as a coincidence test. Triggers failing this test are discarded. Whereas, triggers fulfilling the test are recorded as coincidences and are followed up further because they can be signals.

Random noise is considered to be uncorrelated between geographically separated detectors. Thus, requiring coincidence between triggers of separated detectors lowers the false alarm rate significantly [150]. In LIGO S4 ringdown search, the coincidence test was composed of two separate stages. The time requirement

is enforced first, only allowing triggers that appear within 4 ms of each other for co-located detectors (H1-H2 pair) and 14 ms for the H1-L1 pair. Note that H1 and L1 observatories are separated by 10 ms of light travel time. The second coincidence test is based on the metric used for template placement to measure the distance between the triggers' template parameters [133]. However, it was found that the time of arrival difference of recovered coincidences is actually frequency dependent, which led to having a frequency dependent time-difference cut, instead of a flat dt cut. In this S5 search, we apply a coincidence test that uses the 3D metric in (f_0, Q, t) space to compute the distance between coincident triggers [146]:

$$\begin{aligned}
ds^2 = & \frac{1 + 6Q^2 + 16Q^4}{4f_0^2(1 + 2Q^2)} df_0^2 + \frac{1 + 28Q^4 + 128Q^6 + 64Q^8}{4Q^2(1 + 6Q^2 + 8Q^4)^2} dQ^2 \\
& + \frac{\pi^2 f_0^2(1 + 4Q^2)}{Q^2} dt^2 - \frac{1 + 2Q^2 + 8Q^4}{2f_0Q(1 + 6Q^2 + 8Q^4)} df_0 dQ \\
& - \frac{2\pi Q(1 + 4Q^2)}{1 + 2Q^2} dt df_0 + \frac{2\pi f_0(1 - 2Q^2)}{(1 + 2Q^2)^2} dt dQ. \quad (4.41)
\end{aligned}$$

Using this metric allows us to specify a single threshold that simultaneously covers variations in f_0, Q , and t . By using the 3D coincidence test, we recover the same number of signal triggers, compared to S4 coincident test, while reducing the level of false triggers. Simulation experiments were used to set the coincidence threshold at $ds^2 = 0.4$.

At this stage of the coincident search pipeline we also veto triggers occurring during times when data quality flags were on. Data quality flags are intended to indicate periods of data taking which suffer from environmental and instrumental effects, inducing noise into the data [147, 148, 149]. We differentiate among three categories of environmental and instrumental vetoes: a) CAT1 -

Data marked as CAT1 indicate severe malfunctions of the detector. Data segments surviving the CAT1 veto are used in the analysis. b) CAT2 - Data marked as CAT2 indicate well-understood short duration noise transients. Data segments flagged by this category should not be used for upper limit calculations but are used for searching detection candidates. An example of a CAT2 flag is when simulated waveforms are present in the data in the form of “hardware injections”, which are made for calibration purposes. c) CAT3 - Data marked as CAT3 denote periods when the GW strain channel is only weakly correlated to environmental and instrumental artifacts. Detection candidates found at these times should be followed up with care.

4.4.2 Tuning the search

In any experiment, there will always be false triggers that mimic the behavior of signals. Typically, a detector’s false alarm rate due to the background can be determined simply by turning off the source or changing the orientation of the detector. However, these are not options for GW detectors, which are more or less omni-directional and cannot be shielded from gravitational waves. So, we estimate the background due to accidental coincidences of noise by shifting triggers in one detector relative to those in another by durations greater than the light-travel-time between those detectors. The shifts minimize the chance of putting an actual GW trigger in the background sample. We refer to these as background triggers or slide triggers, as opposed to the in-time coincident triggers (i.e., zero-lag triggers or foreground triggers) obtained without such time shifts. Background triggers corresponding to times which are flagged by

data quality studies are discarded. In LIGO S5 ringdown search, H2 data is not slid with respect to H1 data because the correlation of noise in these co-located detectors under-estimates the rate of false alarms [146]. However, we slide L1 data on a ring fifty times in steps of 5s and fifty times in steps of -5s, forming 100 experimental trials with no true signals [185, 134].

In order to test the sensitivity of our search to GWs from black holes, we add various simulated signals to the data stream. These are known as "software injections". We then run the search pipeline to find them in the noise. To measure the efficiency of the search we simulate three different populations of waveforms [146]. These include (a) PHENOM - phenomenologically motivated post-Newtonian inspiral-merger-ringdown (IMR) gravitational waveforms for binary black holes [152, 153, 154, 155, 156], (b) EOBNR - effective-one-body (EOB) post-Newtonian model fitted to numerical-relativity simulations [157, 158], and (c) RINGDOWN - quasi-normal modes of the perturbed black hole as discussed in Sec. 4.2.3. The injection parameters are chosen in such a way that they cover a wide range of signal parameter space. The injections are placed at random times within an interval of 300s distributed both uniformly in distance and in logarithmic distance between 1 Kpc and 1 Gpc and uniformly in initial phase, sky position, inclination and polarization angles.

We utilize the injection and the slide triggers to find a balance between recovering as many simulated signals in coincidence between multiple detectors as possible while keeping the rate of false coincidences to a minimum. This process is known as tuning a search pipeline. We finished tuning the LIGO S5 ringdown search recently. We find the SNR thresholds to be 5.5, 4.0, and 5.5 for

H1, H2, and L1 detectors, respectively, and the 3D coincidence threshold to be $ds^2 = 0.4$ for each detector. We found that the SNR thresholds for the LIGO S4 ringdown search were set at higher values (see Appendix D.1). This was one of the main reasons why no triple-coincident background trigger was found in H1, H2 and L1 detectors. It is also found that the number of slide triggers grows exponentially as the SNR threshold is lowered. So, to strike a balance between the computational cost and the detection efficiency, we only lowered the SNR threshold for the H2 detector. This is also motivated by the fact that the sensitivity of H2 detector is roughly half of the sensitivity of H1 or L1 detector.

We have not opened any boxes on the analysis yet. So, here we present some preliminary results from the tuning exercise. These results are produced using a portion of the LIGO S5 data. The results presented here contain only software injections and time-slides after CAT1, CAT2 and CAT3 vetoes have been applied. In Fig. 4.8, we show the sensitivity of the search pipeline to GWs from black holes by comparing made and found software injections in about 30 days of LIGO S5 data when H1, H2 and L1 detectors were operating in science mode. These plots include RINGDOWN as well as IMR (i.e., EOBNR and PHENOM) injections. Note that in the following plots, "Sim." means simulated parameters, and "Sngl." means estimated signal parameters. In Figs. 4.9 and 4.10, we separately study the PHENOM injections. Estimated effective distance is higher than simulated effective distance for a large number of IMR injections. We understand that the parameter estimation is bad for unequal mass binaries and the estimated ringdown mass is consistently higher than the simulated ringdown mass. And in Figs. 4.11, 4.12, and 4.14, we study the RINGDOWN injections.

We find bias in frequency recovery for higher mass black holes. Better mass recovery is found for signals with higher quality factor. This is because signals with higher quality factor have more cycles than signals with lower quality factor. The ringdown templates match earlier with the ringdown phase of the IMR signal, i.e, they match with the merger. Thus, effectively, they pick up a longer “ringdown” signal with a larger quality factor and lower frequency. We also find that inclusion of IMR waveforms improves detection efficiency. This is because the ringdown only signals at high frequency are more difficult to recover than those at low frequency because detector sensitivity decreases at higher frequencies. However, the inspiral and merger phases preceding the ringdown phase sweep up through the detector band, finding a significant match with ringdown templates.

The coincidence statistic is a ranking mechanism using the SNRs of coincident triggers. The exact form of the statistic for a given population depends on the properties of the SNR distributions of simulated and background signals (see Figs. 4.14, 4.15, and 4.16). In the LIGO S4 ringdown search, no triple-coincident event was found. However, a ranking statistic was proposed, which was motivated by Gaussian distribution of triggers, and is given by [133]

$$\rho_{D,S4} = \sqrt{\rho_{H1}^2 + \rho_{H2}^2 + \rho_{L1}^2}. \quad (4.42)$$

Note that the original equation in Ref. [133] does not have the square root and was named the detection statistic there. This was done in order to enhance the likelihood of ranking the triple-coincident (injection) triggers higher than the

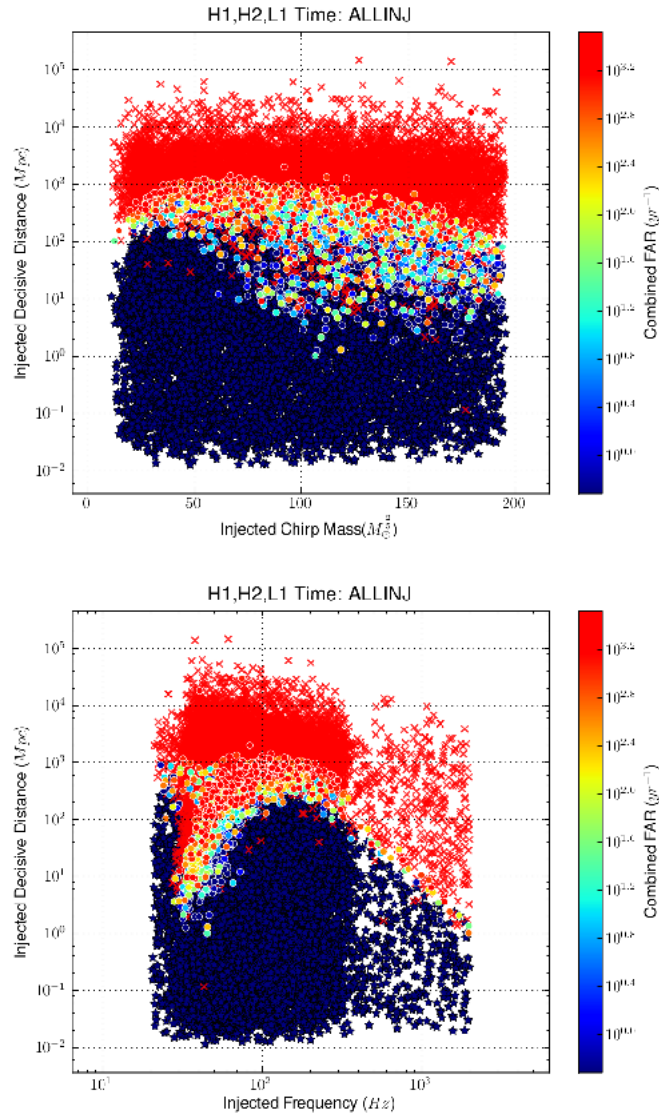


Figure 4.8: Decisive distance of missed and found injections is plotted against chirp mass (top) and frequency (bottom). The stars are injections found with zero combined false-alarm rate (FAR), and the circles are injections found with non-zero combined FAR. The red crosses are missed injections (vetoed injections are excluded). Note that the decisive distance is the second smallest effective distance. Chirp mass is defined in Sec. 5.2.1.

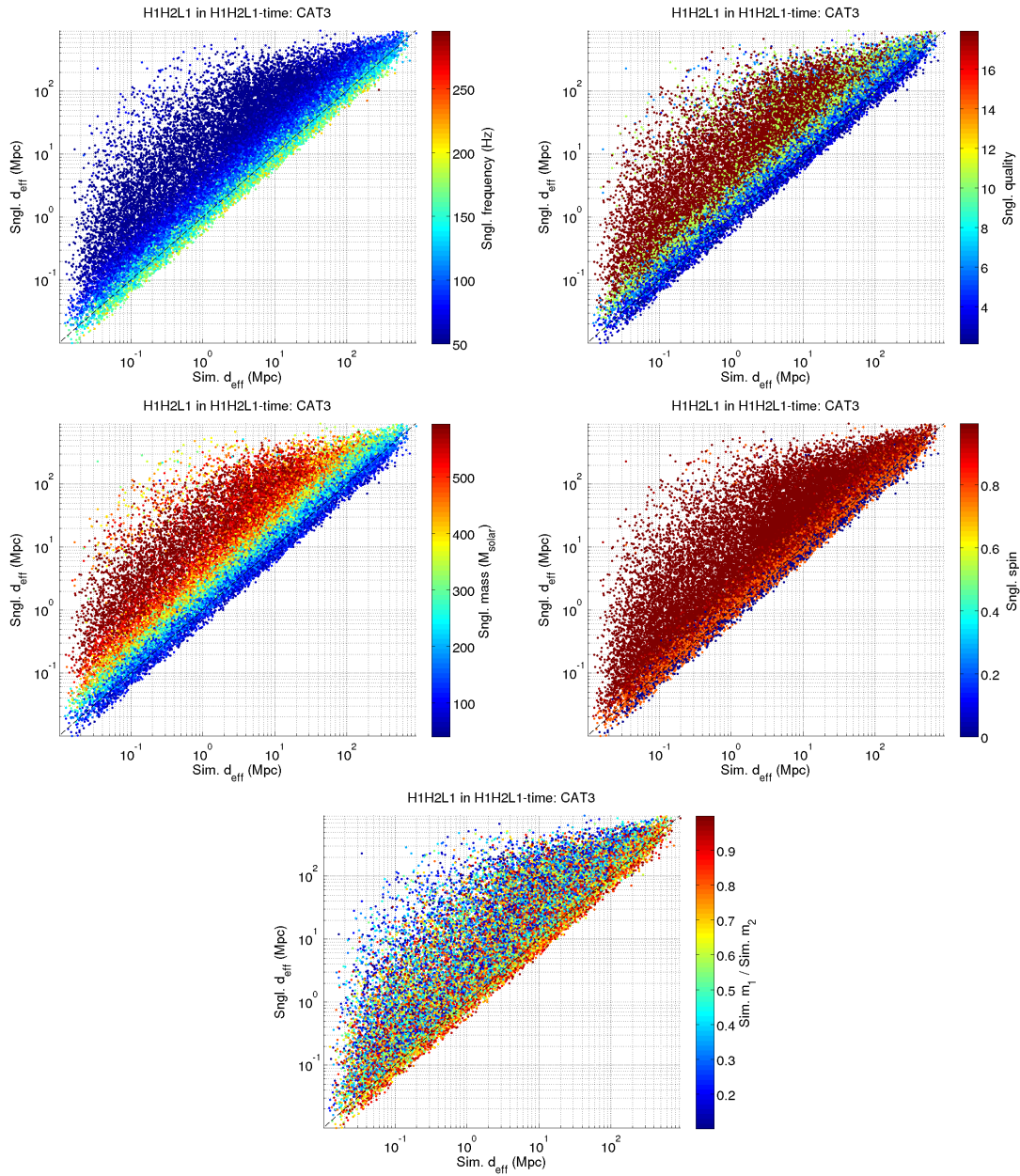


Figure 4.9: Scatter plots of simulated and estimated effective distance of found PHENOM injections. The color-bar represents estimated frequency (top left), quality factor (top right), mass (middle left), and spin (middle right). The color-bar of the bottom plot represents simulated mass-ratio. These parameters are estimated in H1 detector.

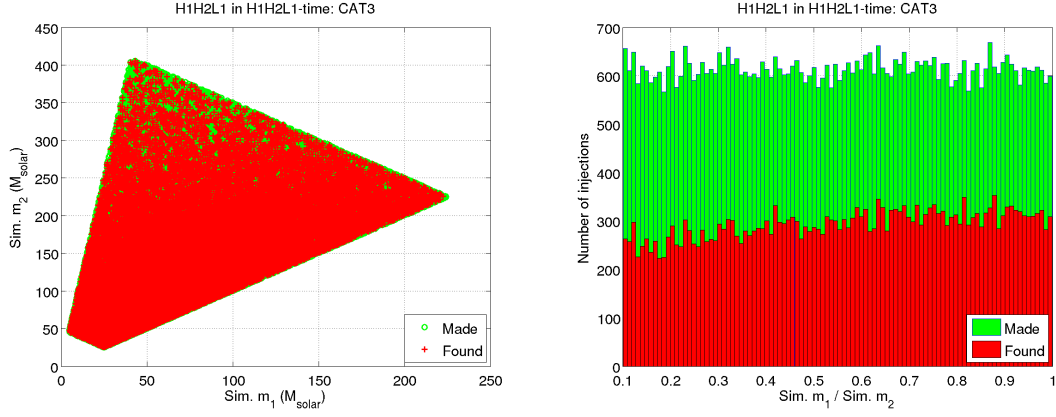


Figure 4.10: Scatter plots of simulated mass 2 versus mass 1 of made and found PHENOM injections (left). Histogram of number of made PHENOM injections per mass-ratio bin is compared with histogram of number of found PHENOM injections per mass-ratio bin (right).

double-coincident ones; the double coincident statistic was introduced as

$$\rho_{DS} = \min\{\rho_{ifo1} + \rho_{ifo2}, 2\rho_{ifo1} + 2.2, 2\rho_{ifo2} + 2.2\}. \quad (4.43)$$

The optimal statistic is the sum of SNR squares if the distribution is Gaussian. However, the distribution in real data was found to have long "tails", i.e. coincidences with a very loud SNR in one detector and a much lower SNR in the other, which motivated the form in Eq. (4.43). For the LIGO S5 ringdown search, the distribution of double-coincident triggers follow the same distribution as in the LIGO S4 ringdown search. So, we use this statistic to rank double-coincident triggers. However, by lowering the SNR threshold and with better understanding of systematics, sources and the pipeline, we managed to generate hundreds of triple-coincident background triggers. Their SNR distributions are shown in

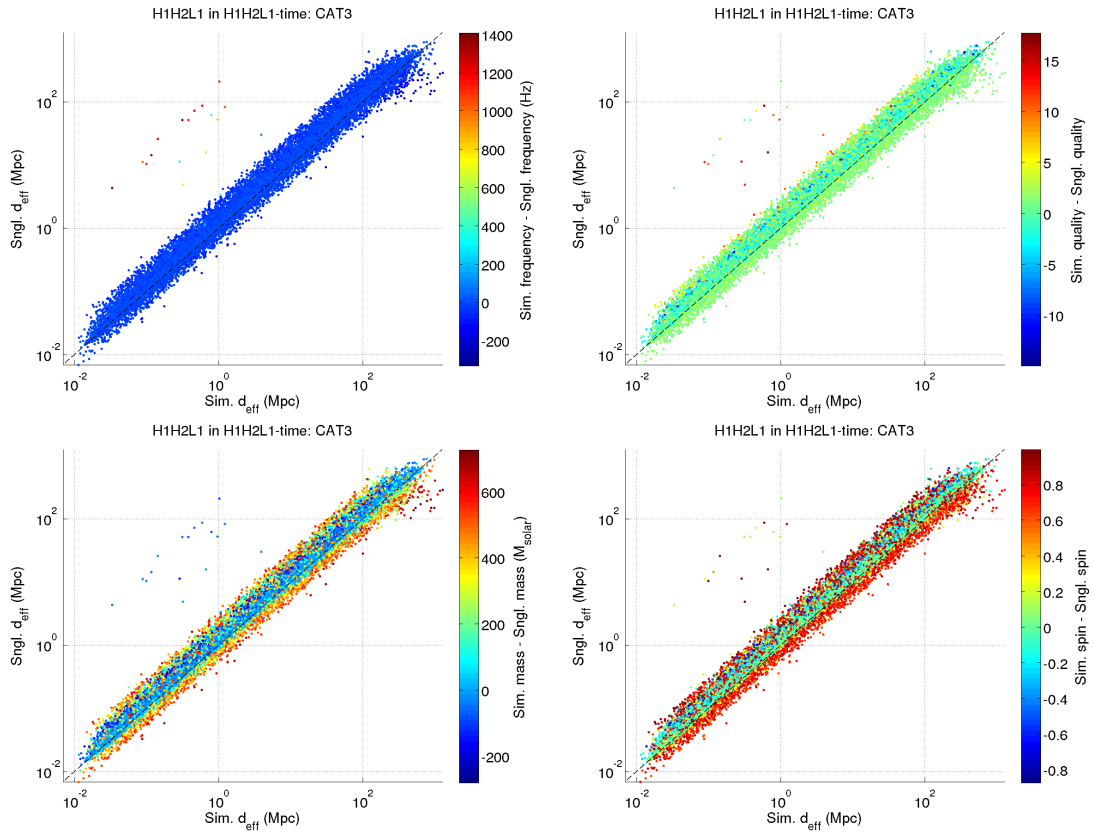


Figure 4.11: Scatter plots of simulated and estimated effective distance of found RINGDOWN injections. The color-bar represents difference between simulated and estimated parameters: Frequency (top left), quality factor (top right), mass (bottom left), and spin (bottom right). These parameters are estimated in H1 detector.

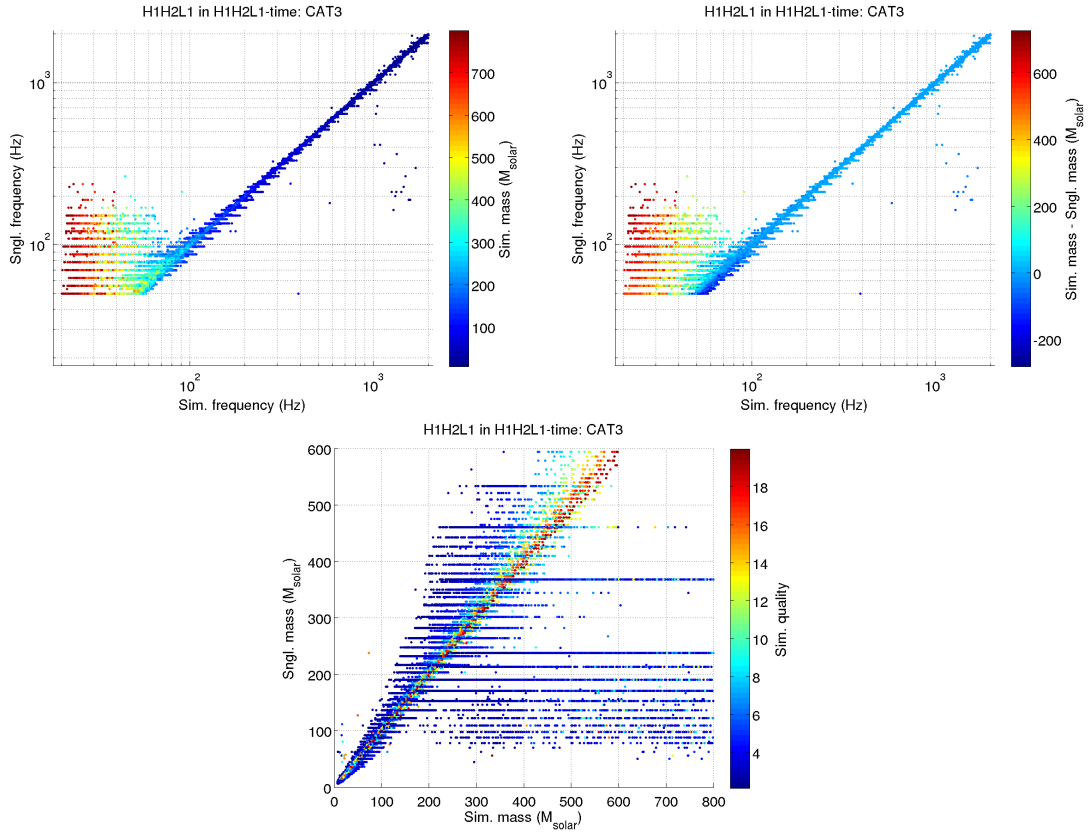


Figure 4.12: Scatter plots of simulated and estimated frequency of found RINGDOWN injections. The color-bar represents simulated mass (top left) and difference between simulated and estimated mass (top right). The scatter plots of simulated and estimated mass of found RINGDOWN injections (bottom). Here, the color-bar represents simulated quality factor. These parameters are estimated in H1 detector.

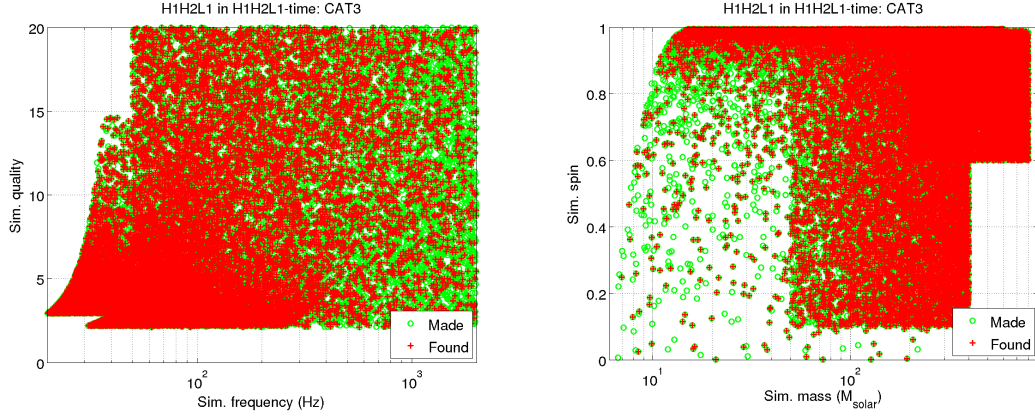


Figure 4.13: Scatter plots of simulated quality factor and frequency (left), and spin and mass (right) of made and found RINGDOWN injections.

Figs. 4.14 and 4.16, along with the injection distributions in Figs. 4.15, and 4.16. We find the background triggers tend to tail along L1 SNR. Since we do not have any signal-based veto for this pipeline, we down-weight triggers in the tail of one IFO significantly. This was done by defining a new triple-coincidence ranking statistic (see Fig. 4.16):

$$\rho_{\text{TR}} = \left[\min \left\{ \sqrt{\rho_{\text{H1}}^2 + \rho_{\text{H2}}^2 + \rho_{\text{L1}}^2}, \rho_{\text{H1}} + \rho_{\text{H2}} + 0.75, \right. \right. \\ \left. \left. \rho_{\text{H1}} + \rho_{\text{L1}} + 0.75, \rho_{\text{H2}} + \rho_{\text{L1}} + 0.75 \right\} \right] \Big|_{\rho_{\text{H1}}/\rho_{\text{H2}} > 1}. \quad (4.44)$$

This new triple-coincidence ranking statistic is compared with the old triple-coincidence ranking statistic in Fig. 4.17. There are hundreds of injection triggers which become louder than the loudest background trigger in this new ranking statistic, that otherwise would not have been achieved. This shows significant improvement in detection efficiency. More quantitatively, the detection probability of this new statistic is higher than that of the old statistic at low false-alarm

probability (see Fig. 4.18).

4.5 The coherent multi-detector search

A study performed on data from LIGO S4 science run shows that the Coherent WaveBurst (cWB) search is more sensitive to ringdown signals than the ringdown search. Note that the cWB pipeline is designed to search for unmodeled burst signals [151]. We understand that this gap in performance is due to the fact that the templated ringdown search described above did not have the infrastructure for checking the coherence of signals from a common astrophysical source in multiple detectors. To improve this scenario we implement several consistency checks. For example, we check for consistency of signal amplitudes and phases in the different detectors with their different orientations and with the signal arrival times in them. In the following sections, we discuss the utilities for the coherent stage, namely the coherent SNR and null-stream statistic, of the ringdown pipeline.

4.5.1 Elliptically-polarized ringdown template

Traditionally, the coincidence search pipeline has not searched for the initial phase of the ringdown signal. In other words, it uses only single-phase ringdown templates (see Eq. 4.26) to filter the data. However, this makes the pipeline limited from having enough information to check for signal amplitude and phase consistency across the detectors. A convenient way to search for the unknown phase of a signal is to filter the data with both phases of the template

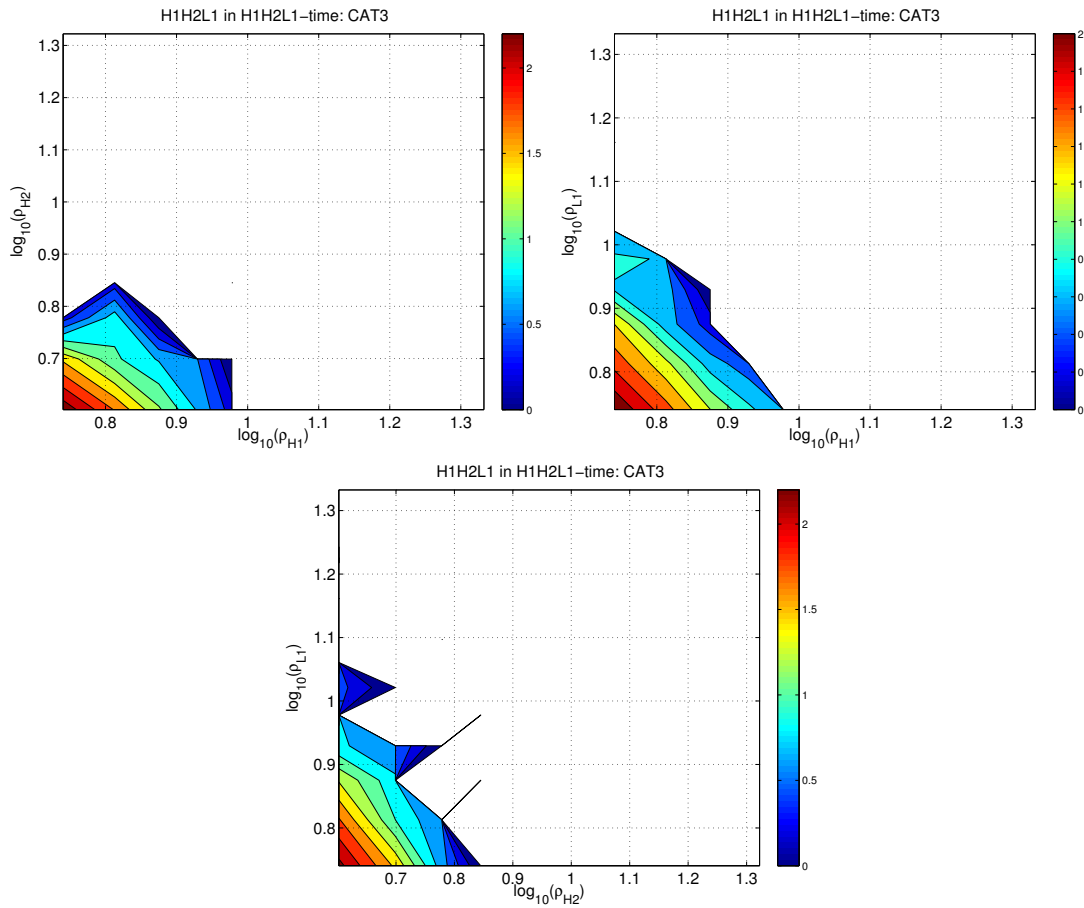


Figure 4.14: Contour plots of H2 SNR versus H1 SNR (top left), L1 SNR versus H1 SNR (top right), and L1 SNR versus H2 SNR (bottom) for triple coincident time-slide events. The color-bar represents $\log_{10}(N)$, where N is the number of triggers.

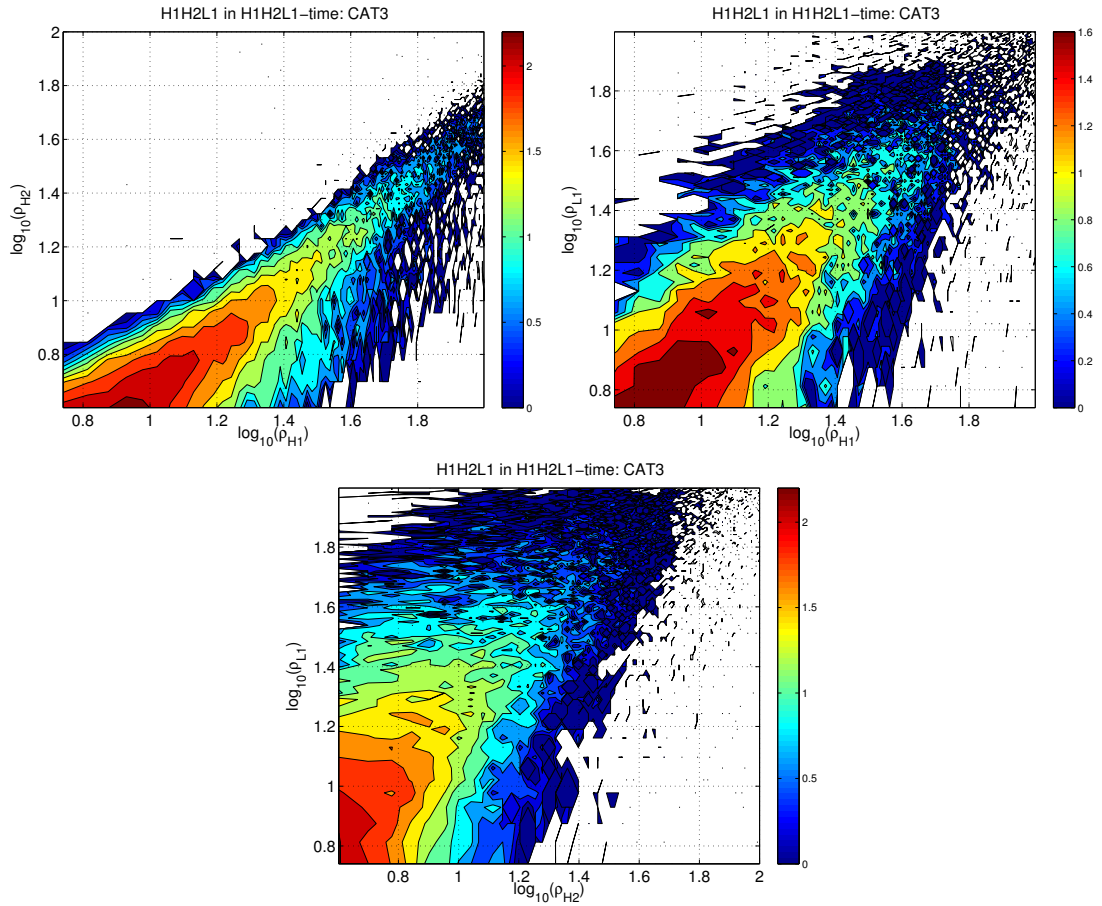


Figure 4.15: Contour plots of H2 SNR versus H1 SNR (top left), L1 SNR versus H1 SNR (top right), and L1 SNR versus H2 SNR (bottom) for triple coincident injection events. The color-bar represents $\log_{10}(N)$, where N is the number of triggers.

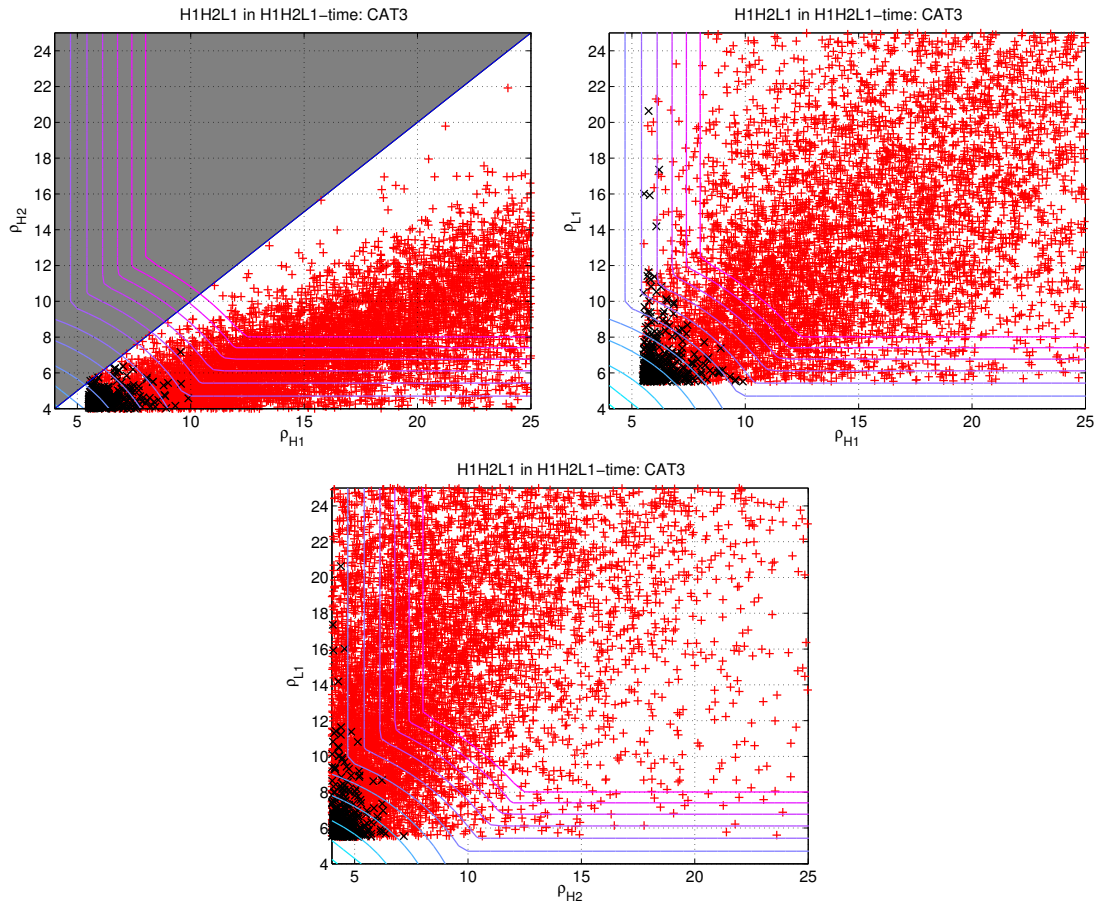


Figure 4.16: The H1-H2 (top left), H1-L1 (top right), and H2-L1 (bottom) SNR distributions for time-slide (black crosses) and injection triggers (red pluses). The curves represent the contours of constant values of the new triple-coincidence ranking statistic defined in Eq. 4.44.

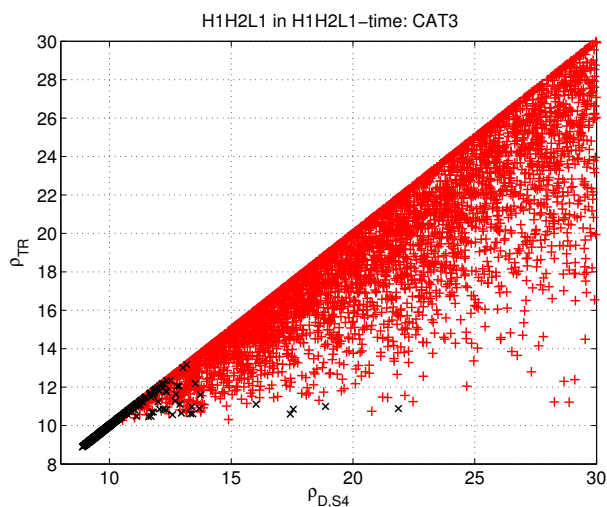


Figure 4.17: Scatter plots of the old and new triple-coincidence ranking statistics. Time-slide triggers are represented by the black crosses and injection triggers are represented by the red pluses.

separately [47]. This straightforwardly applies to the frequency domain inspiral signal in the stationary phase approximation [185]. This is because the sine and the cosine phases of the inspiral template are exactly orthogonal. But this is not true for a generic damped sinusoid. In the following sections, we justify this statement.

4.5.1.1 Fourier transformation of a generic decaying sinusoid

In general, a decaying sinusoid can be expressed as a real function

$$x(t) = A e^{-\alpha t} \cos(\omega t - \varphi) u(t) \quad (0 \leq t \leq \infty), \quad (4.45)$$

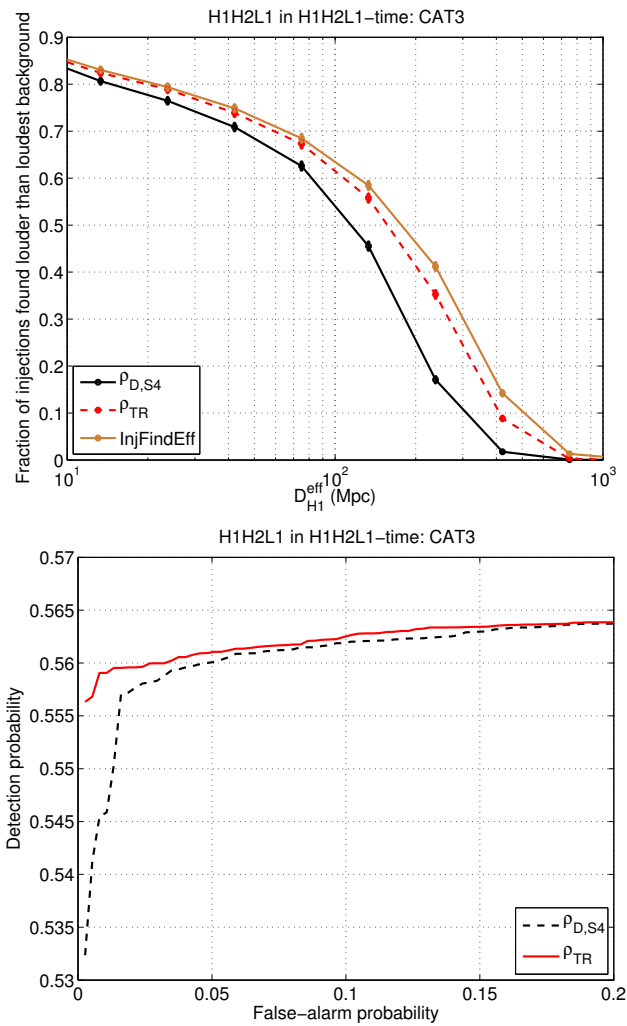


Figure 4.18: The efficiency of finding injections using the old triple-coincidence ranking statistic is compared with that of using the new triple-coincidence ranking statistic (top). The maximum achievable efficiency, for the injections considered here, is shown in "InjFindEff". In this case, we assume that all found injections are louder than the loudest background. The ROC curve of the old triple-coincidence ranking statistic is compared with the ROC curve of the new triple-coincidence ranking statistic (bottom).

where $u(t)$ is the Heaviside step function

$$u(t) = \begin{cases} 1 & \text{for } t \geq 0. \\ 0 & \text{otherwise.} \end{cases} \quad (4.46)$$

Let us define a complex function

$$z(t) = A e^{-\alpha t} e^{i(\omega t - \varphi)} u(t) \quad (4.47)$$

such that $x(t)$ is the real part of $z(t)$. The Fourier transformation of $z(t)$ is given by

$$\tilde{z}(f) = \int_{-\infty}^{\infty} z(t) e^{-2\pi i f t} dt \quad (4.48)$$

$$= \frac{A e^{-i\varphi}}{\alpha + i(2\pi f - \omega)}, \quad (4.49)$$

and hence,

$$\tilde{z}^*(-f) = \frac{A e^{i\varphi}}{\alpha + i(2\pi f + \omega)}. \quad (4.50)$$

Now, the Fourier transform of the real part of $z(t)$ is given by

$$\tilde{x}(f) = \frac{1}{2} [\tilde{z}^*(-f) + \tilde{z}(f)] \quad (4.51)$$

$$= \frac{A}{2} \left[\frac{e^{i\varphi} [\alpha + i(2\pi f - \omega)] + e^{-i\varphi} [\alpha + i(2\pi f + \omega)]}{\alpha^2 + 4i\pi f\alpha - 4\pi^2 f^2 + \omega^2} \right]. \quad (4.52)$$

In the next section, we show how the above relations are used to get the Fourier transform of an elliptically-polarized ringdown template.

4.5.1.2 Fourier transformation of an elliptically-polarized ringdown template

The elliptically-polarized ringdown template is expressed as

$$h_{\text{ep}}(t) = h_{\text{c}}(t) - i h_{\text{s}}(t), \quad (4.53)$$

where $h_c(t)$ and $h_s(t)$ are two damped sinusoid functions given by

$$h_c(t) = e^{-\pi f_0 t/Q} \cos(2\pi f_0 t), \quad (4.54)$$

$$h_s(t) = e^{-\pi f_0 t/Q} \sin(2\pi f_0 t). \quad (4.55)$$

The real part of $h_{\text{ep}}(t)$ can be found from Eq. (4.45) by setting $A = 1$, $\alpha = \pi f_0/Q$, $\omega = 2\pi f_0$ and $\varphi = 0$. Hence, the Fourier transformation of $h_c(t)$ is found Eq. (4.52), and is given by

$$\tilde{h}_c(f) = \frac{\frac{\pi f_0}{Q} + i2\pi f}{4\pi^2 f_0^2 - 4\pi^2 f^2 + \frac{\pi^2 f_0^2}{Q^2} + i\frac{4\pi^2 f f_0}{Q}}. \quad (4.56)$$

Similarly, the imaginary part of $h_{\text{ep}}(t)$ is found from Eq. (4.45) by setting $A = 1$, $\alpha = \pi f_0/Q$, $\omega = 2\pi f_0$ and $\varphi = \pi/2$. Hence, the Fourier transform of $h_s(t)$ is found from Eq. (4.52), and is given by

$$\tilde{h}_s(f) = \frac{2\pi f_0}{4\pi^2 f_0^2 - 4\pi^2 f^2 + \frac{\pi^2 f_0^2}{Q^2} + i\frac{4\pi^2 f f_0}{Q}}. \quad (4.57)$$

By combining Eqs. (4.56) and (4.57), one gets the Fourier transformation of $h_{\text{ep}}(t)$.

4.5.1.3 The template normalization

Filtering the data $x(t)$ with an elliptically-polarized template $h_{\text{ep}}(t; \mu_i)$ characterized by the source parameters μ_i yields the SNR statistic

$$\rho(h_{\text{ep}}) = \frac{|\langle x, h_{\text{ep}} \rangle|}{\sqrt{\langle h_{\text{ep}}, h_{\text{ep}} \rangle}}, \quad (4.58)$$

$$= \frac{|\langle x, \{h_c - ih_s\} \rangle|}{\sqrt{\langle h_{\text{ep}}, h_{\text{ep}} \rangle}}, \quad (4.59)$$

$$= \frac{\sqrt{\langle x, h_c \rangle^2 + \langle x, h_s \rangle^2}}{\sqrt{\langle h_{\text{ep}}, h_{\text{ep}} \rangle}}. \quad (4.60)$$

Note that the noise-weighted scalar product introduced above is defined for the two vectors $X(t)$ and $Y(t)$ by

$$\langle X, Y \rangle \equiv 2 \int_{-\infty}^{\infty} df \frac{\tilde{X}(f)\tilde{Y}^*(f)}{\xi(|f|)}. \quad (4.61)$$

The detailed calculation for the template normalization is as follows:

$$\sigma_{\text{ep}}^2 = \langle h_{\text{ep}}, h_{\text{ep}} \rangle, \quad (4.62)$$

$$= \langle \{h_c - ih_s\}, \{h_c - ih_s\} \rangle, \quad (4.63)$$

$$= 2 \int_{-\infty}^{\infty} df \frac{[\tilde{h}_c(f) - i\tilde{h}_s(f)] [\tilde{h}_c^*(f) + i\tilde{h}_s^*(f)]}{\xi(|f|)}, \quad (4.64)$$

$$= 2 \int_{-\infty}^{\infty} df \frac{\tilde{h}_c(f)\tilde{h}_c^*(f)}{\xi(|f|)} + 2 \int_{-\infty}^{\infty} df \frac{\tilde{h}_s(f)\tilde{h}_s^*(f)}{\xi(|f|)} - 2i \int_{-\infty}^{\infty} df \frac{\tilde{h}_s(f)\tilde{h}_c^*(f)}{\xi(|f|)} + 2i \int_{-\infty}^{\infty} df \frac{\tilde{h}_c(f)\tilde{h}_s^*(f)}{\xi(|f|)}, \quad (4.65)$$

$$= 2 \int_{-\infty}^{\infty} df \frac{\tilde{h}_c(f)\tilde{h}_c^*(f)}{\xi(|f|)} + 2 \int_{-\infty}^{\infty} df \frac{\tilde{h}_s(f)\tilde{h}_s^*(f)}{\xi(|f|)}, \quad (4.66)$$

$$= \langle h_c, h_c \rangle + \langle h_s, h_s \rangle. \quad (4.67)$$

The justification for canceling the last two terms in Eq. (4.65) is numerically shown in Fig. 4.19. It is important to note that

$$\langle h_c, h_c \rangle \neq \langle h_s, h_s \rangle, \quad \text{for a range of } \mu_i. \quad (4.68)$$

This is because h_c and h_s are not orthogonal due to the damping factor. In the following section, we numerically justify this statement.

4.5.1.4 Numerical analysis

To discretize the elliptically-polarized template we consider N data points (assume N to be even) sampled over a given time. When one Fourier transforms a

function one seeks a discrete frequency array

$$f_k = \frac{k}{N\Delta t}; \quad k = -\frac{N}{2}, \dots, \frac{N}{2}, \quad (4.69)$$

where k is an integer and Δt is the inverse of the sampling frequency f_s , i.e., $\Delta t = 1/f_s$. We choose the sampling frequency 4096 Hz, with 256 data points. For simplicity, we consider noise to be white Gaussian, and set its power spectrum, which is constant, to unity, i.e., $\xi(|f|) = 1$. In Fig. 4.19 we consider an elliptically-polarized template characterized by the central frequency $f_0 = 1200$ Hz and the quality factor $Q = 4$. We plot the integrands of the last two terms of Eq. (4.65) as functions of frequency: The top left panel represents their real parts and the top right panel represents their imaginary parts. Their sum (integration) over the frequencies is also noted. So, the last two terms of Eq. (4.65) together contribute zero (except for negligible numerical errors) in the template norm expression. In the bottom panel, we plot and compare the integrands of the first two terms of Eq. (4.65). It proves that the first two terms are not equal.

We now consider a bank of templates that includes both sine and cosine phases and characterized by a range of central frequencies $f_0 \in [50 - 2000]$ Hz and quality factors $Q \in [2.1187 - 20]$. For each template, we define a quantity called “fractional difference” as

$$\text{Fractional difference} \equiv \frac{\langle h_s, h_s \rangle - \langle h_c, h_c \rangle}{\langle h_c, h_c \rangle}. \quad (4.70)$$

Figure 4.20 shows the contours of the fractional difference in the template parameter space. For higher central frequencies and lower quality factors, the fractional difference is significant. Therefore, in order to coherently search for

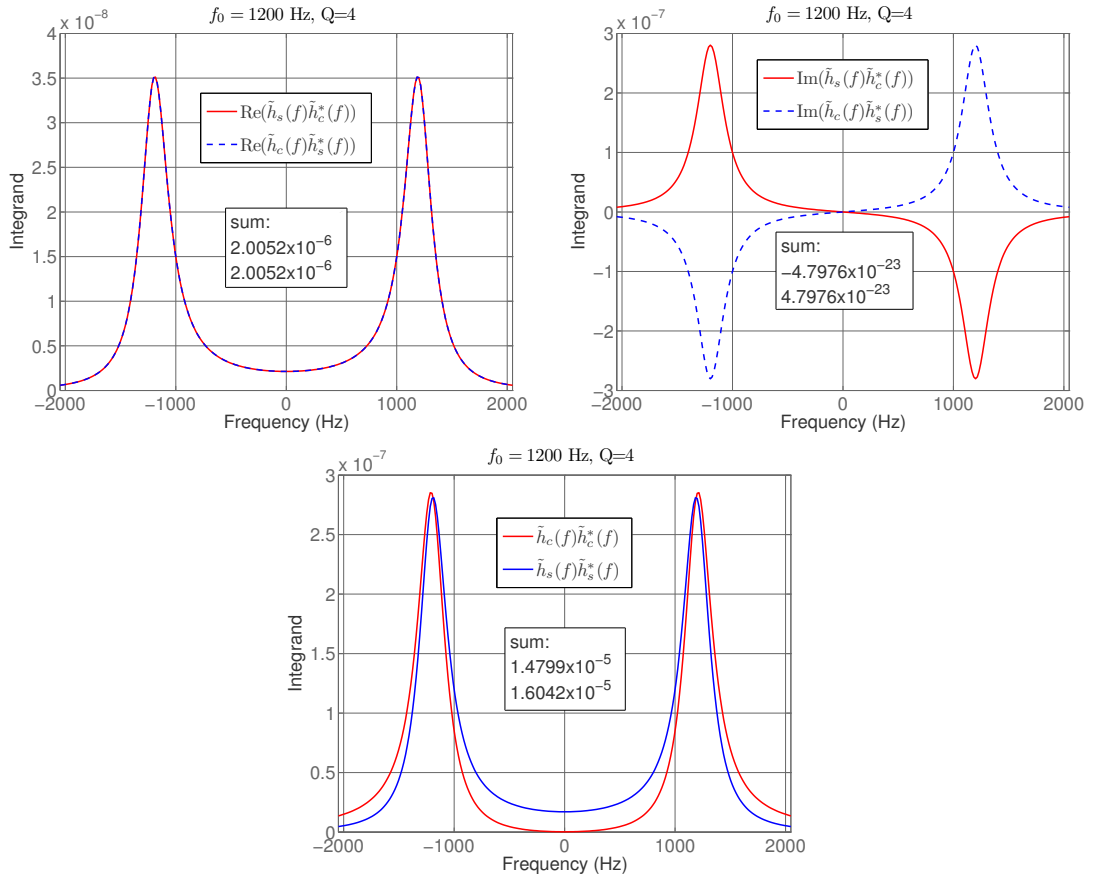


Figure 4.19: The integrands of the sine and cosine template variances (Eq. (4.65)) are plotted as functions of frequency for a given point in the parameter space. Here, the frequency plotted in the x -axes is meant to be the frequency f_k defined in Eq. (4.69). The top left and the top right panels depict the frequency behavior of the last two terms in expression (4.65), whereas the bottom panel depicts the same aspect of the first two terms in that expression.

ringdown signals in a network of detectors, it is necessary to model the template by incorporating both phases.

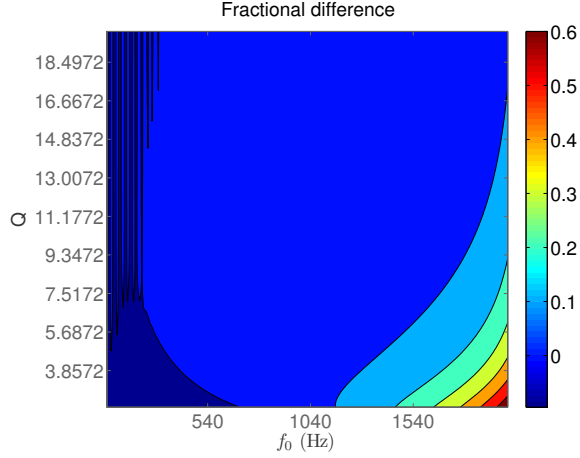


Figure 4.20: Contours of the fractional difference of sine and cosine phases of the elliptically-polarized ringdown template. The color bar represents the fractional difference as defined in Eq. (4.70).

4.5.1.5 SNR statistic

The coherent stage (see Fig. 4.3) follows up on triggers that survive the coincident stage by computing their coherent and null-stream statistics. We construct small snippets of C-data around the peak-time of every trigger that is found to be coincident in multiple detectors in a network. The detailed prescription is given in the next chapter. However, this construction is done by filtering the data around the trigger peak-time with elliptically-polarized templates from the ringdown template bank, and the SNR is given by

$$\rho_{\text{ep}}(h_{\text{ep}}) = \frac{|\langle x, h_{\text{ep}} \rangle|}{\sqrt{\langle h_{\text{ep}}, h_{\text{ep}} \rangle}} \equiv \frac{|Z_{\text{ep}}|}{\sigma_{\text{ep}}}. \quad (4.71)$$

Following the same procedure as in Sec. 4.4.1.3, we find

$$|Z_{epj}| = \frac{2}{N\Delta t} \left[\left(\Re \left\{ \sum_{k=1}^{N/2-1} \frac{S_v^{-1}}{dyn R} (\Delta t \tilde{x}_k^*) (\Delta t \tilde{h}_{ck}) e^{-i2\pi jk/N} \right\} \right)^2 \right. \quad (4.72)$$

$$\left. + \left(\Re \left\{ \sum_{k=1}^{N/2-1} \frac{S_v^{-1}}{dyn R} (\Delta t \tilde{x}_k^*) (\Delta t \tilde{h}_{sk}) e^{-i2\pi jk/N} \right\} \right)^2 \right]^{1/2}, \quad (4.73)$$

and the template variance is given by

$$\sigma_{ep}^2 = \frac{4}{N\Delta t} \left(\sum_{k=1}^{N/2-1} \frac{S_v^{-1}}{dyn^2 |R|^2} \left[(\Re \{ \Delta t \tilde{h}_{ck} \})^2 + (\Im \{ \Delta t \tilde{h}_{ck} \})^2 \right] \right. \quad (4.74)$$

$$\left. + \sum_{k=1}^{N/2-1} \frac{S_v^{-1}}{dyn^2 |R|^2} \left[(\Re \{ \Delta t \tilde{h}_{sk} \})^2 + (\Im \{ \Delta t \tilde{h}_{sk} \})^2 \right] \right) dyn^2. \quad (4.75)$$

The SNR-threshold procedure introduced in Sec. 4.4.1.3 is also followed here, but with the quantities defined in terms of Z_{ep} , ρ_{ep} , and σ_{ep} .

4.5.2 Coherent statistics

In this section we briefly outline the basic expressions for the coherent SNR and the null-stream statistics for use in the ringdown search pipeline. We postpone the more detailed discussion of those statistics (see, e.g., Eqs. (5.31) and (5.39)) to the next chapter. Specifically, we focus on three cases of detector networks most relevant to the S5 coherent ringdown searches:

Case-1: Two co-aligned detectors with different noise PSDs.

The coherent SNR for two co-aligned detectors with different noise power spectral density is given by

$$\varrho_{12} = \frac{|C_1 \sigma_1 + C_2 \sigma_2|}{\sqrt{(\sigma_1)^2 + (\sigma_2)^2}}, \quad (4.76)$$

where σ_I is the template-norm

$$\sigma_I \equiv \sigma_{\text{ep}I} = \sqrt{\langle h_{\text{ep}I}, h_{\text{ep}I} \rangle}, \quad (4.77)$$

and

$$C_I \equiv \rho_I e^{i\Phi_I} = \frac{\langle x_I, h_{\text{ep}I} \rangle}{\sigma_{\text{ep}I}}, \quad (4.78)$$

is the matched-filter output against an elliptically-polarized template in the I th detector. The null-stream statistic is given by

$$\eta_{12} = \frac{\left| \frac{C_1}{\sigma_1} - \frac{C_2}{\sigma_2} \right|}{\sqrt{\left(\frac{1}{\sigma_1}\right)^2 + \left(\frac{1}{\sigma_2}\right)^2}}. \quad (4.79)$$

Case-2: Three detectors with two of them coaligned and colocated at one site and the third one located at a second site, and all with different noise PSDs.

Let detectors $I = 1, 2$ be at the same site. The coherent SNR for this network is given by

$$\varrho_{123} = \sqrt{(\varrho_{12})^2 + (\rho_3)^2}. \quad (4.80)$$

And the null-stream η_{123} is the same as the null-stream defined for Case-1.

Case-3: Three detectors at different sites with different orientations and noise PSDs.

The antenna response functions are expressed as

$$\begin{pmatrix} F_+ \\ F_\times \end{pmatrix} = \begin{pmatrix} \cos 2\psi & \sin 2\psi \\ -\sin 2\psi & \cos 2\psi \end{pmatrix} \begin{pmatrix} u \\ v \end{pmatrix}, \quad (4.81)$$

with $u(\theta, \phi)$ and $v(\theta, \phi)$ being detector orientation (and source-location) dependent functions. For a network of three detectors, we introduce the following

shorthand notations for the quantities involving these functions:

$$\mathcal{A}_{12} \equiv (u_1 v_2 - u_2 v_1), \quad (4.82)$$

$$\mathcal{A}_{23} \equiv (u_2 v_3 - u_3 v_2), \quad (4.83)$$

$$\mathcal{A}_{31} \equiv (u_3 v_1 - u_1 v_3), \quad (4.84)$$

where, u_I and v_I are the I th detector orientation-dependent functions. We also define $\mathcal{A}_{ij} = -\mathcal{A}_{ji}$. Then the coherent and null-stream statistics for this network are given by

$$\rho_{123} = \sqrt{\frac{|\mathcal{B}_{12}C_1 + \mathcal{B}_{32}C_3|^2 + |\mathcal{B}_{31}C_3 + \mathcal{B}_{21}C_2|^2 + |\mathcal{B}_{23}C_2 + \mathcal{B}_{13}C_1|^2}{(\mathcal{B}_{12})^2 + (\mathcal{B}_{23})^2 + (\mathcal{B}_{31})^2}}, \quad (4.85)$$

and

$$\eta_{123} = \sqrt{\frac{\left| \frac{C_1}{\mathcal{B}_{12}} - \frac{C_3}{\mathcal{B}_{32}} \right|^2 + \left| \frac{C_3}{\mathcal{B}_{31}} - \frac{C_2}{\mathcal{B}_{21}} \right|^2 + \left| \frac{C_2}{\mathcal{B}_{23}} - \frac{C_1}{\mathcal{B}_{13}} \right|^2}{\left(\frac{1}{\mathcal{B}_{12}} \right)^2 + \left(\frac{1}{\mathcal{B}_{23}} \right)^2 + \left(\frac{1}{\mathcal{B}_{31}} \right)^2}}, \quad (4.86)$$

where

$$\mathcal{B}_{12} \equiv \mathcal{A}_{12} \sigma_1 \sigma_2, \quad (4.87)$$

$$\mathcal{B}_{23} \equiv \mathcal{A}_{23} \sigma_2 \sigma_3, \quad (4.88)$$

$$\mathcal{B}_{31} \equiv \mathcal{A}_{31} \sigma_3 \sigma_1, \quad (4.89)$$

are the shorthand notations for the quantities involving detector orientation, source-location, and template normalization. Like \mathcal{A}_{ij} , we also have $\mathcal{B}_{ij} = -\mathcal{B}_{ji}$.

4.5.3 Performance study

The coherent stage for the LIGO-VIRGO S5/S6 ringdown search is in the process of tuning, and the results discussed here are preliminary and may change. So, we do not present them here. However, there is preliminary evidence that the coherent statistic performs better than the coincident statistic. To study the utility of the coherent statistics, we ran the ringdown search pipeline (see Fig. 4.3) on a month of data from LIGO S4 science run. For this example, we consider only H1 and H2 detectors. A total of 225 simulated ringdown signals were injected into the data, of which 86 were found by the pipeline. The injection finding efficiency is low because most of the injections were too weak. A total of 143 background triggers, obtained through time-slide experiments, were found. Figure 4.21 scatter plots the coincident statistic (bitten-L) against the coherent statistic (effective-coherent SNR) for the found injection and the slide triggers. The effective-coherent SNR defined here is the quadrature sum of the coherent SNR and null-stream. The curved lines in the top panel of Fig. 4.21 represent constant effective-coherent SNR values. In Fig. 4.22, we compare the efficiency of finding injection triggers using the coincidence statistic with the coherent statistic. Note that both the amplitude and phase consistency are applied in this analysis. In Fig. 4.23 we plot and compare the ROC (receiver operative characteristic, see Ref. [26]) curve for these two statistics. We find that the coherent statistic performs better than the coincidence statistic in the low false-alarm regime.

4.6 Discussion

We have demonstrated using simulated signals that the ringdown pipeline is an efficient search pipeline for detecting gravitational waves from perturbed black holes. As discussed above, we also show that the added-coherent-stage ringdown pipeline performs better than the coincidence-only ringdown pipeline. We expect its performance to be boosted for triple-site searches (LIGO-VIRGO S6 ringdown search). It is decided to use multivariate statistical classifier (MVSC) as a detection statistic for the LIGO-VIRGO S5/S6 ringdown searches [146]. It is an implementation of the random forest of bagged decision trees algorithm. MVSC combines information from many statistics. So, the amalgamated information should be better than any individual statistic alone. MVSC's performance is the best for a best set of parameters that best separate background from signals. The effective-coherent SNR and the new triple-coincidence ranking statistic are found to be the members of the best set of MVSC's parameters.

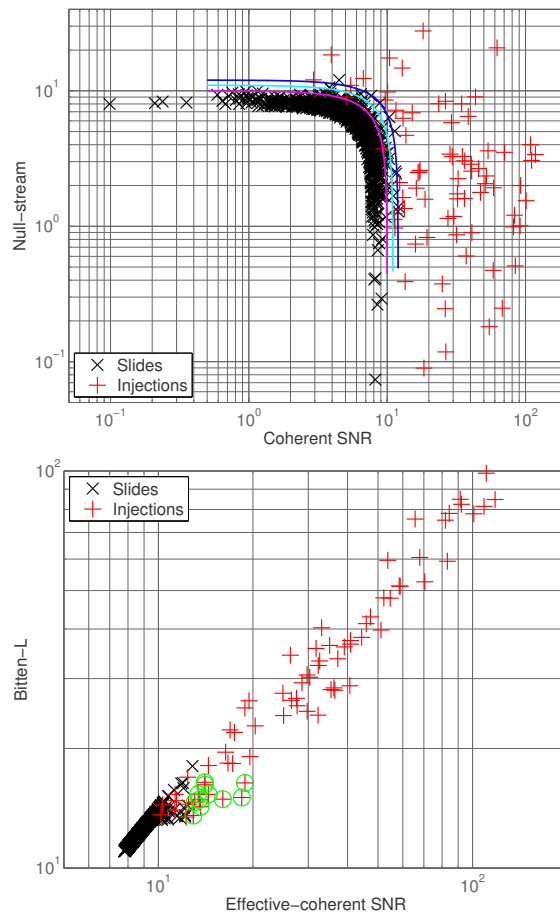


Figure 4.21: The scatter plots for the null-stream and coherent SNR (top panel), and the chopped-L and effective-coherent SNR (bottom panel). The injection triggers are denoted by red pluses, and the background triggers (slide triggers) are denoted by black crosses. All background triggers have been retained. The curved lines in the top figure are the contours of constant effective-coherent SNR, which is a combination of the null-stream and coherent SNR. There are 10 found injection triggers, marked by green circles, which are quieter than the loudest background in the coincidence search whereas louder than the loudest background in the coherent search.

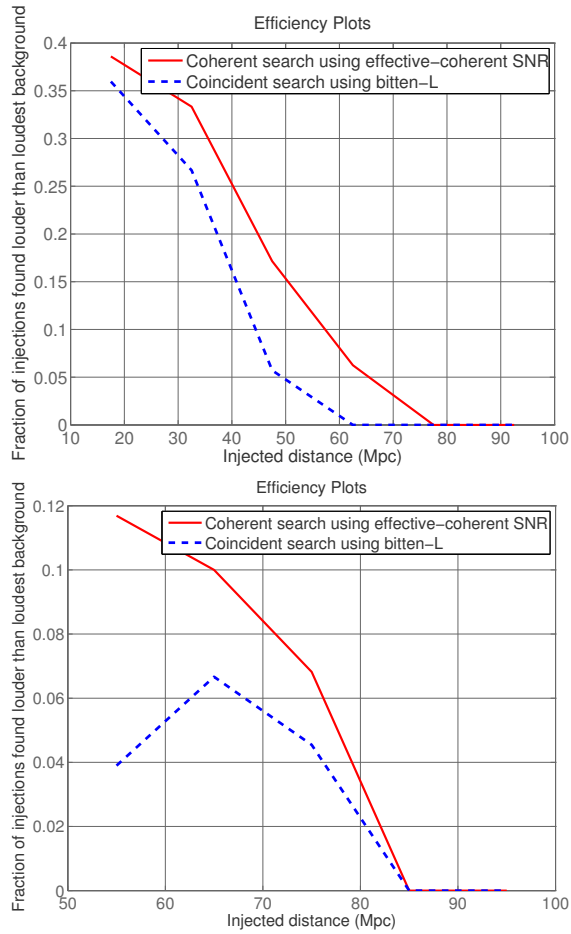


Figure 4.22: Here we compare the efficiency of finding signals using the coincidence search with that of using the coherent search. In the top panel, we focus on a set of stronger injections, with distance from 10 Mpc to 100 Mpc. In the bottom panel, a similar study was performed but with weaker signals, i.e, injections were made allowing distance from 50 Mpc to 100 Mpc. The overall performance of the coherent search is quite a bit better than the coincidence search. In the last distance bin, from 85 Mpc to 100 Mpc, the coherent search above does not show any improvement over the coincidence search simply because no coincidence trigger was found in that bin.

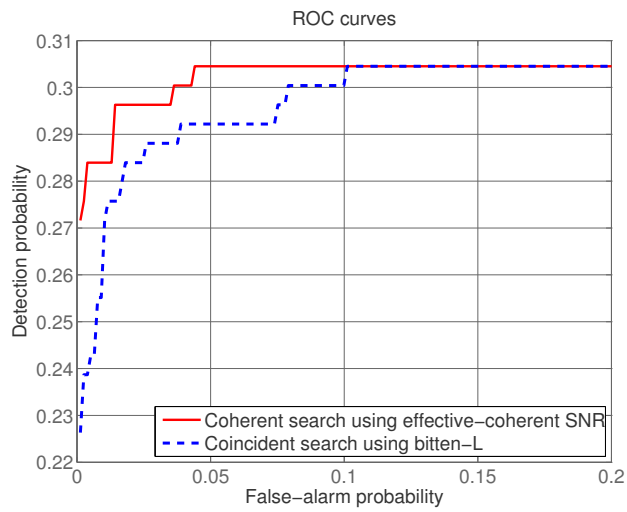


Figure 4.23: The ROC curve of the coincidence search is compared with the ROC curve of the coherent search. The overall performance of the coherent search is better than that of the coincident search. This is because there are 10 found injections that are weaker than the loudest background trigger in the coincidence search as shown in Fig. 4.21. In the low false-alarm region, detection probability of coherent search is higher than the coincident search.

Chapter 5

Aspects of a blind hierarchical coherent search for coalescing compact binaries

We describe a hierarchical data analysis pipeline for coherently searching for GW signals from non-spinning compact binary coalescences (CBCs) in the data of multiple earth-based detectors. This search assumes no prior information on the sky position of the source or the time of occurrence of its transient signals and, hence, is termed “blind”. The pipeline computes the coherent network search statistic that is optimal in stationary, Gaussian noise and more advanced than the current state-of-the-art approach, called coincident statistics. More importantly, it allows for the computation of a suite of alternative multi-detector coherent search statistics and signal-based discriminators that can improve the performance of CBC searches in real data, which can be both non-stationary

and non-Gaussian. Also, unlike the coincident multi-detector search statistics that have been employed so far, the coherent statistics are different in the sense that they check for the consistency of the signal amplitudes and phases in the different detectors with their different orientations and with the signal arrival times in them. Since the computation of coherent statistics entails searching in the sky, it is more expensive than that of the coincident statistics that do not require it. To reduce computational costs, the first stage of the hierarchical pipeline constructs coincidences of triggers from the multiple interferometers, by requiring their proximity in time and component masses. The second stage follows up on these coincident triggers by computing the coherent statistics. Here, we compare the performances of this hierarchical pipeline with and without the second (or coherent) stage in Gaussian noise. Whereas introducing hierarchy can be expected to cause some degradation in the detection efficiency compared to that of a single-stage coherent pipeline, nevertheless it improves the computational speed of the search considerably. The two main results of this work are: (1) The performance of the hierarchical coherent pipeline on Gaussian data is shown to be better than the pipeline with just the coincident stage. (2) The three-site network of LIGO detectors, in Hanford and Livingston (USA), and VIRGO detector in Cascina (Italy) cannot resolve the polarization of waves arriving from certain parts of the sky. This can cause the three-site coherent statistic at those sky positions to become singular. Regularized versions of the statistic can avoid that problem, but can be expected to be sub-optimal. The aforementioned improvement in the pipeline's performance due to the coherent stage is true in spite of this handicap. This work (see Ref. [12]) was the result of a collaboration that in-

cluded two other graduate students, Thilina Dayanga and Shaon Ghosh, at the Washington State University.

5.1 Introduction

Signals from binaries of neutron stars and black holes (BHs) enjoy the prospect of being the first signals to be detected by GW detectors [159]. They are among the best understood of all GW sources and a large enough number of them are expected to appear in the data of second generation detectors [160]. The last several science runs at LIGO [161], GEO600 [162], and VIRGO [163] revealed that searches for signals from these compact binary coalescences (CBCs) benefit from the networking of multiple detectors because of the reduction in the rate of accidentals or false alarms, especially, from non-stationary and non-Gaussian noise artifacts. Further, studies with injection of simulated signals show that the estimation of source parameters, such as sky position and wave polarization, is also helped by networks involving detectors at three or more sites around the globe [41, 164, 165]. This is important since CBCs may not always emit electromagnetic signals that are strong enough to be observable.

This chapter describes blind CBC search strategies, which must be contrasted with a targeted search method [166]. An example of the latter case is a search for GW signal triggered by a short-duration gamma-ray burst (GRB). Short GRBs have been conjectured to be associated with NS-NS or NS-BH coalescences [167, 168]. Owing to an electromagnetic counterpart, the sky-position of the short GRB and the time of arrival of its gamma-ray signal are known in advance for

offline searches. This implies that searches for GW signals from these sources require three less parameters to scan, and are, therefore, computationally less expensive. (In reality, one searches over a several-second window around the arrival time of the gamma-ray signal because it is not clear yet how separated the emission of the gamma-ray burst and the binary-object merger are in time [169, 170].) Perhaps more significantly, it reduces the probability of false-alarms and, therefore, increases our detection confidence.

In this chapter, we address how one tackles both these issues, namely, of increased computational costs and false-alarm rates, affecting a blind search for signals from CBCs with non-spinning components. To reduce the excess computational cost arising from scanning the arrival time, one introduces hierarchical stages in the search pipeline, whereby, first, the triggers of interest are identified in the detectors individually. This is followed by recognizing triggers that are coincident in multiple detectors and then computing network-based statistics for them that reveal their significance as GW candidates. (These hierarchical steps were introduced in Ref. [171] and have been used in multiple CBC searches ever since.) The final stage is used to compute the coherent network statistics for these coincident triggers. To address the second problem of increased false-alarms, especially, from non-stationary noise transients, we introduce signal-based multi-detector discriminators that check for consistency of the signals appearing in individual detectors with a CBC source, after accounting for the different orientations of the detectors and the delays in their times of arrival in them.

Past experiments with multi-detector searches for gravitational-wave signals from CBCs have shown that the statistics that are optimal in Gaussian and sta-

tionary noise (OGSN) cease to be so in real data, in general [171, 172, 173]. Instead a function of the chi-square-weighted [174] matched-filter [175] outputs has been found to deliver a better performance [171, 172]. This function is arrived at empirically by comparing the distribution of the matched-filter and chi-square statistics for simulated CBC signal injections with that of the background. These statistics did not, however, use the phase of the matched-filter output to discriminate signals from noise, which a coherent statistic [46, 47] is equipped to do. We will call the former *coincident* statistics. Their construction has nevertheless helped inspire techniques for obtaining empirically an effective coherent statistic that performs better in real data than the coherent statistic of Refs. [46, 47]. It is this statistic and its variants, which can be useful in searching for non-spinning CBC signals in real data, that we discuss in detail in this chapter.

5.2 Multi-detector statistics

We begin by describing the statistic that is optimal for coherently searching for non-spinning CBC signals in data from multiple detectors when their noise is Gaussian and stationary. The first part of this section gives an alternative derivation of this statistic, as compared to that available in the literature [46]. In the process, it introduces notation and convention followed here. It also introduces signal parameters and variables used in the coherent search code available in the LIGO (Scientific Collaboration) Algorithm Library LAL [176]. We then compare that statistic with the aforementioned empirically-motivated multi-detector

coincident statistics, which have been applied in real data.

5.2.1 Signal and noise

Consider a non-spinning coalescing compact binary with component masses $m_{1,2}$, such that its total mass is $M = m_1 + m_2$ and its reduced mass is $\mu = m_1 m_2 / M$. In the restricted post-Newtonian approximation, the two polarizations determining the GW strain are:

$$h_+(t; r, M, \mu, \iota, \varphi_c, t_c) = \frac{G\mathcal{M}}{c^2 r} \left(\frac{t_c - t}{5G\mathcal{M}/c^3} \right)^{-1/4} \frac{1 + \cos^2 \iota}{2} \times \cos[\varphi(t; t_c, M, \mu) + \varphi_c] , \quad (5.1)$$

$$h_\times(t; r, M, \mu, \iota, \varphi_c, t_c) = \frac{G\mathcal{M}}{c^2 r} \left(\frac{t_c - t}{5G\mathcal{M}/c^3} \right)^{-1/4} \cos \iota \times \sin[\varphi(t; t_c, M, \mu) + \varphi_c] , \quad (5.2)$$

which depend on M , μ , the luminosity distance to the source r , the inclination angle of the source's orbital-momentum vector to the line of sight ι , the time of coalescence of the signal t_c , and the coalescence phase of the signal φ_c . Above, $\varphi(t; t_c, M, \mu)$ is the orbital phase of the binary [177, 178], $\mathcal{M} = \mu^{3/5} M^{2/5}$ is the chirp mass, G is the gravitational constant and c is the speed of light in vacuum. The GW strain in a detector can then be modeled as,

$$h(t) = F_+ h_+(t) + F_\times h_\times(t) , \quad (5.3)$$

where $F_{+,\times}$ are antenna response functions that quantify the sensitivity of the detector to the sky-position and polarization of the source,

$$\begin{pmatrix} F_+ \\ F_\times \end{pmatrix} = \begin{pmatrix} \cos 2\psi & \sin 2\psi \\ -\sin 2\psi & \cos 2\psi \end{pmatrix} \begin{pmatrix} u \\ v \end{pmatrix} , \quad (5.4)$$

with ψ being the wave-polarization angle and $u(\alpha, \delta)$ and $v(\alpha, \delta)$ being detector-orientation dependent functions of the source sky-position angles (α, δ) : [179, 47]

$$u(\alpha, \delta) \equiv -\frac{1}{2} (1 + \cos^2 \alpha) \cos 2\delta, \quad (5.5)$$

$$v(\alpha, \delta) \equiv -\cos \alpha \sin 2\delta. \quad (5.6)$$

Following Ref. [41], let us map the CBC signal parameters $(r, \psi, \iota, \varphi_c)$, into new parameters, $a^{(k)}$, with $k = 1, \dots, 4$, such that the strain in any given detector has a *linear* dependence on them:

$$h(t) = \sum_{k=1}^4 a^{(k)} h_k(t), \quad (5.7)$$

where the $h_k(t)$'s are completely independent of those four parameters. By comparing the above expression for the GW strain with that defined through Eqs. (5.1), (5.2), and (5.3), we find

$$\begin{aligned} h_1(t) &\propto u(\alpha, \delta) \cos[\varphi(t; M, \mu, \alpha, \delta, t_c)], \\ h_2(t) &\propto v(\alpha, \delta) \cos[\varphi(t; M, \mu, \alpha, \delta, t_c)], \\ h_3(t) &\propto u(\alpha, \delta) \sin[\varphi(t; M, \mu, \alpha, \delta, t_c)], \\ h_4(t) &\propto v(\alpha, \delta) \sin[\varphi(t; M, \mu, \alpha, \delta, t_c)], \end{aligned} \quad (5.8)$$

where the proportionality factor is $[GM/c^2][(t_c - t)/(5GM/c^3)]^{-1/4}$. This method of resolving the GW strain signal in a basis of four time-varying functions was first found in Ref. [56] for pulsar signals.

The new parameters, $a^{(k)}$, with the index k taking four values, are defined in

terms of $(r, \psi, \iota, \varphi_c)$ as,

$$\begin{aligned}
a^{(1)} &= \frac{1}{r} \left(\cos 2\psi \cos \varphi_c \frac{1 + \cos^2 \iota}{2} - \sin 2\psi \sin \varphi_c \cos \iota \right), \\
a^{(2)} &= \frac{1}{r} \left(\sin 2\psi \cos \varphi_c \frac{1 + \cos^2 \iota}{2} + \cos 2\psi \sin \varphi_c \cos \iota \right), \\
a^{(3)} &= -\frac{1}{r} \left(\cos 2\psi \sin \varphi_c \frac{1 + \cos^2 \iota}{2} + \sin 2\psi \cos \varphi_c \cos \iota \right), \\
a^{(4)} &= -\frac{1}{r} \left(\sin 2\psi \sin \varphi_c \frac{1 + \cos^2 \iota}{2} - \cos 2\psi \cos \varphi_c \cos \iota \right). \quad (5.9)
\end{aligned}$$

These constitute an alternative set of parameters that define the likelihood ratio. We used parenthetic indices above to avoid confusing them with numerical exponents.

5.2.2 The network detection statistic

Let the inner-product of two temporal functions $p(t)$ and $q(t)$ be defined as

$$\langle p, q \rangle_{(I)} = 4\Re \int_0^\infty df \frac{\tilde{p}^*(f) \tilde{q}(f)}{\zeta_{(I)}(f)}, \quad (5.10)$$

where $\tilde{p}(f)$ and $\tilde{q}(f)$ are the Fourier transforms of $p(t)$ and $q(t)$, respectively, and $\zeta_{(I)}(f)$ is the one-sided noise PSD of the I th detector [26], with $I = 1, \dots, M$ for a network of M detectors. The angular brackets denoting the inner-product are subscripted with the detector index since that product depends on the noise PSD of the detector. Assuming that detector noise $n^I(t)$ is additive, the strain in a detector in the presence of a CBC signal is

$$x^I(t) = n^I(t) + h^I(t), \quad (5.11)$$

where $h^I(t)$ is given by Eq. (5.3), but now with the antenna response functions superscripted with the detector index. (The polarization components $h_{+, \times}(t)$)

also depend on I through the coalescence time, as explained below.) Moreover, if the noise is zero-mean Gaussian and stationary, the log-likelihood ratio (LLR) is [26]

$$\log \Lambda_I = \langle x^I, h^I \rangle_{(I)} - \frac{1}{2} \langle h^I, h^I \rangle_{(I)}, \quad (5.12)$$

which can serve as a statistic for detecting signals in a single detector.

To explore the properties of the LLR, it will be useful to define the (complex) unit-norm template $S^I(t)$ associated with the circular-polarization component of a GW, namely, $h_+(t) + ih_\times(t)$. It can be shown [47] that

$$S^I(t) = g_{(I)}^{-1} \left[\tau^I (t_c - t) \right]^{-1/4} e^{i\varphi(t)}, \quad (5.13)$$

where $g_{(I)}$ (with units of $\sqrt{\text{Hz}}$) is a normalization factor, such that $\langle S^I, S^I \rangle = 1$, and

$$\tau^I = \frac{5}{256 f_s^I} \left[\frac{G\mathcal{M} f_s^I}{c^3} \right]^{-5/3} \quad (5.14)$$

is the time spent by the signal in the detector band, in the Newtonian approximation. Above, f_s^I is the seismic cut-off frequency of the I th detector below which it has little sensitivity for GW signals. The single detector matched-filter output against $S^I(t)$ can then be defined as

$$C^I = \langle S^I, x^I \rangle \equiv \left(c_+^I + ic_-^I \right) = \rho^I e^{i\phi^I}, \quad (5.15)$$

where c_\pm^I , ρ^I and ϕ^I are all real; $\rho^I = |C^I|$ is often termed as the signal-to-noise ratio (SNR) in the I th detector. Since the detector strain due to a GW signal is expected to be tiny, one has $g_{(I)} \gg 1$. Therefore, for computational efficiency, we define a new factor that is closer to unity,

$$\sigma_{(I)} \equiv \left(\frac{G\mathcal{M}/c^2}{1 \text{ Mpc}} \right) \left(\frac{5G\mathcal{M}\tau}{c^3} \right)^{1/4} g_{(I)}, \quad (5.16)$$

with τ computed for a reference detector selected from one of those in the network. This is convenient since, as explained below, the detection statistics and the parameters $\{\psi, \iota, \varphi_c\}$ are all independent of the above parenthetic scale factors; only the source distance depends on them, and is computed after accounting for them.

Using the strain expression in Eq. (5.7), the LLR for a network of multiple detectors can be recast in terms of $a^{(k)}$, provided one knows how the strain from the same CBC signal varies from one detector to the other. This was explained in Refs. [46, 47]. Here, it suffices to note that this dependence arises owing to: (a) The spatial separation of the detectors, which can cause relative delays in the arrival of the signal. These delays are determined by the source's sky-position and can be accounted for in Eqs. (5.1) and (5.2) by adding those delays to t_c . (b) The different orientations of the detectors, which change u and v . Assuming that the noise in the different detectors are statistically independent, the joint log-likelihood ratio for a network of M detectors is

$$\begin{aligned} \log \left({}^{(M)}\Lambda \right) &= \sum_{I=1}^M \log \Lambda_I \\ &= N_k a^{(k)} - \frac{1}{2} M_{ij} a^{(i)} a^{(j)}, \end{aligned} \quad (5.17)$$

where, in the last expression, the sum over detectors has been absorbed in N_k and M_{ij} , as defined below:

$$\begin{pmatrix} N_1 \\ N_2 \\ N_3 \\ N_4 \end{pmatrix} = \chi \begin{pmatrix} \sum_{I=1}^M \sigma_{(I)} u_I c_+^I \\ \sum_{I=1}^M \sigma_{(I)} v_I c_+^I \\ \sum_{I=1}^M \sigma_{(I)} u_I c_-^I \\ \sum_{I=1}^M \sigma_{(I)} v_I c_-^I \end{pmatrix} = \chi \begin{pmatrix} \mathbf{u}_\sigma \cdot \mathbf{c}_+ \\ \mathbf{v}_\sigma \cdot \mathbf{c}_+ \\ \mathbf{u}_\sigma \cdot \mathbf{c}_- \\ \mathbf{v}_\sigma \cdot \mathbf{c}_- \end{pmatrix}. \quad (5.18)$$

Above, \mathbf{u}_σ and \mathbf{v}_σ are network vectors with components $\sigma_{(I)}u_I$ and $\sigma_{(I)}v_I$, respectively, \mathbf{c}_\pm are network vectors with components c_\pm^I , and

$$\chi \equiv \pi^{2/3} \left[\frac{GM_\odot/c^2}{1\text{Mpc}} \right]^{3/4} \text{Mpc} \quad (5.19)$$

is a normalization factor with dimensions of length. Also,

$$\mathbf{M} = \begin{pmatrix} A & B & 0 & 0 \\ B & C & 0 & 0 \\ 0 & 0 & A & B \\ 0 & 0 & B & C \end{pmatrix} \quad (5.20)$$

with

$$\begin{pmatrix} A \\ B \\ C \end{pmatrix} = \chi^2 \begin{pmatrix} \|\mathbf{u}_\sigma\|^2 \\ \mathbf{u}_\sigma \cdot \mathbf{v}_\sigma \\ \|\mathbf{v}_\sigma\|^2 \end{pmatrix}, \quad (5.21)$$

which define the network template-norm, namely, twice the second term on the right-hand side of Eq. (5.17); the first term there can be interpreted as the matched-filter output of the network data-vector, $\mathbf{x} \equiv \{x^1, x^2, \dots, x^M\}$ [47].

Maximizing $2 \log {}^{(M)}\Lambda$ with respect to $\mathbf{a} = \{a^{(1)}, a^{(2)}, a^{(3)}, a^{(4)}\}$ yields

$$2 \log {}^{(M)}\Lambda \Big|_{\mathbf{a}} = \mathbf{N}^T \cdot \mathbf{M}^{-1} \cdot \mathbf{N}, \quad (5.22)$$

which is still a function of $\{M, \mu, \alpha, \delta, t_c\}$. (Note that the above statistic is independent of χ .) The concomitant maximum likelihood *estimates* (MLEs) of the complementary set of four parameters are denoted with an overline:

$$\bar{\mathbf{a}} = \mathbf{M}^{-1} \cdot \mathbf{N}. \quad (5.23)$$

These estimates are also functions of $\{M, \mu, \alpha, \delta, t_c\}$, and are determined by the data through c_{\pm}^I as follows:

$$\begin{pmatrix} \bar{a}^{(1)} \\ \bar{a}^{(2)} \\ \bar{a}^{(3)} \\ \bar{a}^{(4)} \end{pmatrix} = \frac{\chi}{\Delta} \begin{pmatrix} \|\mathbf{v}_\sigma\|^2 (\mathbf{u}_\sigma \cdot \mathbf{c}_+) - (\mathbf{u}_\sigma \cdot \mathbf{v}_\sigma) (\mathbf{v}_\sigma \cdot \mathbf{c}_+) \\ - (\mathbf{u}_\sigma \cdot \mathbf{v}_\sigma) (\mathbf{u}_\sigma \cdot \mathbf{c}_+) + \|\mathbf{u}_\sigma\|^2 (\mathbf{v}_\sigma \cdot \mathbf{c}_+) \\ \|\mathbf{v}_\sigma\|^2 (\mathbf{u}_\sigma \cdot \mathbf{c}_-) - (\mathbf{u}_\sigma \cdot \mathbf{v}_\sigma) (\mathbf{v}_\sigma \cdot \mathbf{c}_-) \\ - (\mathbf{u}_\sigma \cdot \mathbf{v}_\sigma) (\mathbf{u}_\sigma \cdot \mathbf{c}_-) + \|\mathbf{u}_\sigma\|^2 (\mathbf{v}_\sigma \cdot \mathbf{c}_-) \end{pmatrix}, \quad (5.24)$$

where $\Delta \equiv AC - B^2$. The MLE of a parameter will be denoted by placing an overline on its symbol.

It is important to note that the maximization in Eq. (5.22) assumes that the network matrix \mathbf{M} is invertible. This is not true, in general. Indeed, \mathbf{M} is singular when \mathbf{u}_σ is aligned with \mathbf{v}_σ . These two vectors are determined by how the interferometers in the network are oriented with respect to the wave propagation vector, but are not affected by the polarization angle ψ . In addition to this singularity, \mathbf{M} can be rank deficient, thus, making the problem of inverting it ill-posed [180]. Physically, this implies that the network does not have enough linearly independent basis detectors to be able to resolve the source parameters \mathbf{a} . Note that these maladies of \mathbf{M} are dependent on the sky-position angles. This means that a network that is able to resolve the signal parameters for certain source sky-positions may not be able to do so for others. These problems can be tackled by regularizing \mathbf{M} in a variety of ways that have been explored in the context of searches of transient signals from unmodeled sources, also called ‘‘burst’’ searches [180, 181, 182]. These methods obviate the rank-deficiency problem at the cost of making the search statistic sub-optimal. Thus, any deficiencies arising from potential singularities in \mathbf{M} or its regularization

method adopted by a search pipeline will affect its performance. Since \mathbf{M} is independent of the detector strain data, such effects will arise in searches in simulated Gaussian data sets as well, such as the ones studied here. Since our results below are devoid of these maladies, we are confident that they will not arise in real data searches as well.

The maximum-likelihood estimates for the four physical parameters $(r, \psi, \iota, \varphi_c)$ can now be expressed in terms of the above estimates by inverting Eq. (5.9) and replacing \mathbf{a} with $\bar{\mathbf{a}}$. Specifically, for the luminosity distance we get:

$$\bar{r} = \frac{\sqrt{1 + 6 \cos^2 \bar{\iota} + \cos^4 \bar{\iota}}}{2 \|\bar{\mathbf{a}}\|}, \quad (5.25)$$

where $\|\bar{\mathbf{a}}\| \equiv \sqrt{\sum_{i=1}^4 (\bar{a}^{(i)})^2}$ is the norm of the four-parameter vector MLE, and $\bar{\iota}$ is defined below along with the other MLEs. Since those angular parameter estimates should not depend on an overall scaling of $\bar{\mathbf{a}}$, it helps to define the dimensionless unit-norm components $\hat{a}^{(k)} \equiv \bar{a}^{(k)} / \|\bar{\mathbf{a}}\|$. In terms of the $\hat{a}^{(k)}$, the maximum-likelihood estimates for the three angular parameters are,

$$\begin{aligned} \bar{\psi} &= \frac{1}{4} \sin^{-1} \left(\frac{2 \left(\hat{a}^{(1)} \hat{a}^{(2)} + \hat{a}^{(3)} \hat{a}^{(4)} \right)}{\sqrt{1 - \zeta^2}} \right), \\ \bar{\varphi}_c &= -\frac{1}{2} \sin^{-1} \left(\frac{2 \left(\hat{a}^{(1)} \hat{a}^{(3)} + \hat{a}^{(2)} \hat{a}^{(4)} \right)}{\sqrt{1 - \zeta^2}} \right), \\ \bar{\iota} &= \cos^{-1} \left(\frac{1 - \sqrt{1 - \kappa^2}}{\kappa} \right), \end{aligned} \quad (5.26)$$

where $\zeta \equiv 2 \left(\hat{a}^{(1)} \hat{a}^{(4)} - \hat{a}^{(2)} \hat{a}^{(3)} \right)$ and

$$\kappa = \frac{\zeta}{1 + \sqrt{1 - \zeta^2}}. \quad (5.27)$$

Note that the expression for $\bar{\psi}$ goes over to that of $\bar{\phi}_c$ under the transformation $\bar{\psi} \rightarrow (-\bar{\phi}_c)/2$ and $\hat{a}^{(2)} \leftrightarrow \hat{a}^{(3)}$. This relation arises from a similar symmetry exhibited by the $a^{(k)}$ defined in Eq. (5.9). Expressions for the CBC MLEs and the coherent statistic were first obtained in Refs. [46, 47]. Above, we reexpress them in terms of the four parameters $a^{(k)}$ since the search code in LAL uses them [176].

Substituting for \mathbf{M} and \mathbf{N} , the MLR can be expanded as,

$$2 \log \Lambda \Big|_{\bar{\mathbf{a}}} = (\mathbf{w}_+ \cdot \mathbf{c}_+)^2 + (\mathbf{w}_- \cdot \mathbf{c}_+)^2 + (\mathbf{w}_+ \cdot \mathbf{c}_-)^2 + (\mathbf{w}_- \cdot \mathbf{c}_-)^2, \quad (5.28)$$

where \mathbf{w}_{\pm} are network vectors with components w_{\pm}^I ,

$$\begin{pmatrix} w_{I+} \\ w_{I-} \end{pmatrix} = \begin{pmatrix} O_{11} & O_{12} \\ O_{21} & O_{22} \end{pmatrix} \begin{pmatrix} \sigma_{(I)} u_I \\ \sigma_{(I)} v_I \end{pmatrix}, \quad (5.29)$$

and

$$\begin{pmatrix} O_{11} & O_{12} \\ O_{21} & O_{22} \end{pmatrix} = \frac{1}{\sqrt{2\Delta}} \begin{pmatrix} \sqrt{C+A+D}/G_1 & \sqrt{C+A+D}(C-A-D)/(2BG_1) \\ \sqrt{C+A-D}/G_2 & \sqrt{C+A-D}(C-A+D)/(2BG_2) \end{pmatrix}, \quad (5.30)$$

with $D \equiv \sqrt{(A-C)^2 + 4B^2}$ and $G_{1,2} \equiv \sqrt{(C-A \mp D)^2 + 4B^2} / (2B)$. The above matrix diagonalizes \mathbf{M} and, in so doing, identifies the dominant polarization basis, first identified in [46] and named as such in [181].

The coherent search statistic is just $2 \log \Lambda \Big|_{\bar{\mathbf{a}}}$ maximized over $\{M, \mu, \alpha, \delta, t_c\}$, namely,

$$\rho_{\text{coh}}^2 = 2 \log \Lambda \Big|_{\bar{\boldsymbol{\vartheta}}}, \quad (5.31)$$

where $\boldsymbol{\vartheta} = \{a^{(1)}, a^{(2)}, a^{(3)}, a^{(4)}, M, \mu, \alpha, \delta, t_c\}$ is a set of nine parameters for the non-spinning CBC signal. The last five parameters are searched for numerically, by using a grid for the masses and the sky-position and by using the fast Fourier

transform [183] to search for the coalescence time. $\bar{\vartheta}$ denotes the MLE values of these parameters. Searching over (α, δ) requires the flexibility to delay c_{\pm}^I relative to c_{\pm}^J by an interval that can be anywhere between zero and the light-travel-time between the locations of the I th and J th detectors or the negative of it. This is why we construct small snippets of $C^I(t)$ called *C-data* around the end-time of every trigger that is found to be coincident in multiple detectors in a network. The statistic defined above will be termed as the coherent network SNR and is the detection statistic optimal in stationary, Gaussian noise [47].

On the other hand, the *combined* signal-to-noise ratio, which was used as a detection statistic in the past and is used here in Fig. 5.2 for comparison, is defined as

$$\rho_{\text{comb}}^2 = \sum_{I=1}^M (\rho^I)^2 = \|\boldsymbol{\rho}\|^2, \quad (5.32)$$

which is devoid of two significant pieces of information present in the coherent search statistic in Eq. (5.31). The first piece of information is in the form of the $w_{I\pm}$ factors, which assign more weight to the matched-filter output of the detector that is more sensitive to a given sky-position and has a lower noise PSD (or bigger $\sigma_{(I)}$). The second piece of information is in the form of the cross-detector terms that check for the consistency of the phases ϕ^I with those expected of a real signal.

5.2.3 Alternative statistics

The last several science runs at LIGO, GEO600, TAMA, and VIRGO have shown time and again that real detector data is both non-stationary and non-Gaussian. Consequently, neither the single-detector matched-filter-based SNR nor the co-

herent network SNR are optimal in that data. It is also known that empirically constructed search statistics perform better there. These alternative search statistics are based on signal discriminators such as the chi-square [174] and rho-square tests [184], and their performances are compared against the statistics that are optimal in Gaussian and stationary noise. These performances are evaluated in terms of their receiver-operating characteristics, which in turn are constructed from detection efficiencies of simulated signals injected into network data and from the background rates obtained through multiple time-slide experiments.

The statistic that performs better in single-interferometric detector searches is the matched-filtered output weighted by a function of the χ^2 (or chi-square) statistic [171],

$$\rho_{\text{eff}} \equiv \rho \left[\frac{\chi^2}{(2p_{\chi^2} - 2)} \left(1 + \frac{\rho^2}{\rho_0^2} \right) \right]^{-1/4}, \quad (5.33)$$

where ρ_0 and p_{χ^2} are empirical parameters that are deduced by examining the performance of ρ_{eff} in real data. In the latest *low-mass* LIGO search, with $2M_{\odot} < M < 35M_{\odot}$, they were chosen to be 250 and 16, respectively [173]. For the high-mass ($25M_{\odot} < M < 100M_{\odot}$) search studied below, these choices are 50 and 10, respectively. Here, p_{χ^2} is the number of degrees of freedom of the chi-square statistic, and ρ_0 is chosen so that for small ρ and average chi-square values, $\rho_{\text{eff}} \approx \rho$. A large chi-square value indicates that the disagreement between the PSDs of the search template and the putative signal (or noise artifact) in the data is large, and imparts a greater penalty on ρ_{eff} by reducing its value relative to ρ .

The network equivalent of the effective SNR is

$${}^{(M)}\rho_{\text{eff}} = \sqrt{\sum_{I=1}^M (\rho_{\text{eff}}^I)^2} \quad (5.34)$$

and is defined this way simply because it works in real data in discriminating signal injections from background. A coherent statistic that can perform better in real data than its OGSN kin is constructed straightforwardly by replacing c_{\pm}^I with

$$c_{\pm\text{eff}}^I \equiv c_{\pm}^I \left[\frac{\chi_I^2}{(2p_{\chi_I^2} - 2)} \left(1 + \frac{(\rho^I)^2}{(\rho_o^I)^2} \right) \right]^{-1/4}, \quad (5.35)$$

in Eq. (5.28). Since the ρ^I and χ_I^2 statistics are computed in the CBC search pipeline when the data from the individual detectors are filtered, their values are available to the coherent stage for computing the *chi-square-weighted* coherent statistic defined above at little additional computational cost.

Scrutinizing expression (5.28) of ρ_{coh} , one finds that it can be decomposed into two parts. The first part is

$$\rho_{\text{auto-coh}}^2 = \sum_{I=1}^M (w_{I+}^2 + w_{I-}^2) |C^I|^2 \quad (5.36)$$

and is a sum of auto-correlation terms in each detector. This part of the coherent statistic is less discriminatory between signal and noise triggers. The second part,

$$\rho_{\text{cross-coh}}^2 = \sum_{I=1}^M \sum_{\substack{J=1 \\ (J \neq I)}}^M (w_{I+}w_{J+} + w_{I-}w_{J-}) [c_+^I c_+^J + c_-^I c_-^J], \quad (5.37)$$

by contrast, is a sum of cross-correlation terms across pairs of detectors, or baselines, and is critical in checking for phase consistency among signals appearing in the detectors from a GW source. Once again, both of the above statistics can be made more robust against noise glitches by replacing c_{\pm}^I with $c_{\pm\text{eff}}^I$ to obtain their chi-square-weighted counterparts.

Another statistic that is helpful in discriminating signals from noise glitches

in multi-detector data is the null-stream [51]. If $\tilde{C}^I(f)$ is the Fourier transform of $C^I(t)$, then one can show that for GW signals in the data, the mean of

$$Y \equiv \sum_{I=1}^M K_I \sigma_{\text{inv}}^{(I)} S_{h(I)}(f) \tilde{C}^I(f) \quad (5.38)$$

is zero. Above, $K_I = \epsilon_{IJK} F_+^J F_\times^K$, with ϵ_{IJK} being the Levi-Civita symbol, and $\sigma_{\text{inv}}^{(I)} \equiv (\sigma_{(I)})^{-1}$. For non-stationary artifacts, however, this need not be true, thereby, motivating the following discriminator:

$$\eta = \frac{\langle |Y| \rangle}{\sqrt{\text{Var}(|Y|)}}, \quad (5.39)$$

where $\langle x \rangle$ and $\text{Var}(x)$ denote the statistical average and variance of x , respectively. The above construct is called the null-stream statistic. Just like the coherent SNR, it can be decomposed into two parts as well, comprising auto-correlation and cross-correlation terms, respectively. The former is akin to the incoherent energy defined in Ref. [52] for burst searches and will be denoted as η_{auto} . For GW signals one expects η_{auto} to be large while η itself is small. On the other hand, for noise artifacts, η is expected to be large, on the average, even when η_{auto} itself is not very strong. This analysis argues for a new statistic, namely,

$$R = \eta_{\text{auto}} / \eta, \quad (5.40)$$

which we call the ratio-statistic.

5.3 Coherent hierarchical inspiral analysis pipeline

The coherent hierarchical inspiral analysis (CHIA) pipeline mainly comprises two stages, namely, the coincident and coherent stages, respectively. Both in-

involve multiple steps. The coincident stage has been discussed in the past in Refs. [171, 172] and is described here briefly for completeness. It includes the following steps: (a) Compute noise PSDs and generate template-banks of the two component masses for each detector in the network. The noise PSDs vary from one detector to another, and in time. A template bank is constructed for every 2048s chunk of data from every detector [185]. (b) Use the template bank for each detector to filter the data from that detector and output the parameters of triggers crossing the chosen SNR threshold. For the injection studies, simulated software-injections are added in software to the data in this step, before the data are match-filtered. (c) Parameters of the triggers from the participating detectors are then compared to identify coincidences [186]. Before these coincident triggers are considered as detection candidates, in real data one usually applies data-quality vetoes. For our study in simulated data, we forego this stage of the pipeline and, instead, apply the coherent stage directly to the triple-coincident triggers. For the computation of the coherent and null-stream statistics the C-data time-series, which include both the amplitude and the phase time-series of the matched-filter outputs, are required. These time-series are computed in the coherent stage and not upstream in the pipeline since it is computationally less expensive to identify coincidences and construct the C-data only for them.

The coherent stage in the CBC search pipeline is constituted of 4 steps. In the first step, a “coherent bank” of templates is constructed from the parameters of the coincident triggers. Triggers in different detectors that are coincident and arise from the same GW source can have different mass pairs owing to the possibility that the noise PSDs of the detectors they arise in are somewhat different

and because of the random nature of noise. For every coincident trigger we construct a network template with a single mass-pair, namely, the one corresponding to the loudest SNR among all the detectors, to search coherently around the end-time of that putative signal. This mass-pair will be termed as the *max*-SNR pair and the corresponding detector the *max*-SNR detector. For example, consider a triple-coincident trigger with $\{\rho, m_1/M_\odot, m_2/M_\odot\} = \{10.0, 1.43, 1.39\}$, $\{10.9, 1.40, 1.36\}$, and $\{8.9, 1.51, 1.32\}$ in the first, second, and third interferometric detector (or IFO), respectively. Then the *max*-SNR detector is IFO-2 and the *max*-SNR mass-pair is $\{m_1/M_\odot, m_2/M_\odot\} = \{1.40, 1.36\}$, which is the template included in the coherent bank to represent this coincident trigger in the coherent stage.

While this mass pair will not necessarily give the loudest SNR in the two other detectors, it has been found to yield a better performance for the coherent-statistic and null-stream than when they are computed using the original and, often, non-identical mass pairs in the different detectors. (Note, however, that simulated software injections in real data must be used to determine empirically if the detection efficiency is helped by using the same mass pair across all detectors in any given science run.) Also, since error-covariances are known to exist between the mass parameters and the trigger end-time, we search at and *around* the end-times of the single-detector triggers that constitute a given network trigger.

The second step in the coherent stage is the construction of *trigger-banks*, whereby the coherent-bank template for every coincident trigger is copied as a single-detector template. (See Fig. 5.1.) In the subsequent step, the single-

detector templates are used to filter the data from the individual IFOs. This step outputs the time-series of C-data around the trigger end-times in that detector. Additionally, this step computes the template normalization factor and chi-square for the *max*-SNR mass-pair across all detectors per coincident trigger. Note that the values of these constructs are not available earlier in the pipeline for the triggers in the detectors complementary to the *max*-SNR detector since, in general, the mass-pairs would be somewhat different in the preceding coincident stage of the search pipeline. In summary, this step outputs a C-data time-series and the corresponding signal parameters, such as the template normalization factor, for every trigger listed in the *coherent-bank* output file.

The final step of the coherent stage is the *coherent-statistics* step, which matches the parameters of each triple-coincident trigger to the C-data time-series output by the matched-filtering step and uses them and the corresponding template-norms, chi-square values for the respective detectors to compute a variety of multi-detector statistics, such as the coherent SNR, null-stream, the chi-square-weighted coherent SNR, and other alternative statistics.

5.4 Results

To study the performance gain arising from using the coherent stage, we ran the CBC search pipeline with and without that stage on simulated Gaussian noise, with LIGO-I noise PSD [176] in the 4km LIGO detectors in Hanford (H1), Livingston (L1), and in the VIRGO detector (V1), for the duration of approximately a month. Specifically, this search pipeline was run once with signal in-

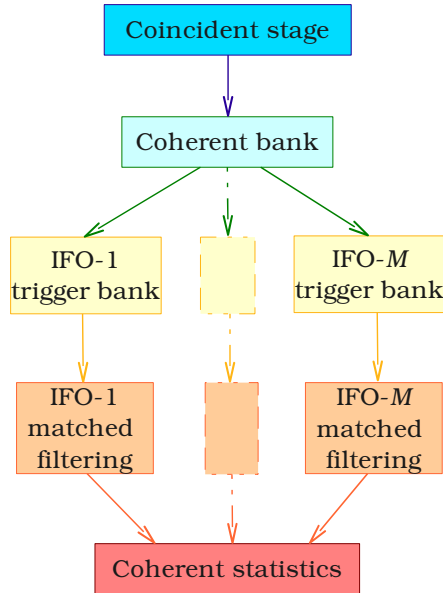


Figure 5.1: A schematic diagram of the coherent stage in the compact binary coalescence search pipeline.

jections and again (parallelly) without injections but with time-slid data so that the background could be estimated. The top plot in Fig. 5.2 compares the performance of the coherent statistics and the combined effective SNR. The bottom plot compares the coherent SNR and null-stream statistics. For these simulations, 1051 signals were injected in software in all three detectors. The source distances of all injections were between 100-500 Mpc. The total masses of these sources were chosen to be in the range 25-100 M_{\odot} , and component masses between 1-99 M_{\odot} . A total of 55 of those injections were found, above the single-

interferometer detection thresholds of 5.0 and coherent SNR threshold of 3.75¹. The latter threshold was intentionally chosen to be lower since we anticipated that some coincident background triggers will have negative cross-terms owing to incoherent phases, thereby, yielding lower coherent SNRs.

All injections recovered by the coincident stage were also found by the coherent stage, and are symbolized by red pluses. The black crosses depict the background triggers that are found by the coincident stage and survive the coherent stage. The blue circles, on the other hand, denote background triggers in the coincident stage that got vetoed by the choice of the threshold on the coherent SNR in the coherent stage. To include them in the top plot, we arbitrarily assign all of them $\rho_{\text{coh}} = 3.0$. Comparing the sets of black crosses and blue circles reveals that the coherent stage not only reduces the number of background triggers but, in this case, also vetoes some of the loudest ones (in combined-effective SNR). Furthermore, whereas all found injections have coherent SNR greater than that of the loudest background trigger, 13 of them have combined-effective-SNR weaker than that of the loudest background trigger (shown in blue circles). When compared to the loudest black cross, that number drops to 7. It drops further when some of the background triggers with the loudest null-stream (as shown in the bottom plot) are vetoed. The resulting performance improvement is depicted in the blue dash-dotted Receiver-Operating-Characteristic (ROC) curve in Fig. 5.3;

¹The detection probabilities are small because, first, all injections made were weak and, second, here we focused only on triggers that are coincident in all three detectors. Owing to sensitivity disparities, it is more likely to find injection trigger coincidences in two of the three detectors. Only weak injections were made since that is where the coherent code can help improve the performance of current searches.

its performance is better than that of the coincident stage (shown in red), without the null-stream vetoes. The former is asymptotic to the ROC curve of the coherent stage (shown in black dashes) for higher false-alarm probabilities.

Finally, Fig. 5.2 reveals the existence of a gap between the loudest background and the weakest injection ρ_{coh} values. One might argue that this is owing to the lack of a sufficient number of weak signal injections made into the data. We have verified that, indeed, one can get some injection triggers to show up in that gap by making multiple weak injections (say, with source distances between 500-750 Mpc) in the data. Those studies also reveal that the detection efficiency in that region is very low (i.e., less than 1 in 250). We believe that this low efficiency is partly caused by the coincident stage, in the way it has been designed and tuned, acting as a bottleneck for the coherent stage.

5.5 Discussion

The main advantage of implementing a blind coherent search in the hierarchical manner explained above is that it has a lower computational cost compared to that of a fully coherent search pipeline. This is primarily because it reduces the number of time-of-arrival values for the coherent code to search for, and because recognizing coincidences is relatively cheaper computationally. There are additional reasons, such the inherent detector-bound nature of data-quality cuts, which are best implemented in the matched-filtering stage. This in turn can reduce an otherwise triple-coincident trigger into a double-coincident one if the third IFO data-points around the concurrent time get vetoed. Since the co-

incident and coherent statistics are the same for two-site CBC searches, it makes sense to not follow them up with the coherent stage.

There are, however, some demerits of searching hierarchically. The first one came to the fore in the results presented above, where the coincident stage is potentially affecting the efficiency of the coherent stage in finding injections. Indeed, it may be possible to improve the injection finding efficiency by reducing the SNR thresholds in the matched-filtering step of the coherent stage. While that may happen, it is also likely that the overall performance of the pipeline will be hurt since it will tend to increase the background rate as well. An alternative solution is to retain the original mass-pairs of the coincident triggers in the coherent stage instead of replacing them with *max*-SNR mass-pairs. This will ensure that injection-finding efficiency of the matched-filtering stage is unaffected, but may hurt the coherence of the triggers and, therefore, ultimately affect the injection finding efficiency of the coherent stage. It may also cause the false-alarm rate to rise, owing to the less stringent requirements on the agreement of the mass-pair values across the network of detectors.

A more optimal solution that addresses the drawbacks of the last two solutions is to assign to every coincident trigger multiple mass-pair templates to search the data with in the coherent stage. This approach makes sense since statistical errors alone are known to cause substantially different mass-templates to be triggered by signals in different detectors arising from the same (injected simulated) source. However, as was shown by the work in Ref. [186] on identifying coincidences, the separation in the mass parameter-space between triggers in two detectors from the same source can be wide enough to allow for

multiple other mass templates to fit in between. Some of these intermediate mass-templates can have a greater chance of not only passing the SNR threshold in individual detectors but also appearing as coherent. The main problem to attack here is to find what the optimal density and size are of these relatively small template banks localized around the coincident mass-pairs. Too small a density or size can hurt signal-finding efficiency and too large a density or size can increase the background rate.

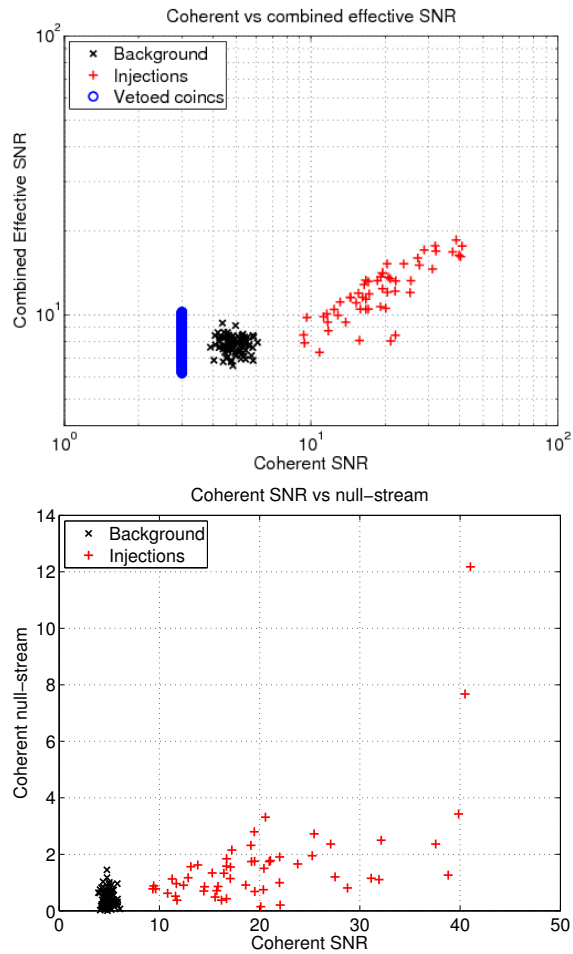


Figure 5.2: These are scatter plots of the combined and coherent SNRs of injection triggers, represented by red plus symbols, and background (or “slide”) triggers, represented by the black crosses. The coherent SNR was used to cluster the triggers, from both injections and slides. The coherent SNR performs noticeably better than the combined effective SNR in discriminating signals from background: In the top plot, at a detection threshold of a little above 6 in the coherent SNR all the injections found in the coincident stage are recovered with a vanishing false-alarm probability. For the same false-alarm probability, the combined effective SNR detects a lesser number of injected signals.

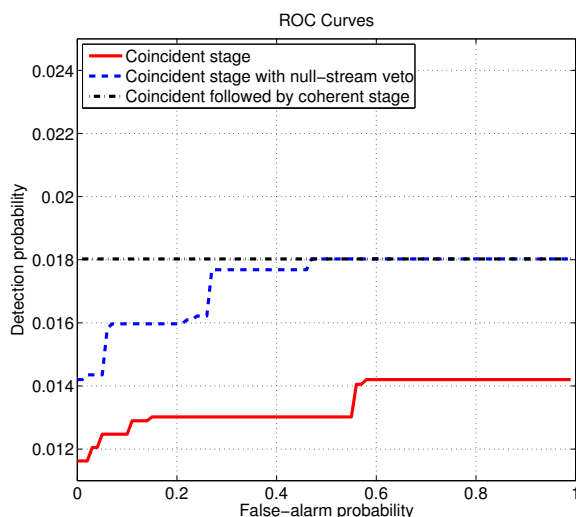


Figure 5.3: The receiver operating characteristic (ROC) curves of three CBC searches are compared above. The ROC of the search with the coincident stage alone is plotted in solid red line, and has the weakest performance owing to the 13 found injections that are weaker than the loudest background trigger in that search. On the other hand, the ROC curve for the hierarchical pipeline, with coherent stage included, is shown in black dash-dotted line and has the best performance. It has a constant detection probability because all found injections are louder than the loudest background trigger for this pipeline. Finally, the third ROC curve, shown as a blue dashed line is the coincident stage, with the null-stream veto applied. This veto improves the performance of the coincident pipeline, so much so that for low detection-thresholds (or high false-alarm probability) its ROC curve rises to match that of the pipeline with the coherent stage. The average error in the detection probabilities plotted here is less than 3×10^{-4} .

Appendix A

Technical details

A.1 Antenna response

The gravitational wave strain is the linear combination of the strains induced by *plus* and *cross* polarizations. The antenna response functions F_+ and F_\times encode the detector responses to the plus and cross polarizations defined in the radiation basis. Their functional forms are given by [187]

$$F_+(\theta, \phi, \psi) = -\frac{1}{2}(1 + \cos^2 \theta) \cos 2\phi \cos 2\psi - \cos \theta \sin 2\phi \sin 2\psi, \quad (\text{A.1})$$

$$F_\times(\theta, \phi, \psi) = \frac{1}{2}(1 + \cos^2 \theta) \cos 2\phi \sin 2\psi - \cos \theta \sin 2\phi \cos 2\psi, \quad (\text{A.2})$$

where θ and ϕ are the spherical polar coordinates of the source in the detector frame, and ψ is the polarization angle defined in Fig. A.1. Since the polarization angle ψ is unknown *a priori*, it is often useful to use the quadrature sum of antenna response functions, also called antenna-pattern:

$$F_{\text{sum}}(\theta, \phi) = \sqrt{F_+^2(\theta, \phi, \psi) + F_\times^2(\theta, \phi, \psi)}, \quad (\text{A.3})$$

which is independent of ψ . The antenna response functions and the antenna-pattern are shown in Fig. A.2.

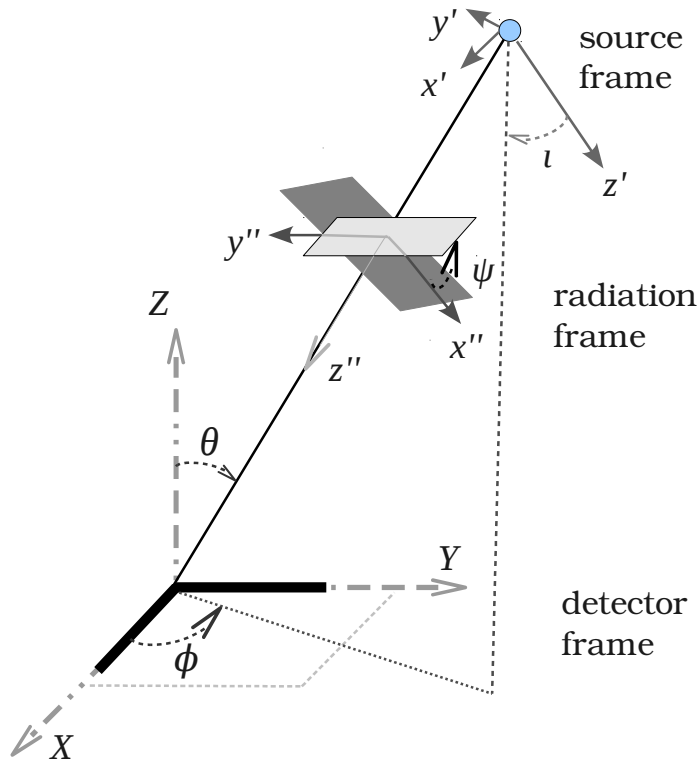


Figure A.1: Definition of source location and orientation angles relative to the inertial frame of a GW detector with arms along X and Y axes. Wave propagates along z'' -axis from a source at an arbitrary sky position defined by (θ, ϕ) and subtending an inclination angle l . The polarization angle ψ , subtended by the wave, is also shown here.

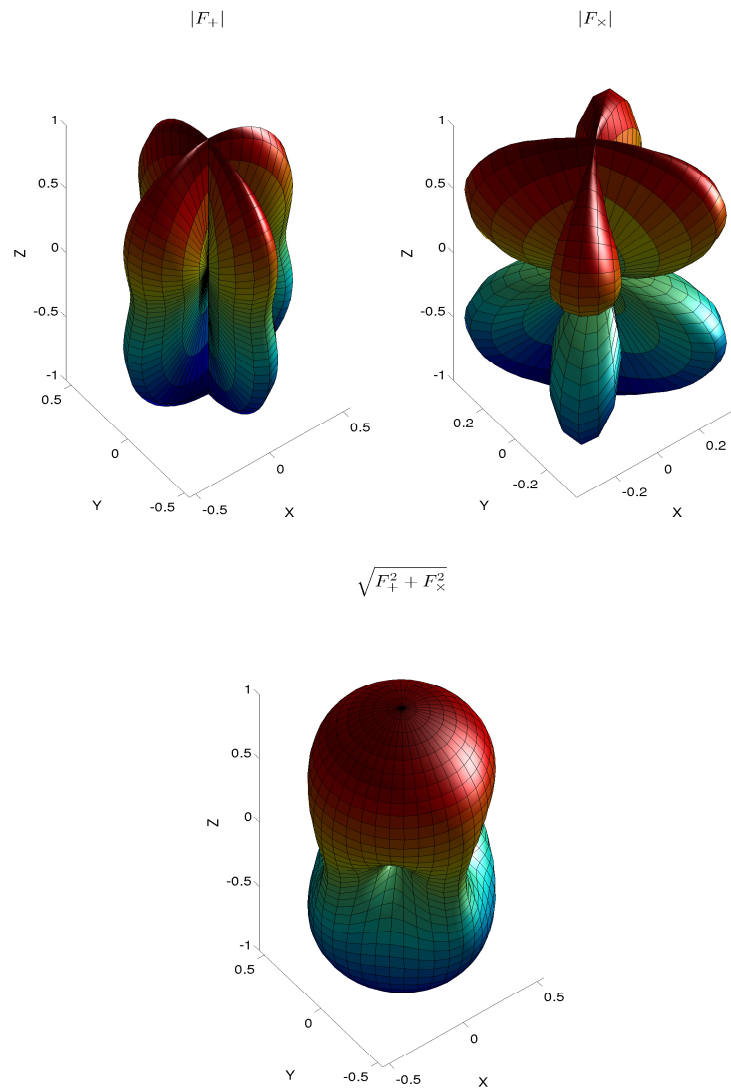


Figure A.2: The antenna response of interferometric gravitational wave detectors to gravitational waves with plus (top left), and cross (top right) polarizations. For making these plots, we have chosen $\psi = 0$. The bottom plot depicts the antenna-pattern (for an unpolarized wave.)

A.2 Parameter accuracy

The *match* can be rewritten as

$$M = 1 - g_{\alpha\beta} \Delta\Theta_{(k)}^\alpha \Delta\Theta_{(k)}^\beta, \quad (\text{A.4})$$

where

$$\Gamma_{(k)\alpha\beta} = (\text{SNR}_{(k)})^2 g_{\alpha\beta}(\Theta_{(k)}), \quad (\text{A.5})$$

$$\begin{aligned} g_{\alpha\beta} &= -\frac{1}{2} \left(\frac{\partial^2 M}{\partial\Theta_{(k')}^\alpha \partial\Theta_{(k')}^\beta} \right) \Big|_{\Theta_{(k')} = \Theta_{(k)}} = g_{\alpha\beta}(\Theta_{(k)}), \\ &:= \begin{pmatrix} \mathcal{G}^{\mu(k)\mu(k)} & \mathcal{G}^{\mu(k)\phi(k)} \\ \mathcal{G}^{\phi(k)\mu(k)} & \mathcal{G}^{\phi(k)\phi(k)} \end{pmatrix}. \end{aligned} \quad (\text{A.6})$$

The components of the above $g_{\alpha\beta}$ matrix are obtained from the derivatives of the beam matrix:

$$\begin{aligned} \mathcal{G}^{\mu(k)\mu(k)} &= \\ &= \frac{1}{2(\mathcal{B}_{(k)(k)})^2} \left[(\mathcal{B}_{(k)(k)}) \left(\frac{\partial^2}{\partial\mu_{k'} \partial\mu_k} \mathcal{B}_{k'k} \Big|_{k'=k} \right) \right. \\ &\quad \left. - \left(\frac{\partial}{\partial\mu_{k'}} \mathcal{B}_{k'k} \Big|_{k'=k} \right)^2 \right], \end{aligned} \quad (\text{A.7})$$

$$\begin{aligned} \mathcal{G}^{\mu(k)\phi(k)} &= \mathcal{G}^{\phi(k)\mu(k)} = \\ &= \frac{1}{2(\mathcal{B}_{(k)(k)})^2} \left[(\mathcal{B}_{(k)(k)}) \left(\frac{\partial^2}{\partial\mu_{k'} \partial\phi_k} \mathcal{B}_{k'k} \Big|_{k'=k} \right) \right. \\ &\quad \left. - \left(\frac{\partial}{\partial\mu_{k'}} \mathcal{B}_{k'k} \Big|_{k'=k} \right) \left(\frac{\partial}{\partial\phi_{k'}} \mathcal{B}_{k'k} \Big|_{k'=k} \right) \right], \end{aligned} \quad (\text{A.8})$$

$$\begin{aligned}
\mathcal{G}_{\phi_{(k)}\phi_{(k)}} = & \\
& \frac{1}{2(\mathcal{B}_{(k)(k)})^2} \left[(\mathcal{B}_{(k)(k)}) \left(\frac{\partial^2}{\partial\phi_{k'}\partial\phi_k} \mathcal{B}_{k'k} \Big|_{k'=k} \right) \right. \\
& \left. - \left(\frac{\partial}{\partial\phi_{k'}} \mathcal{B}_{k'k} \Big|_{k'=k} \right)^2 \right]. \tag{A.9}
\end{aligned}$$

The estimation error (2.42) is obtained from Eqs. (A.5) and (2.41) by utilizing the fact that the inverse of the determinant of a matrix is the same as the determinant of the inverse of that matrix. Above, we assumed that \mathcal{B} is nonsingular.

Appendix B

Advanced detectors studies

B.1 Performance of multi-baseline radiometers

We assess the improvement in performance of a LIGO-VIRGO network gained by adding detectors in Japan and India, namely, KAGRA and INDIGO, respectively. The source PSD is taken to be a constant, $H(f) = 1.516 \times 10^{-48}/\text{Hz}$. The signal band considered here is 40-1024 Hz. For the second-generation configuration, the noise PSDs of LIGO, INDIGO, and KAGRA are taken to be the aLIGO noise PSD. The noise PSD of VIRGO is chosen to be the aVIRGO one. And for the third-generation configuration, the noise PSDs of all detectors are taken to be that of ET, as shown in Figure 2.6.

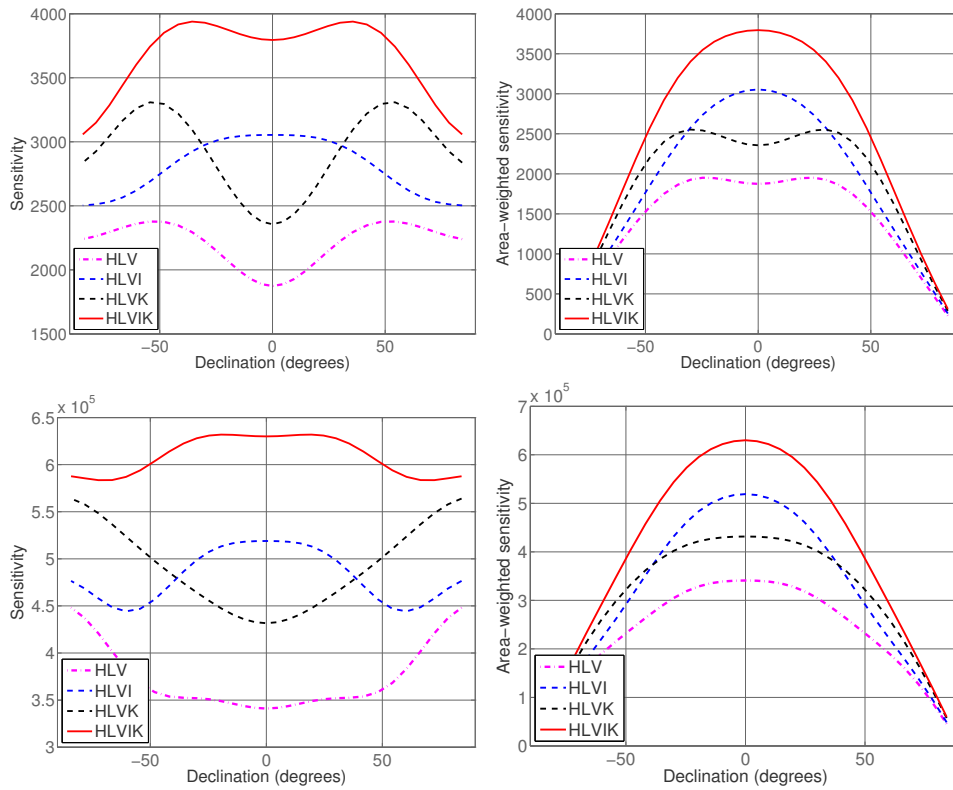


Figure B.1: The sensitivities (left) and their area-weighted counterparts (right) of different LIGO-VIRGO-INDIGO-KAGRA networks in their second (top) and third (bottom) generation configurations are plotted as functions of the declination of a single-pixel SGWB source.

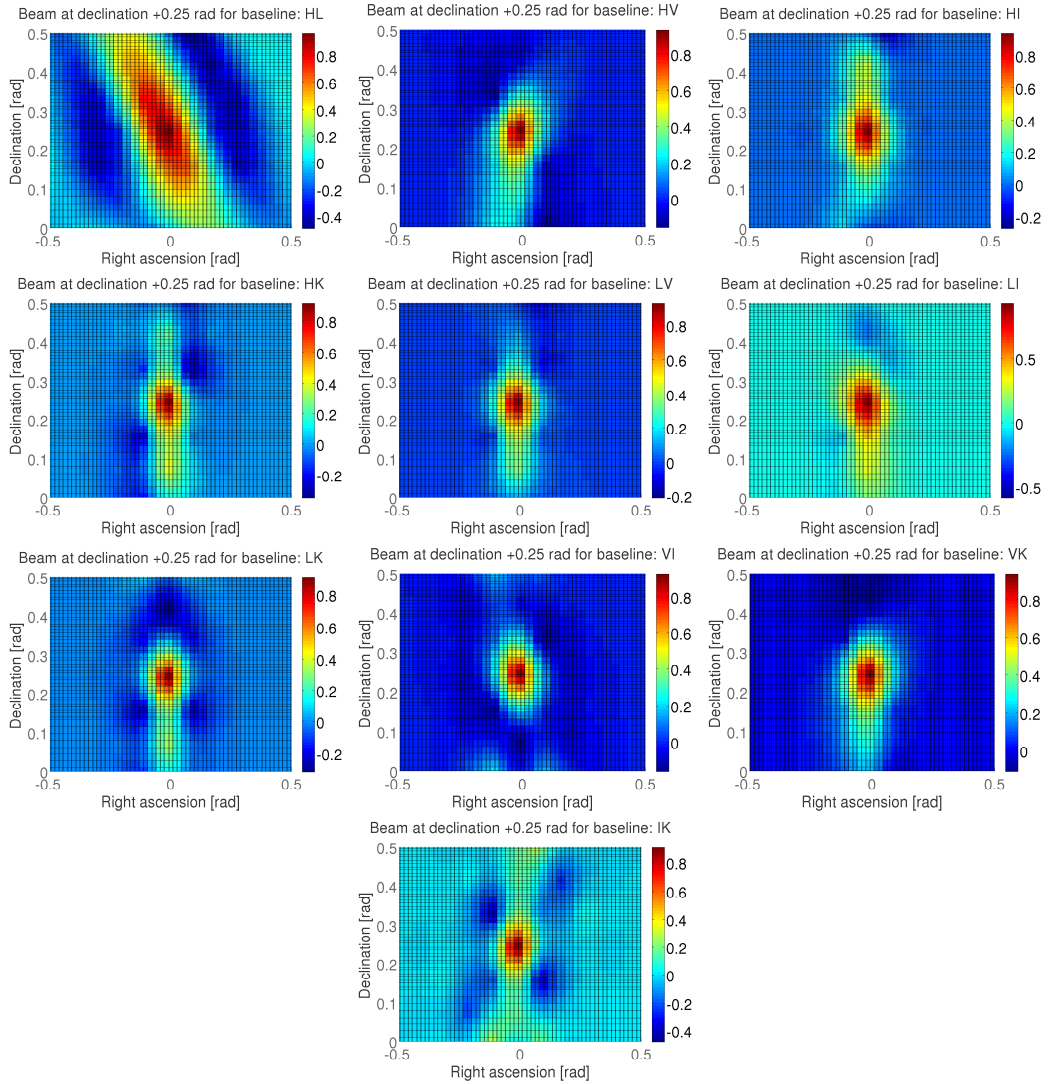


Figure B.2: The beam functions of different second-generation LIGO-VIRGO-INDIGO-KAGRA baselines for a source at declination $+0.25$ radian and with a constant PSD are shown here.

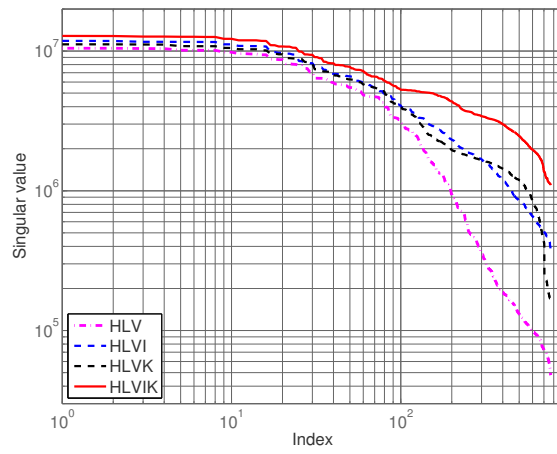


Figure B.3: Singular values of the Fisher matrices for different second-generation LIGO-VIRGO-INDIGO-KAGRA networks are plotted in this figure.

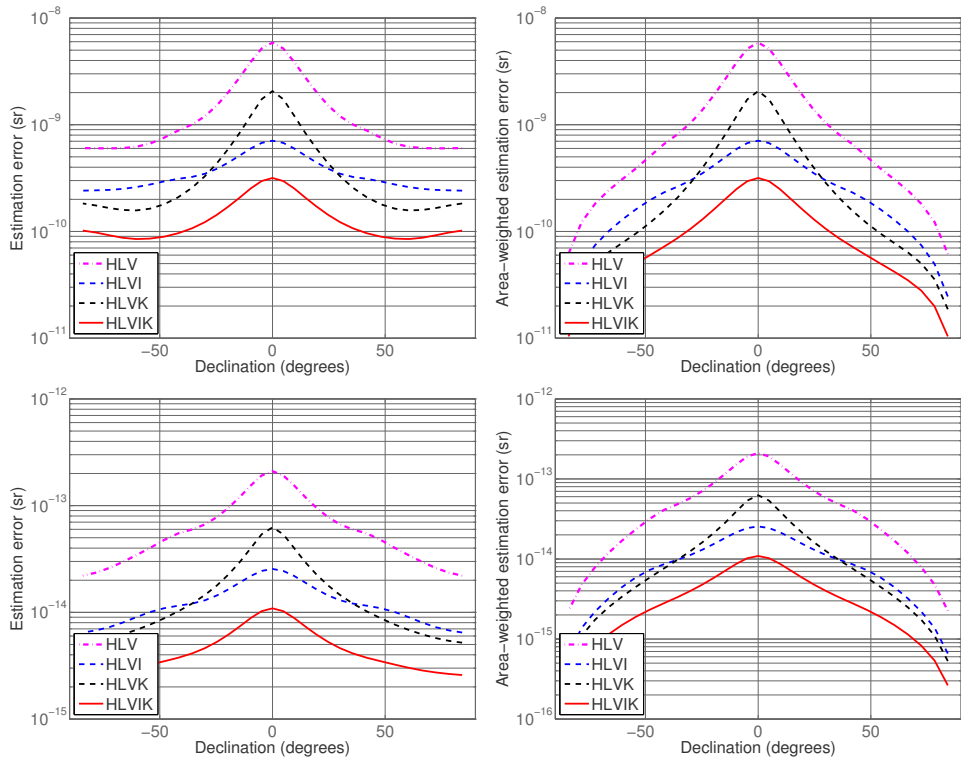


Figure B.4: The 1σ error (left) and area-weighted 1σ error (right) in the solid angle of locating a source in the sky with different LIGO-VIRGO-INDIGO-KAGRA networks in their second (top) and third (bottom) generation configurations.

Appendix C

A directed SGWB search and Olbers' paradox

C.1 Virgo cluster versus the isotropic background

We explicitly compute the ratio between the effective number of sources in the nearby Virgo cluster to that in the distant universe in the same solid angle subtended by the Virgo cluster. This is taken from the Ref. [75].

Consider the flat ($k = 0$) model of the universe which is currently dust dominated. Then the scale factor is given by

$$a(t) = \alpha t^{2/3}. \quad (\text{C.1})$$

The Hubble parameter $H := \dot{a}(t)/a(t)$ at the current epoch $t = t_0$ from Eq. (C.1) becomes

$$H_0 := H(t_0) = \frac{\dot{a}(t_0)}{a(t_0)} = \frac{2}{3t_0}, \quad (\text{C.2})$$

which gives $t_0 = (2/3)H_0^{-1}$. Setting the present scale factor to 1, i.e., $a(t_0) = 1$, one gets

$$a(t) = \alpha t^{2/3} = a(t_0) \left(\frac{t}{t_0} \right)^{2/3} = \left(\frac{3H_0 t}{2} \right)^{2/3}. \quad (\text{C.3})$$

The cosmological redshift z , defined as $1 + z := a(t_0)/a(t) = 1/a(t)$, is a very useful measure of distance. From the Friedmann-Robertson-Walker metric for flat space-time, the proper radius r , from which light emitted at the epoch t reaches us at the epoch t_0 , can be written as

$$r = \int_t^{t_0} \frac{cdt}{a(t)} = \int_t^{t_0} \frac{dt}{(t/t_0)^{2/3}}, \quad (\text{C.4})$$

$$= 3c t_0 \left[1 - \left(\frac{t}{t_0} \right)^{1/3} \right] = \frac{2c}{H_0} \left[1 - \sqrt{a(t)} \right]. \quad (\text{C.5})$$

Then, introducing the definition of redshift, one can write,

$$r = \frac{2c}{H_0} \left[1 - \frac{1}{\sqrt{1+z}} \right]. \quad (\text{C.6})$$

Therefore,

$$dr = \frac{c}{H_0} (1+z)^{-3/2} dz. \quad (\text{C.7})$$

Since there are $n(1+z)^3$ galaxies per unit volume at a redshift z , the effective number of sources in a solid angle $\Delta\Omega$ can be expressed as

$$\Delta n_{\text{eff}} = \int_0^\infty \frac{n(1+z)^3 r^2 \Delta\Omega dr}{r^2 (1+z)^5}, \quad (\text{C.8})$$

$$= n\Delta\Omega \frac{c}{H_0} \int_0^\infty \frac{dz}{(1+z)^{7/2}} = n\Delta\Omega \frac{2c}{5H_0}, \quad (\text{C.9})$$

where n is the average number density of sources in a homogeneous universe, the $(1+z)^5$ factor signifies the decrease in radiation energy density by a factor of $(1+z)^4$ and increase in time interval by a factor of $1+z$ (which reduces the

effective luminosity of the source). Assuming $cH_0^{-1} = 3 \times 10^3 h^{-1}$ Mpc, where $h \sim 0.72$, and $n \sim 0.004 \text{ Mpc}^{-3}$, the effective number of galaxies at 1 Mpc distance per unit solid angle becomes ~ 7 .

The number of sources (galaxies) at the Virgo cluster is $n_{\text{Virgo}} \sim 1500$, spread over a solid angle of $\Delta\Omega_{\text{Virgo}} \approx 0.015$ (that is 50 square degrees). The Virgo cluster is $r_{\text{Virgo}} \sim 16.5$ Mpc away. The redshift to the Virgo cluster is negligible. Thus, for the Virgo cluster the effective number of sources at 1 Mpc distance per unit solid angle is

$$\Delta n_{\text{eff}}^{\text{Virgo}} = \frac{n_{\text{Virgo}}}{\Delta\Omega_{\text{Virgo}} r_{\text{Virgo}}^2} \sim 360. \quad (\text{C.10})$$

This is of course a very rough estimate. However, the Virgo cluster is about 50 times brighter than the background created by the distant sources.

Appendix D

Notes on SNR threshold

D.1 SNR thresholds for the S4 ringdown search

In the low-mass CBC search, the two orthogonal phases of the binary inspiral waveform are expressed as [185]

$$h_c(t) = \frac{2}{c^2} \left(\frac{\mu}{M_\odot} \right) [\pi G M f(t)]^{2/3} \cos[2\phi(t) - 2\phi_0], \quad (\text{D.1})$$

$$h_s(t) = \frac{2}{c^2} \left(\frac{\mu}{M_\odot} \right) [\pi G M f(t)]^{2/3} \sin[2\phi(t) - 2\phi_0]. \quad (\text{D.2})$$

The normalized filter-output is found by filtering the data $x(t)$ against the elliptically-polarized template $h_{\text{ep}}(t) = h_c(t) - ih_s(t)$ and is expressed as

$$\rho_{\text{ep}}(h_{\text{ep}}) \equiv \frac{|\langle x, h_{\text{ep}} \rangle|}{\sqrt{\langle h_{\text{ep}}, h_{\text{ep}} \rangle}} = \frac{|\langle x, h_c \rangle + i\langle x, h_s \rangle|}{\sqrt{\langle h_c - ih_s, h_c - ih_s \rangle}}, \quad (\text{D.3})$$

$$= \frac{\sqrt{\langle x, h_c \rangle^2 + \langle x, h_s \rangle^2}}{\sqrt{\langle h_c, h_c \rangle + \langle h_s, h_s \rangle}}, \quad (\text{D.4})$$

$$= \frac{1}{\sqrt{2}} \frac{\sqrt{\langle x, h_c \rangle^2 + \langle x, h_s \rangle^2}}{\sqrt{\langle h_c, h_c \rangle}}, \quad (\text{D.5})$$

$$\equiv \frac{1}{\sqrt{2}} \rho_{\text{D}}(h_{\text{ep}}). \quad (\text{D.6})$$

The quantity ρ_D defined above is termed as SNR in the low-mass CBC search. Any triggers having $\rho_D \geq 5.5$ are kept, which is equivalent to having $\rho_{\text{ep}} \geq 3.9$.

Contrastingly, for the ringdown search the normalized filter-output is given by Eq. (4.27) as

$$\rho_c(h_c) = \frac{|\langle x, h_c \rangle|}{\sqrt{\langle h_c, h_c \rangle}}. \quad (\text{D.7})$$

The quantity ρ_c is termed as SNR in the ringdown search. That means the quantity ρ_c in the ringdown search is equivalent to the quantity ρ_{ep} in the low-mass CBC search.

Appendix E

List of abbreviations

AGWB: Astrophysical Gravitational-Wave Background

aLIGO: Advanced Laser Interferometer Gravitational-Wave Observatory, the second generation LIGO detectors

ASD: Amplitude Spectral Density

aVIRGO: Advanced VIRGO, a second generation European GW observatory

BH: Black Hole

CBC: Compact Binary Coalescence

CG: Conjugate Gradient

CHIA: Coherent Hierarchical Inspiral Analysis

CMB: Cosmic Microwave Background

cWB: Coherent WaveBurst

Dec: Declination

EFE: Einstein Field Equations

EOB: Effective-One-Body

EP: Equatorial Plane

ET: Einstein Telescope, a third generation gravitational-wave observatory

FAR: False Alarm Rate

GEO: British-German 600 m long gravitational-wave observatory

GR: General Relativity

GRB: Gamma-Ray Burst

GW: Gravitational Wave

HEALPix: Hierarchical Equal Area iso-Latitude Pixelization

H1: The LIGO detector with 4 km arm-length at Hanford

H1L1: The baseline constructed from H1 and L1

H1L1V1: The triple-baseline network constructed from H1, L1 and V1

H1V1: The baseline constructed from H1 and V1

IFO: Interferometric detector

IMBH: Intermediate-Mass Black Hole

IMR: Inspiral-Merger-Ringdown

INDIGO: Proposed Indian Gravitational-Wave Observatory

KAGRA: Japanese second generation 3 km long cryogenic gravitational-wave detector (previously known as LCGT for Large-scale Cryogenic Gravitational-wave Telescope)

LIGO: Laser Interferometer Gravitational-wave Observatory

LLR: Log-Likelihood Ratio

LMXB: Low-Mass X-ray Binary

L1: The LIGO detector with 4 km arm-length at Livingston

LSC: LIGO Scientific Collaboration

ML: Maximum Likelihood

MLE: Maximum Likelihood Estimate

MLR: Maximized-Likelihood Ratio

MSP: Millisecond Pulsar

NMSE: Normalized Mean Square Error

NS: Neutron Star

OGSN: Optimal in Gaussian and Stationary Noise

PSD: Power Spectral Density

PSR: Pulsar

RA: Right Ascension

ROC: Receiver Operating Characteristic

S5: The fifth LIGO science run

S4: The fourth LIGO science run

SGWB: Stochastic Gravitational-Wave Background

SNR: Signal-to-Noise Ratio

S6: The sixth LIGO science run

TT: Transverse-Traceless

VIRGO: European gravitational-wave observatory located at Cascina, Italy

V1: The "European gravitational-wave observatory" with 3 km arm-length at Cascina

VSR: VIRGO Science Run

Bibliography

- [1] A. Einstein, *Annalen der Physik*, **354**, 769 (1996).
- [2] R. A. Hulse, and J. H. Taylor, *Astrophys. J.* **195**, L51 (1975).
- [3] B. F. Schutz, *A first course in general relativity* (Cambridge University Press, 1985).
- [4] P. R. Saulson, *Fundamentals of Interferometric Gravitational Wave Detectors* (World Scientific, 1994).
- [5] <http://www.ligo.caltech.edu/>.
- [6] <https://wwwcascina.virgo.infn.it/>.
- [7] <http://gwcenter.icrr.u-tokyo.ac.jp/en/>.
- [8] <http://www.geo600.org/>.
- [9] D. Sigg, Internal working note, LIGO-P980007-00-D.
- [10] B. F Schutz, *Class. Quant. Grav.* **28**, 125023 (2011).
- [11] C. Cutler, and K. S. Thorne, *An Overview of Gravitational-Wave Sources* [arXiv:gr-qc/0204090].

- [12] S. Bose, T. Dayanga, S. Ghosh, and D. Talukder, *Class. Quant. Grav.* **28**, 134009 (2011).
- [13] D. Talukder, S. Mitra, and S. Bose, *Phys. Rev. D* **83**, 063002 (2011).
- [14] E. Thrane, S. Ballmer, J. Romano, S. Mitra, D. Talukder, S. Bose, and V. Mandic, *Phys. Rev. D* **80**, 122002 (2009).
- [15] A. A. Penzias, and R. W. Wilson, *Astrophys. J.* **142**, 419 (1965).
- [16] R. H. Dicke, P. J. E. Peebles, P. G. Roll, and D. T. Wilkinson, *Astrophys. J.* **142**, 414 (1965).
- [17] B. Allen, *The stochastic gravity-wave background: sources and detection* [arXiv:gr-qc/9604033].
- [18] B. P. Abbott *et al.* (LIGO Scientific), *Nature* **460**, 990 (2009), 0910.5772.
- [19] A. A. Starobinsky, *JETP Lett.* **30**, 682 (1979).
- [20] T. Kahniashvili, A. Kosowsky, G. Gogoberidze, and Y. Maravin, *Detectability of Gravitational Waves from Phase Transitions* [arXiv:astro-ph/0806.0293].
- [21] D. Coward, and T. Regimbau, *New Astron. Rev.* **50**, 461 (2006).
- [22] B. F. Burke, and F. Graham-Smith, *An Introduction to Radio Astronomy* (Cambridge University Press, 1997).
- [23] R. B. Partridge, *3K: The Cosmic Microwave Background Radiation* (Cambridge University Press, 1995).

- [24] S. Mitra, S. Dhurandhar, T. Souradeep, A. Lazzarini, V. Mandic, S. Bose, and S. Ballmer, *Phys. Rev. D* **77**, 042002 (2008), arXiv:0708.2728.
- [25] S. W. Ballmer, *Class. Quant. Grav.* **23**, S179 (2006), gr-qc/0510096.
- [26] C. W. Helstrom, *Statistical Theory of Signal Detection* (Pergamon Press, London, England, 1968), 2nd ed.
- [27] B. Allen and A. C. Ottewill, *Phys. Rev. D* **56**, 545 (1997).
- [28] N. J. Cornish, *Class. Quant. Grav.* **18**, 4277 (2001).
- [29] H. Kudoh and A. Taruya, *Phys. Rev. D* **71**, 024025 (2005), gr-qc/0411017.
- [30] A. Taruya and H. Kudoh, *Phys. Rev. D* **72**, 104015 (2005), gr-qc/0507114.
- [31] A. Taruya, *Phys. Rev. D* **74**, 104022 (2006), gr-qc/0607080.
- [32] Kipp C. Cannon, *Phys. Rev. D* **75**, 123003 (2007).
- [33] A. Lazzarini and R. Weiss, Internal working note LIGO-T040140-00-Z, Laser Interferometer Gravitational Wave Observatory (LIGO) (2004).
- [34] B. Abbott *et al.*, *Phys. Rev. D* **76**, 082003 (2007), astro-ph/0703234.
- [35] E. Flanagan, *Phys. Rev. D* **48**, 2389 (1993).
- [36] B. Allen, and J. D. Romano, *Phys. Rev. D* **59**, 102001 (1999).
- [37] Hierarchical Equal Area isoLatitude Pixelization (HEALPix), <http://healpix.jpl.nasa.gov/>.
- [38] K. M. Górski *et al.*, *Astrophys. J.* **622**, 759 (2005), astro-ph/0409513.

- [39] B. P. Abbott *et al.* (LIGO Scientific), Rep. Prog. Phys. **72**, 076901 (2009), 0711.3041.
- [40] F. Acernese *et al.*, Optics and Lasers in Engineering **45**, 478 (2007).
- [41] P. Ajith, and S. Bose, Phys. Rev. D **79**, 084032 (2009).
- [42] G. Cella, C. N. Colacino, E. Cuoco, A. Di Virgilio, T. Regimbau, E. L. Robinson, and J. T. Whelan, Class. Quant. Grav. **24**, S639 (2007), 0704.2983.
- [43] B. J. Owen, Phys. Rev. D **53**, 6749 (1996), arXiv:gr-qc/9511032.
- [44] C. Cutler, Phys. Rev. D **57**, 7089 (1998), arXiv:gr-qc/9703068.
- [45] G. Hinshaw, M. R. Nolta, C. L. Bennett, R. Bean, O. Doré, M. R. Greason, M. Halpern, R. S. Hill, N. Jarosik, A. Kogut, *et al.*, Astrophys. J. Suppl **170**, 288 (2007), arXiv:astro-ph/0603451.
- [46] S. Bose, A. Pai, and S. Dhurandhar, International Journal of Modern Physics D **9**, 325 (2000), arXiv:gr-qc/0002010.
- [47] A. Pai, S. Dhurandhar, and S. Bose, Phys. Rev. D **64**, 042004 (2001), arXiv:gr-qc/0009078.
- [48] L. Wen and Y. Chen, Phys. Rev. D **81**, 082001 (2010), 1003.2504.
- [49] K. Hayama, S. D. Mohanty, M. Rakhmanov, and S. Desai, Class. Quant. Grav. **24**, S681 (2007), 0709.0940.
- [50] S. Dhurandhar, B. Krishnan, H. Mukhopadhyay, and J. T. Whelan, Phys. Rev. D **77**, 082001 (2008), 0712.1578.

- [51] Y. Gürsel and M. Tinto, Phys. Rev. D **40**, 3884 (1989).
- [52] S. Chatterji, A. Lazzarini, L. Stein, P. J. Sutton, A. Searle, and M. Tinto, Phys. Rev. D **74**, 082005 (2006), arXiv:gr-qc/0605002.
- [53] S. Bose, Phys. Rev. **D71**, 082001 (2005), astro-ph/0504048.
- [54] S. Bose *et al.*, Class. Quant. Grav. **20**, S677-S687 (2003).
- [55] S. Dhurandhar, H. Tagoshi, Y. Okada, N. Kanda, and H. Takahashi, Phys. Rev. D **84**, 083007 (2011).
- [56] P. Jaranowski, A. Królak, and B. F. Schutz, Phys. Rev. D **58**, 063001 (1998).
- [57] N. Sartore, E. Ripamonti, A. Treves, and R. Turolla, Astron. Astrophys. **510**, A23 (2010).
- [58] D. R. Lorimer *et al.*, Astrophys. J. **439**, 933 (1995).
- [59] <http://www.atnf.csiro.au/people/pulsar/psrcat/>.
- [60] J. Abadie *et al.* (LIGO Scientific), Phys. Rev. Lett. **107**, 271102 (2011).
- [61] D. R. Lorimer *et al.*, Mon. Not. R. Astron. Soc. **372**, 777 (2006).
- [62] D. R. Lorimer, *Binary and Millisecond Pulsars*, Living Rev. Relativity **11**, 8 (2008).
- [63] C. Palomba, Mon. Not. R. Astron. Soc. **359**, 1050 (2005).
- [64] B. Knispel, and B. Allen, Phys. Rev. D **78**, 044031 (2008).

- [65] B. Knispel (2011), Ph.D. Thesis, Albert Einstein Institute, Hannover, <http://edok01.tib.uni-hannover.de/edoks/e01dh11/66410357X.pdf>.
- [66] Z. Arzoumanian, D. F. Chernoff, and J. M. Cordes, *Astrophys. J.* **568**, 289 (2002).
- [67] S. A. Story, P. L. Gonthier, and A. K. Harding, *Astrophys. J.* **671**, 713 (2007).
- [68] P. L. Gonthier, C. Billman, A. K. Harding, I. A. Grenier, and M. Pierbatista, *Population Synthesis of Radio and Gamma-ray Pulsars in the Fermi Era* [arXiv:astro-ph/1103.1856].
- [69] T. Regimbau, and J. A. de Freitas Pacheco, *Astron. Astrophys.* **359**, 242 (2000).
- [70] T. Regimbau, and J. A. de Freitas Pacheco, *Astron. Astrophys.* **374**, 182 (2001).
- [71] J. P. Ostriker, and J. E. Gunn, *Astrophys. J.* **157**, 1395 (1969).
- [72] T. Regimbau (Private communication, 2012).
- [73] T. Regimbau, Internal working note, LIGO-VIRGO Scientific Collaboration (2012).
- [74] S. Ballmer, Internal working note, LIGO Scientific Collaboration (2012).
- [75] N. Mazumder, S. Mitra, and S. Dhurandhar, Internal working note, LIGO Scientific Collaboration (2012).

- [76] R. E. E. Rothschild, E. A. Boldt, S. S. Holt, and P. J. Serlemitsos, *Astrophys. J.* **189**, L13 (1974).
- [77] H. V. D. Bradt, and J. E. McClintock, *Ann. Rev. Astron. Astrophys.* **21**, 13 (1983).
- [78] J. A. Orosz *et al.*, *Nature* **449**, 872 (2007).
- [79] T. Bulik, *Nature* **449**, 799 (2007).
- [80] J. Kormendy, and D. Richstone, *Annu. Rev. Astron. Astrophys.* **33**, 581 (1995).
- [81] R. Schöde *et al.*, *Nature* **419**, 694 (2002).
- [82] J. H. Lacy, C. H. Townes, T. R. Geballe, and D. J. Hollenbach, *Astrophys. J.* **241**, 132 (1980).
- [83] E. Serabyn, and J. H. Lacy, *Astrophys. J.* **293**, 445 (1985).
- [84] R. Genzel, D. M. Watson, M. K. Crawford, and C. H. Townes, *Astrophys. J.* **297**, 766 (1985).
- [85] K. Sellgren, M. T. McGinn, E. E. Becklin, and D. N. B. Hall, *Astrophys. J.* **359**, 112 (1990).
- [86] A. Krabbe *et al.*, *Astrophys. J.* **447**, L95 (1995).
- [87] J. W. Haller *et al.*, *Astrophys. J.* **456**, 194 (1996).
- [88] A. Eckart, and R. Genzel, *Nature* **383**, 415 (1996).

- [89] K. Gebhardt, *Nature* **419**, 675 (2002).
- [90] M. C. Miller, and E. J. M. Colbert, *Int. J. Mod. Phys. D* **13**, 1 (2004).
- [91] G. Fabbiano, *Science* **307**, 533 (2005).
- [92] S. F. P. Zwart, and S. L. W. McMillan, *Astrophys. J.* **576**, 899 (2002).
- [93] D. Vanbeveren, H. Belkus, J. V. Bever, and N. Mennekens, *Astrophys. Space Sci.* **324**, 271 (2009).
- [94] T. Pan, A. Loeb, and D. Kasen, *Mon. Not. R. Astron. Soc.* (2012),
doi:10.1111/j.1365-2966.2012.21030.x .
- [95] M. C. Miller, and D. P. Hamilton, *Mon. Not. R. Astron. Soc.* **330**, 232 (2002).
- [96] S. Goswami, S. Umbreit, M. Bierbaum, and F. A. Rasio, (2011),
[arXiv:1105.5884].
- [97] T. Ohkubo, K. Nomoto, H. Umeda , N. Yoshida, and S. Tsuruta, *Astrophys. J.* **706**, 1184 (2009).
- [98] A. Heger, and S. E. Woosley, *Astrophys. J.* **567**, 532 (2002).
- [99] E. Glebbeek, E. Gaburov, S. E. de Mink, O. R. Pols, and S. F. P. Zwart, *Astron. Astrophys.* **497**, 255 (2009).
- [100] H. Baumgardt, J. Makino, and T. Ebisuzaki, *Astrophys. J.* **613**, 1143 (2004).
- [101] R. M. O’Leary, F. A. Rasio, J. M. Fregeau, N. Ivanova, and R. O’Shaughnessy, *Astrophys. J.* **637**, 937 (2006).

- [102] K. Gebhardt, R. M. Rich, and L. C. Ho, *Astrophys. J.* **578**, L41 (2002).
- [103] J. Gerssen *et al.*, *Astron. J.* **124**, 3270 (2002).
- [104] H. Baumgardt, J. Makino, and P. Hut, *Astrophys. J.* **620**, 238 (2005).
- [105] M. Safonova, and P. Shastri, *Astrophys. Space Sci.* **325**, 47 (2010).
- [106] K. Gültekin, M. C. Miller, and D. P. Hamilton, *Astrophys. J.* **616**, 221 (2004).
- [107] T. Okajima, K. Ebisawa, and T. Kawaguchi, *Astrophys. J.* **652**, L105 (2006).
- [108] P. Casella, G. Ponti, A. Patruno, T. Belloni, G. Miniutti, and L. Zampieri, *Mon. Not. R. Astron. Soc.* **387**, 1707 (2008).
- [109] T. E. Strohmayer, and R. F. Mushotzky, *Astrophys. J.* **703**, 1386 (2009).
- [110] A. Patruno, and L. Zampieri, *Mon. Not. R. Astron. Soc.* **403**, L69 (2010).
- [111] F. R. Ferraro, A. Possenti, E. Sabbi, P. Lagani, R. T. Rood, N. D'Amico, and L. Origlia, *Astrophys. J.* **595**, 179 (2003).
- [112] S. F. P. Zwart, and E. P. J. van den Heuvel, *Nature* **450**, 388 (2007).
- [113] P. Kaaret *et al.*, *Mon. Not. R. Astron. Soc.* **321**, L29 (2001).
- [114] S. A. Farrell, N. A. Webb, D. Barret, O. Godet, and J. M. Rodrigues, *Nature* **460**, 73 (2009).
- [115] E. Vesperini, S. L. W. McMillan, A. D'Ercole, and F. D'Antona, *Astrophys. J.* **713**, L41 (2010).

- [116] S. Umbreit, J. M. Fregeau, S. Chatterjee, and F. A. Rasio, *Astrophys. J.* **750**, 31 (2012).
- [117] E. T. Newman, E. Couch, K. Chinnapared, A. Exton, A. Prakash, and R. Torrence, *J. Math. Phys.* **6**, 918 (1965).
- [118] T. Regge, and J. A. Wheeler, *Phys. Rev.* **108**, 1063 (1957).
- [119] F. J. Zerilli, *Phys. Rev. D* **2**, 2141 (1970).
- [120] S. Chandrasekhar, and S. Detweiler, *Proc. R. Soc. Lond. A* **344**, 441 (1975).
- [121] S. Chandrasekhar, *Proc. R. Soc. Lond. A* **358**, 421 (1978).
- [122] C. V. Vishveshwara, *Nature* **227**, 936 (1970).
- [123] M. Davis, R. Ruffini, W. H. Press, and R. H. Price, *Phys. Rev. Lett.* **27**, 1466 (1971).
- [124] S. L. Detweiler, *Proc. R. Soc. Lond. A* **352**, 381 (1977).
- [125] S. L. Detweiler, and E. Szedenits, *Astrophys. J.* **231**, 211 (1979).
- [126] C. T. Cunningham, R. H. Price, and V. Moncrief, *Astrophys. J.* **224**, 643 (1978).
- [127] C. T. Cunningham, R. H. Price, and V. Moncrief, *Astrophys. J.* **230**, 870 (1979).
- [128] C. T. Cunningham, R. H. Price, and V. Moncrief, *Astrophys. J.* **236**, 674 (1980).

- [129] K. D. Kokkotas, and B. G. Schmidt, *Quasi-Normal Modes of Stars and Black Holes*, Living Rev. Relativity **2**, 2 (1999).
- [130] A. Buonanno, G. B. Cook, and F. Pretorius, Phys. Rev. D **75**, 124018 (2007).
- [131] E. Berti, V. Cardoso, J. A. Gonzalez, U. Sperhake, M. Hannam, S. Husa, and B. Brügmann, Phys. Rev. D **76**, 064034 (2007).
- [132] L. S. Finn, Phys. Rev. D **46**, 12 (1992).
- [133] B. P. Abbott *et al.* (LIGO Scientific), Phys. Rev. D **80**, 062001 (2009).
- [134] L. M. Goggin (2008), Ph.D. Thesis, California Institute of Technology, [arXiv:0908.2085].
- [135] L. M. Goggin, Class. Quant. Grav. **23** S709 (2006).
- [136] J. D. E. Creighton, Phys. Rev. D **60**, 022001 (1999).
- [137] B. Allen, “GRASP users manual”, (1997),
<http://www.lsc-group.phys.uwm.edu>.
- [138] R. Adhikari (2004), Ph.D. Thesis, Massachusetts Institute of Technology,
<http://dspace.mit.edu/bitstream/handle/1721.1/28646/1/58964895.pdf>.
- [139] Y. Tsunesada *et al.* (TAMA Collaboration), Class. Quant. Grav. **21**, S703 (2004).
- [140] J. Abadie *et al.* (LIGO Scientific), (2012), [arXiv:1201.5999].
- [141] E. W. Leaver, Proc. R. Soc. Lond. A **402**, 285 (1985).

- [142] F. Echeverria, Phys. Rev. D **40**, 3194 (1989).
- [143] E. Berti, V. Cardoso, and C. M. Will, Phys. Rev. D **73**, 064030 (2006).
- [144] E. Berti, J. Cardoso, V. Cardoso, and Marco Cavaglià, Phys. Rev. D **76**, 104044 (2007).
- [145] S. Caudill, S. E. Field, C. R. Galley, F. Herrmann, and M. Tiglio, Class. Quantum Grav. **29**, 095016 (2012).
- [146] S. Caudill *et al.*, The Ringdown Search Group Internal Working Note (LIGO) (2012).
- [147] LSC Internal working note LIGO-T1000056-v5, Laser Interferometer Gravitational Wave Observatory (LIGO).
- [148] N. Leroy (for the LIGO Scientific Collaboration and Virgo Collaboration), Class. Quantum Grav. **26**, 204007 (2009).
- [149] J. Aasi *et al.*, (2009), [arXiv:1203.5613].
- [150] B. P. Abbott *et al.*, Phys. Rev. D **79**, 122001 (2009).
- [151] S. Klimenko, I. Yakushin, A. Mercer, and G. Mitselmakher, Class. Quant. Grav. **25**, 114029 (2008).
- [152] P. Ajith *et al.*, Class. Quant. Grav. **24** S689 (2007).
- [153] R. Sturani, S. Fischetti, L. Cadonati, G. M. Guidi, J. Healy, D. Shoemaker, and A. Viceré, JPCS **243**, 012007 (2010).
- [154] P. Ajith *et al.*, Phys. Rev. D **77**, 104017 (2008).

- [155] P. Ajith *et al.*, Phys. Rev. Lett. **106**, 241101 (2011).
- [156] L. Santamaría *et al.*, Phys. Rev. D **82**, 064016 (2010).
- [157] T. Damour, A. Nagar, M. Hannam, S. Husa, and B. Bruggmann, Phys. Rev. D **78**, 044039 (2008).
- [158] Y. Pan, A. Buonanno, M. Boyle, L. T. Buchman, L. E. Kidder, H. P. Pfeiffer, and M. A. Scheel, Phys. Rev. D **84**, 124052 (2011).
- [159] K. Thorne, in *Three Hundred Years of Gravitation*, edited by S. Hawking and W. Israel (Cambridge University Press, Cambridge, U.K.; New York, U.S.A., 1987), pp. 330–458.
- [160] J. Abadie *et al.* (LIGO Scientific), Class. Quant. Grav. **27**, 173001 (2010), 1003.2480.
- [161] D. Sigg, Class. Quant. Grav. **25**, 114041 (2008).
- [162] H. Grote, Class. Quant. Grav. **25**, 114043 (2008).
- [163] F. Acernese *et al.*, Class. Quant. Grav. **25**, 184001 (2008).
- [164] S. Nissanke, D. E. Holz, S. A. Hughes, N. Dalal, and J. L. Sievers, Astrophys. J. **725**, 496 (2010), 0904.1017.
- [165] S. Fairhurst, New J. Phys. **11**, 123006 (2009), 0908.2356.
- [166] I. W. Harry, and S. Fairhurst (2010), LIGO Document No. P1000104-v6.
- [167] D. Eichler, M. Livio, T. Piran, and D. N. Schramm, Nature **340**, 126 (1989).

- [168] B. Paczynski, *Acta Astron.* **41**, 257 (1991).
- [169] B. Abbott *et al.* (LIGO Scientific Collaboration), *Phys. Rev. D* **77**, 062004 (2008), 0709.0766.
- [170] J. Abadie *et al.* (LIGO Scientific Collaboration and Virgo Collaboration), *Astrophys. J.* **715**, 1453 (2010), 1001.0165.
- [171] B. Abbott *et al.* (LIGO Scientific Collaboration), *Phys. Rev. D* **77**, 062002 (2008), 0704.3368.
- [172] B. P. Abbott *et al.* (LIGO Scientific Collaboration), *Phys. Rev. D* **79**, 122001 (2009), 0901.0302.
- [173] B. P. Abbott *et al.* (LIGO Scientific Collaboration), *Phys. Rev. D* **80**, 047101 (2009), 0905.3710.
- [174] B. Allen, *Phys. Rev. D* **71**, 062001 (2005), gr-qc/0405045.
- [175] B. S. Sathyaprakash, and S. V. Dhurandhar, *Phys. Rev. D* **44**, 3819 (1991).
- [176] LSC Algorithms Library,
<https://www.lsc-group.phys.uwm.edu/daswg/projects/lalsuite.ht>.
- [177] L. Blanchet, T. Damour, B. R. Iyer, C. M. Will, and A. G. Wiseman, *Phys. Rev. Lett.* **74**, 3515 (1995), gr-qc/9501027.
- [178] L. Blanchet, B. R. Iyer, C. M. Will, and A. G. Wiseman, *Class. Quant. Grav.* **13**, 575 (1996), gr-qc/9602024.

- [179] P. Jaranowski, A. Krolak, K. D. Kokkotas, and G. Tsegas, *Class. Quant. Grav.* **13**, 1279 (1996).
- [180] M. Rakhmanov, *Class. Quant. Grav.* **23**, S673 (2006), gr-qc/0604005.
- [181] S. Klimentko, S. Mohanty, M. Rakhmanov, and G. Mitselmakher, *Phys. Rev. D* **72**, 122002 (2005), gr-qc/0508068.
- [182] S. D. Mohanty, M. Rakhmanov, S. Klimentko, and G. Mitselmakher, *Class. Quant. Grav.* **23**, 4799 (2006), gr-qc/0601076.
- [183] W. H. Press, S. A. Teukolsky, W. T. Vetterling, and B. P. Flannery, *Numerical Recipes 3rd Edition: The Art of Scientific Computing* (Cambridge University Press, 2007).
- [184] A. Rodríguez (2007), Masters Thesis, Louisiana State University, Baton Rouge.
- [185] D. A. Brown (2004), Ph.D. Thesis, University of Wisconsin, Milwaukee, [arXiv:0705.1514].
- [186] C. A. K. Robinson, B. S. Sathyaprakash, and A. S. Sengupta, *Phys. Rev. D* **78**, 062002 (2008), 0804.4816.
- [187] W. G. Anderson, P. R. Brady, J. D. E. Creighton, and É. É. Flanagan, *Phys. Rev. D* **63**, 042003 (2001).